

Influence of post-processing on Ti6Al4V lattice structures produced by Selective Laser Melting



Rimit Kumar Ashok Kumar Jain

Student Number: 4506774

Faculty of Mechanical, Maritime and Materials Engineering (3ME)

Delft University of Technology

Supervisors:	Dr. V.A. Popovich	TU Delft
	S. M. Ahmadi	TU Delft
Thesis committee:	Prof. Dr. I. M. Richardson	Chair, TU Delft
	Dr. J. Zhou	TU Delft

This thesis is submitted for the degree of *Master of Science in Mechanical Engineering – MEA*.

An electronic version of this thesis is available at <http://repository.tudelft.nl/>.

Delft University of Technology

18 October 2017

Acknowledgements

First and foremost, I would like to thank my supervisors Dr. Vera Popovich and Mohammad Ahmadi. This thesis would not have been possible without their support, motivation and guidance. The long and insightful discussions provided me with a better understanding of the thesis and made the writing possible. The discussions were an immense source of knowledge and provided the background required for the completion of this thesis.

I would like to thank Sander Leeflang from the BME department for printing the samples and helping me with the fatigue tests and providing the machine at short notice. The experiments and results of the thesis would not have been achieved without the help of the people at the MSE department. I would like to extend my gratitude to Ton Riemslog, Sander van Asperen, Ruud Hendrikx, Richard Huizenga and Wouter de Goeij. Their help with the experiments and discussion is what helped achieve the results.

I would also like to extend my gratitude to my colleagues Ashwath, Ankit, Gautam, Milan and Constantinos for their help in the labs and discussions. The discussions and much needed coffee breaks are deeply appreciated.

The master's would not have been possible without the support and presence of my friends and family in Delft and in India. I am especially grateful to Srikar, Shishir and Chinmay for making my stay in Delft feel like home. Further, I am thankful to Joe, Greeshma, Madhav, Vishnu, Elise, Vitesh and others who were always there at times of fun and supported me throughout my stay here.

Words cannot describe how grateful I am to my parents and brother back in India. Their support and unconditional love is what has kept me going. No success is enjoyable without sharing it with them.

Rimit Kumar A Jain

Delft, 18 October 2017

Abstract

Selective laser melting (SLM) is a novel technique being increasingly used for the production of porous structures with a high degree of precision and near net shape. These porous materials are finding their use in the biomedical industry for implants.

In this thesis, the effect of post-processing using hot isostatic pressing (HIP) and surface modification techniques, such as chemical etching and sandblasting on the developed microstructure and mechanical properties is studied.

Cylindrical porous samples with a diamond unit cell were produced by the vector based approach from Ti6Al4V ELI powder using the SLM process. The samples were tested in the as-processed and post-processed condition for compression and fatigue life. A comparison between the as-processed vector approach and Stereo Lithography (STL) approach was also studied and discussed in detail.

The post-processing was found to have a positive influence on the microstructure and mechanical properties of the Ti6Al4V lattice structures. The HIP treatment showed the best post-processing step allowing to relieve residual stress, reduce the process induced porosity and obtain the optimal lamellar ($\alpha+\beta$) microstructure. The HIP post-processing resulted in a significant improvement of the fatigue life of the studied porous structures. HIP followed by surface treatment using sandblasting technique was found to be promising for further fatigue life improvement without any reduction in strength as compared to HIP and as-processed conditions. Chemical etching showed improved fatigue life at lower stress levels but decreased strength due to a reduction in relative density.

Additionally, the comparison between the vector and STL approach confirmed the importance of process parameter optimization required to improve the as-processed properties. In this study a combination of HIP and sandblasting methods allowed to improve fatigue properties of vector based samples, making them superior to STL as-processed condition. Thus, the application of the studied post-processing techniques can be further applied to other porous metallic structures in order to improve their mechanical performance.

Contents

Contents	vii
List of Figures	ix
List of Tables	xi
Nomenclature	xiii
Chapter 1 Introduction	1
Chapter 2 Literature review	3
2.1 Additive Manufacturing	3
2.1.1 Classification of AM Processes	3
2.2 Selective Laser Melting (SLM)	4
2.2.1 SLM Process Parameters	5
2.2.2 Defects	6
2.2.3 Advantages and Disadvantages of SLM	8
2.3 Titanium Alloy – Ti6Al4V	8
2.3.1 Open Cell Porous Titanium Structures (Ti6Al4V)	9
2.3.2 Microstructure	11
2.3.3 Surface modification treatments	14
2.3.4 Mechanical Properties	16
2.4 Conclusion	18
2.5 Research Objective	19
Chapter 3 Experimental Section	21
3.1 Material and Methods	21
3.2 Post-processing	22
3.3 Morphological Characterisation	23
3.4 Microstructural and Hardness Analysis	24
3.5 XRD Analysis	24
3.6 Static Mechanical Testing	25
3.7 Fatigue Testing	25
Chapter 4 Results	27
4.1 Morphological Characterisation	27
4.1.1 Relative Density (ρ_{rel})	27
4.1.2 Process induced internal porosity	28
4.1.3 Effect of chemical etching	29

4.1.4	Effect of sandblasting.....	30
4.2	Microstructure and Hardness.....	32
4.2.1	Microstructure	32
4.2.2	Hardness.....	33
4.3	XRD.....	34
4.4	Static Mechanical Testing	36
4.5	Fatigue	38
4.6	As-processed (Vector vs STL based approach)	40
Chapter 5	Discussion.....	45
5.1	Vector approach based samples.....	45
5.1.1	Morphological characterisation	45
5.1.2	Microstructure and hardness.....	46
5.1.3	Surface modification treatments	46
5.1.4	XRD.....	49
5.1.5	Static mechanical testing	50
5.1.6	Fatigue.....	51
5.2	Comparison of vector and STL based approach	53
Chapter 6	Conclusion and recommendations	57
6.1	Conclusions.....	57
6.2	Recommendation for future work.....	58
References	61
Appendix A	Fatigue data overview.....	A-1
Appendix B	Surface roughness quantification	B-1
B.1	Bead roughness	B-1
B.2	Profile Roughness	B-2
Appendix C	Chemical etching trials.....	C-1

List of Figures

Figure 2.1 Schematic Overview of SLM. Reproduced from A. Sidambe <i>et al.</i> (2014) [6].	4
Figure 2.2 SLM process parameters. Reproduced from L. E. Criales <i>et al.</i> (2016) [7].	5
Figure 2.3 Example of cracking. Reproduced from P.C. Collins <i>et al.</i> (2016) [10].	6
Figure 2.4 Example of (a) Porosity and (b) lack of fusion defects. Reproduced from P.C. Collins <i>et al.</i> (2016) [10].	7
Figure 2.5 The unit cells for (a) α and (b) β phases in titanium. Reproduced from A.A. Antonysamy <i>et al.</i> (2012) [21].	9
Figure 2.6 Unit Cell configuration (above) and sample specimens (below) for (a) Cube (b) Diamond and (c) Truncated Cube. Reproduced from S. Ahmadi <i>et al.</i> (2015) [23].	10
Figure 2.7 Schematic representation of cooling curves in Ti6Al4V alloy. Reproduced from A.A. Antonysamy <i>et al.</i> (2012) [21].	11
Figure 2.8 (a) Wrought globular $\alpha+\beta$ microstructure (b) SLM as-processed α' microstructure images from SEM of etched surfaces. Reproduced from G. Kasperovich <i>et al.</i> (2015) [12].	12
Figure 2.9 Microstructure after sub-transus heat treatment (a) 940 °C for 2 hours followed by furnace cooling [5] and (b) 890 °C for 2 hours followed by furnace cooling [31]. The light regions are α phase and the dark regions are β phase.	13
Figure 2.10 Microstructure of HIP processed samples. Reproduced from (a) R. Wauthle <i>et al.</i> (2015) [15] and (b) B. van Hooreweder <i>et al.</i> (2017) [4].	14
Figure 2.11 SEM images of as-processed (left) and chemically etched (right) samples. Reproduced from B. van Hooreweder <i>et al.</i> (2017) [4].	15
Figure 2.12 Fatigue behaviour (S-N curve) of SLM processed and post-processed Ti6Al4V porous structures. Reproduced from B. van Hooreweder <i>et al.</i> (2017) [4].	18
Figure 3.1 3D representation of the porous test sample and diamond unit cell. Reproduced from R. Wauthle <i>et al.</i> (2015) [15].	21
Figure 3.2 Schematic of the vector based approach for the manufacturing of porous structures using SLM. Reproduced from S.M. Ahmadi <i>et al.</i> (2017) [13].	22
Figure 3.3 Schematic representation of the top, middle and cross section location of the samples.	24
Figure 3.4 Instron Electropuls E10000 used for fatigue testing.	26
Figure 4.1 Porosity measurements for as-processed sample using the Keyence VHX Microscope.	28
Figure 4.2 Effect of chemical etching on HIP Sample (a) Before CE and (b) After CE.	29
Figure 4.3 (a) Shaded area represent the region affected by chemical etching. SEM images from the middle of the sample (b) core and (c) edges of the sample after chemical etching.	30
Figure 4.4 Effect of sandblasting on HIP samples (a) Before SB and (b) After SB.	31

Figure 4.5 (a) Shaded area represents the area affected by sandblasting. SEM images from the middle of the sample (a) core and (b) edges of the sample after sandblasting.	31
Figure 4.6 Optical Microscopy images for (a) as-processed (b) HIP (c) HIP+CE and (d) HIP+SB samples.	33
Figure 4.7 (a) Plot for the average hardness and indent shape and size for (b) As-processed (c) HIP (d) HIP+CE and (e) HIP+SB.	34
Figure 4.8 XRD pattern for the as-processed and HIP samples.	35
Figure 4.9 Compression specimen (a) before testing and after testing for (b) as-processed (b) HIP (c) HIP+CE and (d) HIP+SB sample.	37
Figure 4.10 σ - ϵ plots after compression for (a) as-processed (b) HIP (c) HIP+CE and (d) HIP+SB.	38
Figure 4.11 Typical sample failure after fatigue at (a) one or (b) two planes.	39
Figure 4.12 S-N plot for the as-processed and post-processed conditions after normalisation... ..	39
Figure 4.13 Optical micrographs for (a) Vector based and (b) STL based as-processed samples.	41
Figure 4.14 SEM images for (a) Vector based and (b) STL based sample.	41
Figure 4.15 Mean σ - ϵ plot for vector based and STL based samples.	42
Figure 4.16 S-N plot for the as-processed vector based and STL based samples after stress normalisation.	43
Figure 5.1 (a) Process induced internal defects and porosity and (b) Lack of fusion between beads.	45
Figure 5.2 Schematic of sandblasting using Al_2O_3 abrasives.	47
Figure 5.3 (a) and (b) Aluminium oxide abrasive particles and (c) HIP+SB sample strut surface.. ..	48
Figure 5.4 Mean σ - ϵ plots for the as-processed and post-processed samples.	50
Figure 5.5 S-N curve using maximum applied stress during fatigue for as-processed and post-processed samples.	51
Figure 5.6 Fatigue cracks for (a) as-processed and (b) HIP+SB sample.	52
Figure 5.7 Compression specimens after testing (a) Vector based and (b) STL based.	54
Figure 5.8 Fatigue cracks in (a) Vector based and (b) STL based samples.	54
Figure 5.9 S-N curve comparison of as-processed vector based and STL based with HIP+SB samples.	55

List of Tables

Table 2.1 Compression test results of SLM processed and post processed Ti6Al4V alloy. Reproduced from B. van Hooreweder <i>et al.</i> (2017) [4].	17
Table 3.1 Overview of the samples used for testing in this study.	23
Table 4.1 Relative density and internal porosity of the samples.	27
Table 4.2 Statistical data for internal porosity of the samples.	28
Table 4.3 Influence of chemical etching on the strut thickness.	29
Table 4.4 Influence of sandblasting on the strut thickness.	30
Table 4.5 β phase fraction in weight percent, calculated by optimal method.	32
Table 4.6 Stresses induced after sandblasting on HIP samples based on $\sin^2 \psi$ method.	36
Table 4.7 Compressive mechanical properties for as-processed and post-processed samples.	36
Table 4.8 Power law fit parameters ($y=ax^b$).	39
Table 4.9 Relative density and unit cell size of the samples.	40
Table 4.10 Vickers hardness test results.	41
Table 4.11 Compressive mechanical properties.	42
Table 4.12 Power law fitting parameters ($y=ax^b$).	43

Nomenclature

AM	Additive Manufacturing
SLM	Selective Laser Melting
STL	Stereo lithography
BCC	Body centred cube
HCP	Hexagonal close packed
AB	As-processed
HIP	Hot Isostatic Pressing
CE	Chemical Etching
SB	Sandblasting
SEM	Scanning Electron Microscope
XRD	X-ray Diffraction

Chapter 1 Introduction

Metal alloys find their usage in various industrial applications. Even with the extensive research over the years, the manufacturing of complex shapes and customisation of properties remains a challenge [1]. The solution to these problems has been seen in terms of novel production techniques. One such production technique is Additive Manufacturing (AM), popularly known as 3D printing. AM in its early stages was used as a method for building prototypes. But with the advancements in technology and years of research enabled its application for producing parts for direct commercial usage ranging from orthopaedic implants to aircraft components.

Ti6Al4V alloy finds extensive usage in the biomedical industry due to their good mechanical properties, high strength to weight ratio and biocompatibility. Selective laser melting (SLM) is a powder based AM technique. SLM of Ti6Al4V alloy enables the possibility of manufacturing intricate designs and shape. The ability to manufacture porous structure with lattice unit cells of controlled geometry is advantageous for the biomedical industry. It enables the manufacture of parts with properties matching the bone intended to be replaced, in the process ensuring better integration of the implant. In addition, the SLM process provides the freedom to customise the implant with respect to the patient's requirements with ease. Hence, a lot of research is focussed towards the usage of SLM for Ti6Al4V porous structures.

Despite the years of research, the SLM processing of Ti6Al4V has its drawbacks and a fundamental understanding of the microstructure-properties relationship is still required. The as-processed SLM parts are brittle in nature and require post-processing for utilisation. Furthermore, the processing, if not appropriately optimised, results in a high amount of surface roughness and porosity. These defects can be detrimental to the mechanical performance of the structures making them prone to premature failure. Thus, it is important to post-process the SLM parts with appropriate surface modification and heat treatments in order to obtain an ideal combination of properties for their prolonged service life.

The aim of this research is to develop the most optimal post-processing steps, in particular, hot isostatic pressing (HIP) and surface modification treatments for the diamond unit cell type porous structure. This would enable an understanding of the influence of the post-processing on the microstructure and developed mechanical properties. The mechanical properties in this research are studied in terms of compression and fatigue behaviour. The diamond unit cell is chosen due to its isotropic structure, which ensures uniform properties in all directions with respect to the design and only requires the study of the post-processing on the material properties.

The report is divided into six chapters. The introduction to the thesis and its importance is given in Chapter one, which is followed by a summary of the literature review and research objectives provided in Chapter two. Chapter two gives an overview of the available data and research that

has been carried out on SLM processed Ti6Al4V alloy for both the open cell porous and full density structures. The third chapter describes the material and methods used for testing and the characterisation involved to carry out the thesis. Chapter four consists of the results of the tests and characterisation carried out on the samples followed by a discussion of the results in Chapter five. Based on the results and discussions, the conclusion of the thesis are shown in Chapter six which also includes the recommendation for further research. The appendix consists of all the additional images and data that have not been included in the report but are important for the complete understanding of the thesis.

Chapter 2 Literature review

2.1 Additive Manufacturing

Additive manufacturing can be defined as a technique for processing complex metallic structures by adding material in layers to produce a complete part from 3D model data. AM as opposed to removal of material seen in conventional techniques, facilitates to achieve a near-net shaped part with minimum or no finishing requirements [2].

The development of metal AM as a manufacturing technique started in 1987 with the introduction of the first modern AM machine by 3D Systems. But the historical development of the technique can be dated back to the 1860s which described the practice of layered manufacturing in broader terms. The earliest mention of this technique was in photo sculpture and topography in the late 18th century. Early 19th century, saw the development of creating 3D parts with material deposition using a moving deposition source supplying material at a constant rate [2, 3].

The start of the 20th century saw the development of various AM techniques in use and development for metal AM such as Direct Metal Deposition (DMD) technique. They involve the use of high power lasers to produce full density titanium alloy and steel parts for direct application. Also, the advancements in AM and laser technology led to the use of new power sources resulting in the introduction of Electron Beam Melting (EBM) and Selective Laser Melting (SLM) [2, 3].

This rapid development of the technique over the last three decades with the advances in material sciences, has enabled many industries to realise the potential of the technology in terms of cost reduction and complex design manufacturing capabilities. This has led to an increase in research and development of the technology at a rapid pace in both industries as well as academic research groups [2, 3].

2.1.1 Classification of AM Processes

The ISO/ASTM terminology classifies the AM processes into seven broad categories mentioned below [2].

- Binder Jetting: “an AM process in which a liquid bonding agent is selectively deposited to join powder materials”.
- Directed Energy Deposition: “in which focused thermal energy is used to fuse materials by melting as they are being deposited. Focused thermal energy means that an energy source (e.g., laser, electron beam, or plasma arc) is focused to melt the materials being deposited”.

- Material Extrusion: “is an AM process in which material is selectively dispensed through a nozzle or orifice”.
- Material Jetting: “an AM process in which droplets of build material are selectively deposited. Example materials include photopolymer and wax”.
- Powder Bed Fusion: “an AM process in which thermal energy selectively fuses regions of a powder bed”.
- Sheet Lamination: “an AM process in which sheets of material are bonded to form an object”.
- Vat Polymerization: “an AM process in which liquid photopolymer in a vat is selectively cured by light-activated polymerisation”.

The focus of this research is towards the powder bed fusion technique and in particular selective laser melting of titanium alloys. An overview of the technique with the process parameters and defects involved are explained in the next section.

2.2 Selective Laser Melting (SLM)

SLM is a layer-wise material addition AM technique, in which complex 3D components are built by selectively melting successive layers of metal powder together by the application of a highly focused and computer controlled laser beam [4]. It follows a bottom to top production approach as seen with a majority of AM processes. SLM is generally associated with a short laser-powder interaction time and a highly localised heat input. Thus, resulting in a steep thermal gradient and rapid cooling rates in the built part [5].

Figure 2.1 shows a schematic of the SLM setup used for the production of 3D parts. A layer of metallic powder of a predefined depth or thickness is deposited on the building platform. The thickness of the layer depends on the defined 2D cross-section of the 3D CAD part file fed to the system to produce the component. The laser scans the predefined area and selectively melts the powder to fuse it locally. The building platform is subsequently lowered, the next layer of powder deposited and the process repeated layer by layer to build up the 3D part/component. The entire process is carried out in vacuum or in an inert atmosphere to maintain low air content in the chamber during the component build up to avoid contamination or oxidation.

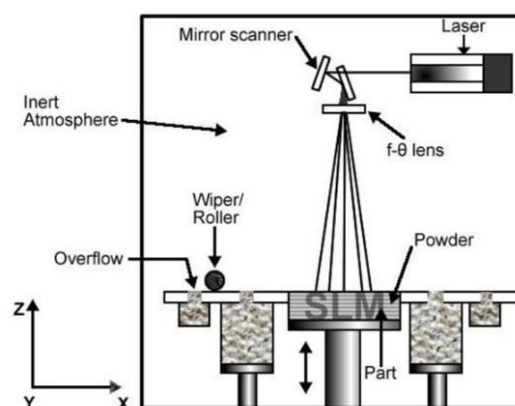


Figure 2.1 Schematic Overview of SLM. Reproduced from A. Sidambe *et al.* (2014) [6].

2.2.1 SLM Process Parameters

In SLM, laser parameters, process parameters and material properties must be studied to have a better understanding of the technique and its utilisation for producing parts. Some of the important process parameters involved in SLM are: laser power (P), laser wavelength (λ), layer thickness (s), hatch distance (h), scanning velocity (v) and scanning strategy as shown in Figure 2.2 [7]. In addition to the mentioned parameters, the base plate temperature, powder size, powder chemistry, build orientation and the inert gas environment available in the equipment play a detrimental role in the properties of the part produced by SLM process.

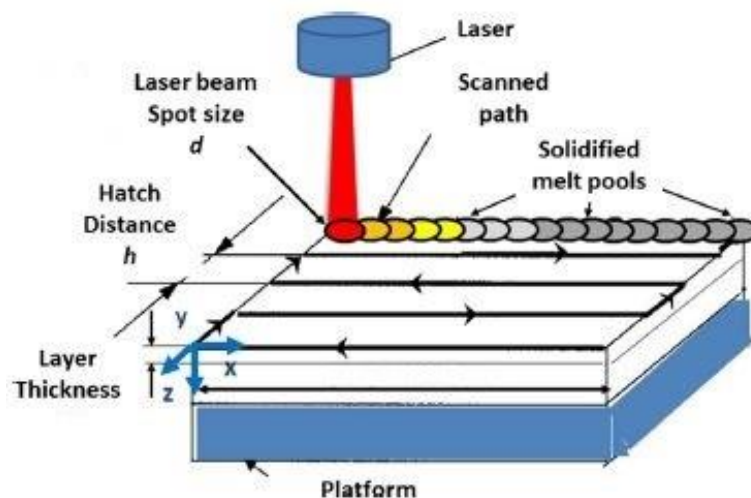


Figure 2.2 SLM process parameters. Reproduced from L. E. Criales *et al.* (2016) [7].

2.2.1.1 Base Plate/Substrate Heating

T. Vilaro *et al.* (2011) mentions the importance of heating the base plate/substrate to temperatures of 500 °C for Ti6Al4V alloy to relieve the thermal stresses in the material. The solidified material due to the high temperature gradient between the build platform and laser melted part is susceptible to high levels of residual stresses similar to that seen in welding [8]. It also helps in removing any moisture that may be present in the powder or on the base plate.

2.2.1.2 Energy Density

The energy density is an important factor in the SLM process that defines the properties and structural integrity of the produced part. Energy density E (Jm^{-3}) is defined as the energy supplied per unit volume and is given by $E = P/v \cdot h \cdot t$, where P is the laser power in Js^{-1} , v is the scanning velocity in ms^{-1} , h is the hatch spacing in m and t is the layer thickness in m [9, 10]. An optimal value of energy density is used by varying the affecting parameters to ensure the complete melting of the powders and minimise the defects associated with the SLM process. The optimal values for the process parameters are determined on a trial and error basis [8, 9, 11-13]. The parameters are specific to a metal powder size, composition and the SLM machine used for the fabrication of the part. Hence, it requires a series of experiments to determine the optimum

parameters with respect to the minimum energy density needed for complete material fusion with the desired material properties in the part.

2.2.2 Defects

Since SLM is a process parameter reliant technique, the use of optimised parameters is of utmost importance. A number of defects can arise due to unsuitable selection of parameter. The most common defects associated with SLM are surface balling, cracking, porosity and surface roughness.

2.2.2.1 Surface Balling

Surface balling refers to the formation of bulges on the surface due to lack of wetting between the molten liquid and the solidified layer or the powder bed. A major reason for this is the contamination due to oxygen, which causes the formation of oxides. This results in a lack of spreading out of the molten material on the oxide surface due to the decrease in surface tension by oxygen contamination at high temperatures in the melt pool. Temperature influences both the surface tension and the rate of oxide formation. Thus, the heat input has a major influence on the surface balling effect [14].

2.2.2.2 Cracking

Cracking is another common defect in SLM that occurs due to the rapid solidification rate observed in the process. It is a result of the contraction of the cooling phases which cause an increase in the internal or residual stresses in the built part. The cracks act as a site for the initiation and propagation during mechanical failure by fatigue. Hence, it is important that appropriate scanning and stress relieving strategies are utilised to minimise the internal stresses. Figure 2.3 shows an example of cracking in SLM processed parts.

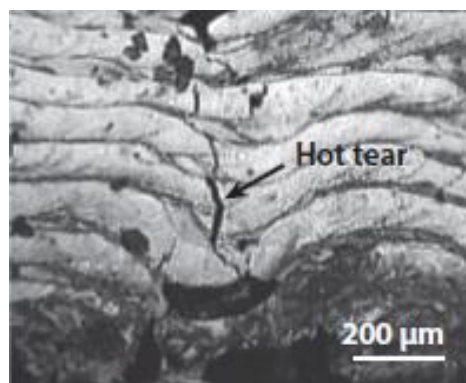


Figure 2.3 Example of cracking. Reproduced from P.C. Collins *et al.* (2016) [10].

2.2.2.3 Porosity

Porosity is the most widely observed defect which cannot be avoided completely but minimised by using appropriate process parameters and shielding environment. The types of porosity that can be observed in SLM manufactured parts include lack of fusion pores and gas entrapped pores

[8, 15, 16]. The gas entrapped spherical pores, seen even in casting are formed due to the gases present between the powder particles which are entrapped in the solidified part due to the rapid cooling rate. An additional possible reason for pore formation is due to the increase in solubility of gases in the melt pool formed at the elevated temperatures seen during the SLM process. These kind of pores can be avoided either by heating the substrate or reducing the volume of the melt pool by decreasing either the laser power or the layer thickness. Another type of porosity observed is the lack of fusion porosity which is generally characterised by larger pore size when compared to gas entrapped pores. These defects are due to the improper fusion of material between consequent layers of powder which are a result of unsuitable process parameters. These defects can be minimised by reducing the thickness of the layer for a given energy density ensuring complete melting and thus fusion of subsequent layers [8]. In addition to this, pores can be formed by the evaporation of low melting point constituents of the alloy powder due to the high temperature melt pool [17]. Process induced porosity in porous structures are also affected by the strut inclination, where horizontal struts have high porosity or are even incomplete because of the lack of support structures during the scanning of loose powder for part fabrication [15]. Figure 2.4 shows examples of porosity defects observed in SLM processed parts.

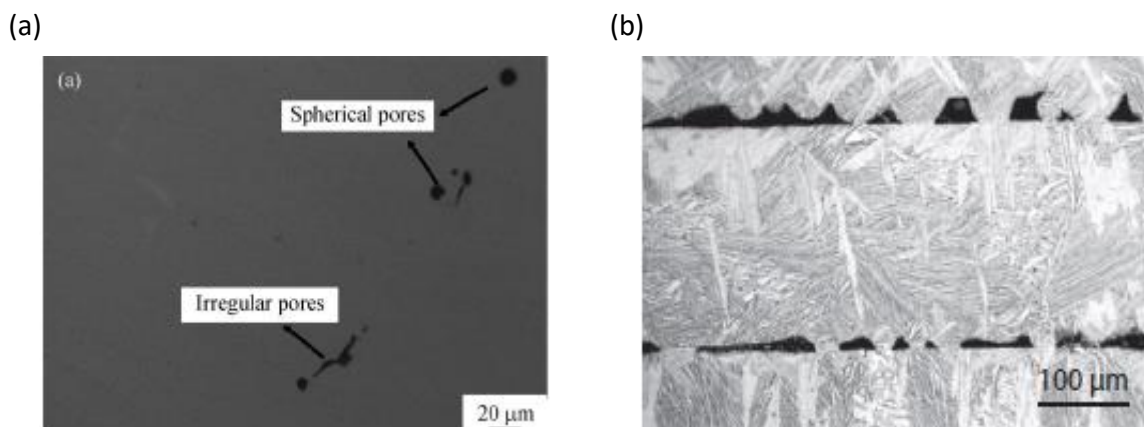


Figure 2.4 Example of (a) Porosity and (b) lack of fusion defects. Reproduced from P.C. Collins *et al.* (2016) [10].

2.2.2.4 Surface Roughness

Surface Roughness is another defect associated with SLM. It influences numerous material properties and hence is an important defect that has to be minimised by the optimisation of process parameters. Surface roughness can be due to the deposition of powder particles on the surface due to lack of melting or sputtering. This results in inhomogeneous deposition of powder on the strut or structure surface [18]. The surface quality in a fully dense sample can be improved significantly by the application of an additional re-melting step or by varying the energy density parameters to optimised values. In the case of porous structures, chemical etching is a process suggested to remove the loose powder grains and thus improving surface quality but has a disadvantage of reduction in the strut size [18, 19].

2.2.3 Advantages and Disadvantages of SLM

The advantages of SLM technique are:

- Well suited technique for manufacturing high quality parts in low to medium quantities.
- Good repeatability and ability to manufacture complex parts. For example, for implant manufacturing SLM provides the ability to produce parts with respect to the patient's specific requirements.
- Low buy to fly ratio which refers to the amount of material bought to manufacture the complex part. In conventional techniques, most of the material is machined away to produce the complex geometry resulting in significant wastage of material which is reduced in all the AM techniques.
- Lower production time and manufacturing cost when complex geometries are produced in low to medium quantities.

Associated disadvantages are:

- Formation of non-equilibrium phases such as martensite in Ti6Al4V alloy due to the rapid solidification and high cooling rates, which affect the mechanical properties of the material.
- High initial cost of investment for machinery.
- Lack of standards for testing, especially for lattice structures.
- High residual stresses and porosity.
- Anisotropic properties due to the microstructure being aligned along the building direction, especially in solid parts.

Based on the associated advantages and disadvantages, it can be seen that the SLM technique is the best possible for fit for the production of prosthetics. The next section gives an introduction on titanium alloys, in particular Ti6Al4V for SLM fabrication because of its widespread usage for biomedical applications.

2.3 Titanium Alloy – Ti6Al4V

Titanium alloys and in particular, Ti6Al4V is the focus of this research for biomedical applications. Titanium based alloys are known for their superior mechanical properties, high strength to weight ratio due to a low density of about 4.43 g/cm³ and biocompatibility when compared to other materials. The cost of the material being a major drawback. Also, titanium based alloys show superior wear resistance, corrosion resistance and high fatigue performance in a biological environment giving it an edge over other materials for biomedical application. In addition to the biomedical industry, Ti6Al4V alloy is used in aerospace, automotive, sports and other major industrial applications [20].

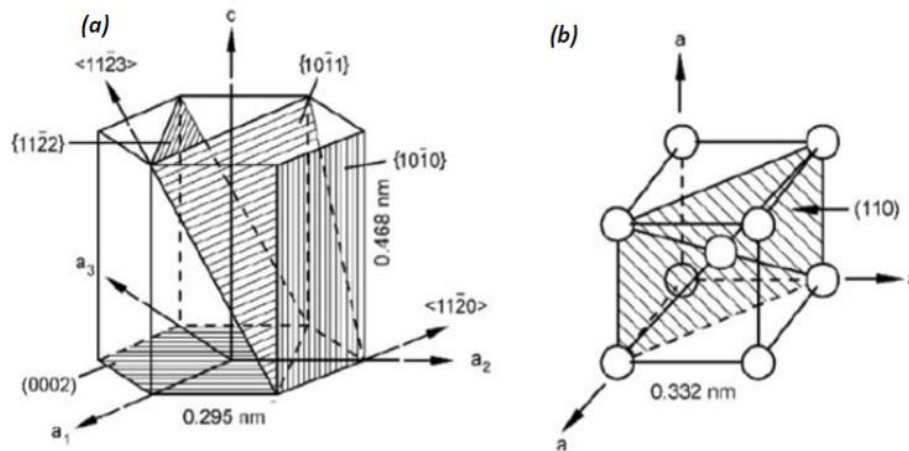


Figure 2.5 The unit cells for (a) α and (b) β phases in titanium. Reproduced from A.A. Antonyamy *et al.* (2012) [21].

The crystal structure of the two equilibrium phases for titanium are shown in Figure 2.5. α is a low temperature phase with a hexagonal close packed (HCP) crystal structure and β is a high temperature phase ($> 882^\circ\text{C}$ for pure Ti) with a body centred cube (BCC) crystal structure [21]. α phase due to its HCP structure is stronger and less ductile due to the close packed nature of the crystal structure. On the other hand, the β phase owing to a larger number of slip planes because of the BCC crystal structure provides ductility. Titanium alloys are classified based on the equilibrium phases that exist at room temperature and their chemical composition into α alloys, near α alloys, β alloys, $\alpha+\beta$ alloys and metastable β alloys. Ti6Al4V is an ($\alpha+\beta$) alloy commonly used for biomedical application. It consists of aluminium which is an α stabiliser, providing strength by solid solution hardening and vanadium which is a β stabiliser, providing ductility by increasing β phase fraction [20]. Vanadium does so by decreasing the β transus temperature.

2.3.1 Open Cell Porous Titanium Structures (Ti6Al4V)

The use of AM processing such as SLM for titanium alloys can be attributed to the fact that they are difficult to machine due to their low thermal conductivity and high reactivity. Also, manufacturing parts by conventional methods such as casting and forging is both expensive and time consuming with a lot of wastage of material in the form of scrap. Thus the use of SLM gained popularity in the manufacturing of Ti6Al4V, especially for biomedical application due to its ability to manufacture complex design geometries such as open unit cell porous structure with a minimal loss of material and finishing required. SLM also enables the ease to fabricate parts or implants based on a patient's requirements [17, 22]. The ability to produce controlled unit cell design porous structures facilitates to engineer parts which could improve the probability of success in orthopaedic application such as bone healing therapies as opposed to random foam structures attained by traditional techniques for the manufacturing of porous parts [18]. Also, by the application of porous design structure in the manufacturing of bone implants, the modulus of the implant can be tailored closer to that of a bone which varies between 4 to 30 GPa depending on the type of bone and the direction of measurement. This is an important criterion to avoid a phenomenon referred to as stress shielding effect. Stress shielding effect results in loosening of the implant due to inadequate transfer of stresses to the adjacent bone as a result of the

mismatch between the stiffness of the implant and the bone [20, 23]. Hence, the research for the manufacturing of open cell porous structure with controlled geometries and different unit cell configuration is gaining importance. A number of researchers have suggested different unit cell configurations and tested their performance.

SLM has enabled the manufacturing of multiple types of unit cell porous structures. Due to their properties and biocompatibility, Ti6Al4V alloy in addition with SLM are apt for implants production as they can be tailored to have mechanical properties similar to that of bones. The high porosity and surface area of the open cell porous structures can be used to perform bio-functional surface treatments to allow bone ingrowth and osseointegration [6, 24-27]. Diamond, truncated cube, truncated cuboctahedron, rhombic dodecahedron and rhombicuboctahedron are different unit cell configurations that have been fabricated using SLM and their properties studied to understand the effect of each unit cell type and their dimensions on the mechanical behaviour of the material [23]. Figure 2.6 shows examples of some unit cell configurations and respective sample specimens that are used to produce porous parts by SLM.

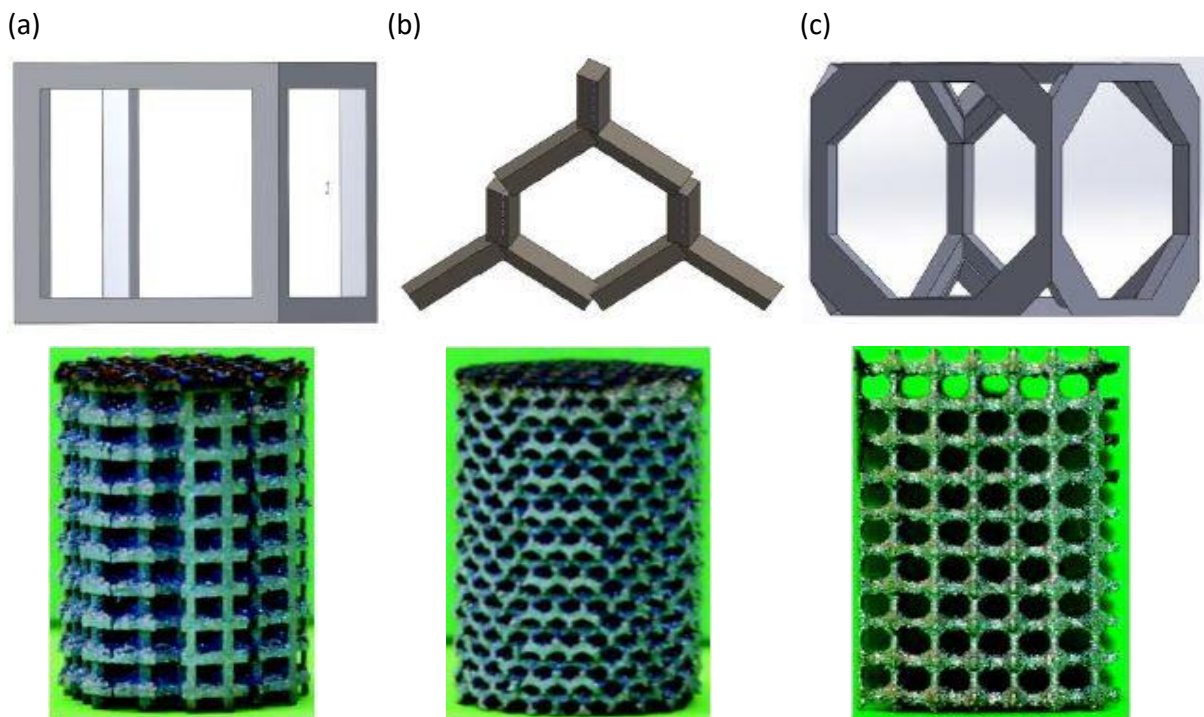


Figure 2.6 Unit Cell configuration (above) and sample specimens (below) for (a) Cube (b) Diamond and (c) Truncated Cube. Reproduced from S. Ahmadi *et al.* (2015) [23].

Porous materials derive their properties from the unit cell in addition to the microstructure and the phase fractions. Porous structures are characterised by the unit cell type, unit cell size and relative density [23]. Surface quality is another factor that influences a number of functional properties of the structure such as frictional properties, heat transfer and mechanical properties. For biological applications, surface roughness has a strong influence on the interaction of the implant and the surrounding which helps bone ingrowth. Hence, an optimal value of roughness is to be attained to ensure a good mix of mechanical properties and surface roughness [18].

2.3.2 Microstructure

The Ti6Al4V consists of two equilibrium phases, α and β . At low temperatures it has a close packed hexagonal crystal structure (hcp) known as α and at temperature greater than the β transus temperature it has a body centred cubic crystal structure (bcc) referred to as β [20]. The microstructure of the Ti6Al4V alloy is a function of the cooling rate or the rate of solidification, based on which it can either be lamellar or globular [12].

In Titanium alloys, the transformation temperature after which only β phase is present is referred to as the β transus temperature. This temperature plays a vital role in the microstructural evolution and thus the heat treatment and processing schedule of the material. In the case of conventional manufacturing methods and to an extent in additively manufactured titanium alloys, the alloys processed/heat treated above the β transus temperature result in a mixture of equiaxed α colonies in prior β grains with some retained β . Heat treatment below in the $\alpha+\beta$ regime have a mixture of lamellar α and β phases. For Ti6Al4V the β transus temperature is between 980-1000 °C based on the composition of the alloy. The volume fraction and nature of α and β phases depend on the alloy chemistry, cooling rate and heat treatments. The phase fraction can be varied by changing either of these parameters based on the application to get the desired properties. For example, a higher cooling rate can result in the microstructure consisting of high volume fraction of non-equilibrium martensite (α') phase with some amount of retained β phase. Whereas, slow cooling to room temperature can result in a combination of majority α phase with β as the remaining volume fraction and no non-equilibrium phases [8, 20, 28]. Figure 2.7 shows a schematic of the cooling curves in Ti6Al4V alloy from the β transus temperature.

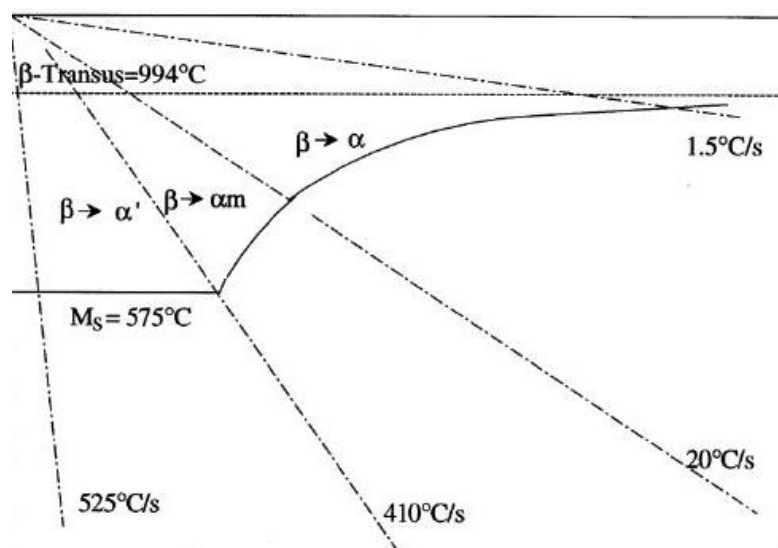


Figure 2.7 Schematic representation of cooling curves in Ti6Al4V alloy. Reproduced from A.A. Antonysamy *et al.* (2012) [21].

2.3.2.1 As-Processed microstructure

The typical microstructure for a Ti6Al4V alloy manufactured by conventional technique consists of globular α phase in $\alpha+\beta$ matrix. Due to the high temperatures, well above the β transus, involved in the process for melting the powder grains and high temperature gradients between

the melt pool and substrate in SLM, the microstructure consists of fine needle like or acicular α' phases. α' has a hexagonal close packed structure. Martensite is formed within the prior β grains which are mostly aligned along the build direction in the case of fully dense samples or sometimes along the strut direction in a porous structure [8, 15, 17, 29]. Another important observation is that the prior β grains during solidification from the liquid phase tend to favour epitaxial growth in $\langle 001 \rangle$ direction with the same crystal orientation as the substrate below. The substrate is of the same material as the fabricated part. This growth direction generally aligns with the AM build direction which is along the path of maximum thermal gradient [8, 17]. Figure 2.8 shows the SEM images of the microstructure of a typical wrought Ti6Al4V alloy and as-processed microstructure for a SLM processed part.

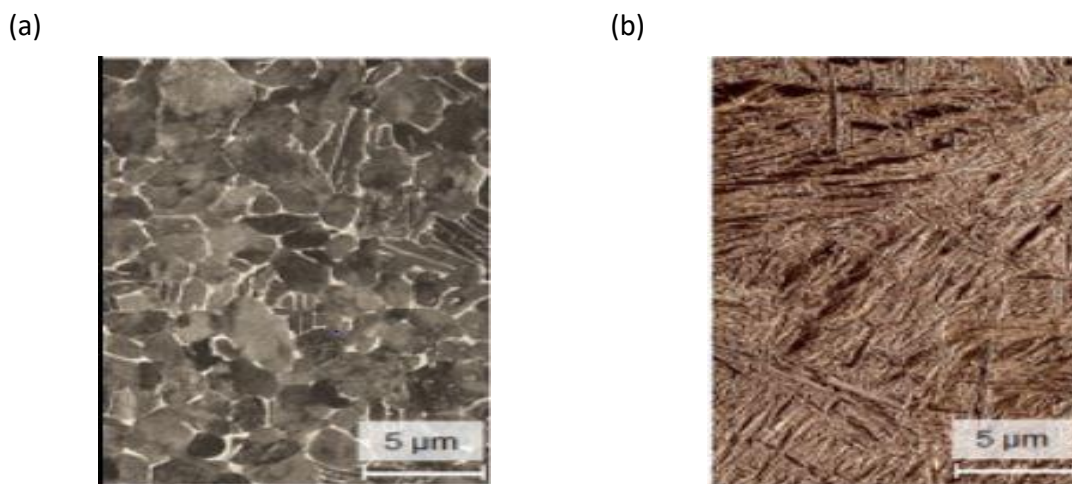


Figure 2.8 (a) Wrought globular $\alpha+\beta$ microstructure (b) SLM as-processed α' microstructure images from SEM of etched surfaces. Reproduced from G. Kasperovich *et al.* (2015) [12].

The as-processed microstructure after SLM constitutes martensite (α'), which is not acceptable for industrial applications as it is brittle in nature. It is known that the microstructure has a close relationship with the mechanical properties of a material. Hence, it is important to control the microstructure during processing or by using post-processing treatments such as annealing or hot isostatic pressing (HIP) to ensure a homogenous and stable microstructure to have a set of desired and acceptable properties for a given application.

2.3.2.2 Microstructure after post-processing

Post-processing is performed on SLM processed Ti6Al4V alloy primarily to reduce the internal stresses as well as to improve the ductility of the structure. It is known that ductility and strength are opposing properties where an increase in one generally results in a decrease in another. Thus, it is important that an optimal post-processing treatment in terms of time and temperature be used. This can help achieve the desired properties in terms of strength and ductility for biomedical applications.

The post-processing heat treatments can be categorised into two regions, one below the β transus temperature referred to as sub-transus or low temperature strategy heat treatment and the other above the β transus temperature referred to as super-transus or high temperature strategy heat treatment [8]. These treatments based on the strategy employed have an effect on the grain size,

grain morphology and phase distribution, especially the amount of β phase in the material in addition to relieving of internal stresses. The focus of this research is on HIP which is generally a sub-transus heat treatment.

2.3.2.2.1 Sub-transus heat treatment

The heat treatment below the β transus temperature has been carried out by a number of researchers in vacuum or an inert atmosphere to prevent the oxidation of the material and also by varying the treatment time and cooling rate to understand its effect on the microstructure. Some of the heat treatment strategies below the β transus temperature used are 700 °C for 2 hours followed by furnace cooling or air cooling [8], 800 °C for 2 hours followed by furnace cooling [30], 700 °C for 1h followed by cooling at a uniform rate of 10 °C /min [12] or two step strategy of annealing at 900 °C for 2 hours followed by another annealing step of 700 °C for 1 hour and then cooling at a uniform rate of 10 °C/min [12]. The effect of the sub-transus treatment is generally to relieve the stresses in addition to transforming the microstructure by gradual decomposition of the as-fabricated fine acicular or needle-like martensite (α') to a mixture of a stable α and β lamellar structure. The sub-transus heat treatment does not significantly affect the grain morphology and gives a lamellar mixture that is present inside the columnar prior β grains [5]. It has been observed that an increase in the temperature results in an increase in the β phase fraction at α phase boundaries. β phase is formed due to the enrichment of the region by vanadium which is expelled during the nucleation of α phase along α' grain boundaries during heating. Increasing the heat treatment residence time also results in α grain coarsening [5, 8]. Van Hooreweder *et al.* (2017) mentions that in the case of porous structures, the stress relieving treatment, generally for the sub-transus treatment in the range of 700 °C, does not change the stress state of the structure as the residual stresses in a porous structure are low. This is because the struts are free to deform. The process only affects the microstructure similar to that of SLM processed fully dense samples [4]. Figure 2.9 shows the microstructure of sub-transus heat treated samples of Ti6Al4V.

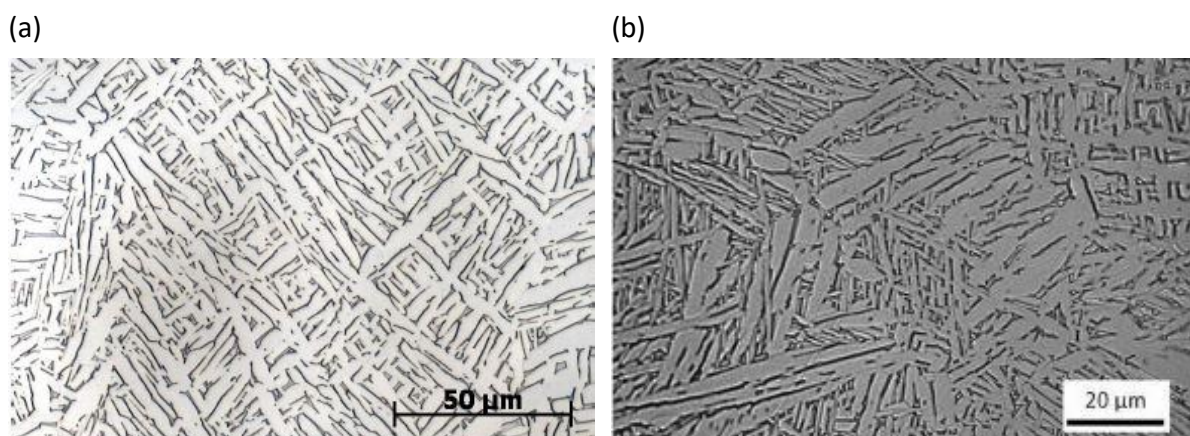


Figure 2.9 Microstructure after sub-transus heat treatment (a) 940 °C for 2 hours followed by furnace cooling [5] and (b) 890 °C for 2 hours followed by furnace cooling [31]. The light regions are α phase and the dark regions are β phase.

2.3.2.2 Hot Isostatic Pressing (HIP)

Hot isostatic pressing (HIP) is a post-processing technique that involves the application of elevated temperatures and isostatic pressure on a material. It is largely done on cast and SLM processed Ti6Al4V alloy to reduce the process induced internal porosity of the structure in order to achieve a fully dense sample or strut. The HIP process is aimed at improving the structural integrity, microstructure and mechanical properties of SLM processed Ti6Al4V alloy for industrial application. The HIP treatment followed is as per the standard values for cast Ti6Al4V alloys at an elevated temperature of 920 °C and pressure of 100 MPa for two hours in an inert gas atmosphere [4, 12, 15, 17]. The HIP treatment is sometimes followed by an annealing step [12]. The effect of the treatment on the microstructure is similar to that of the sub-transus heat treatment as the temperatures are slightly lower than the β transus temperature. The HIP treatment in porous structures results in a microstructure with no fixed orientation. It consists of elongated lamellar α and β phases as seen after sub-transus heat treatment for both porous and fully dense samples [15]. The prior β grains formed due to the high temperature involved determine the size of α grains formed. The only difference from the sub-transus microstructure is the coarser grain size of α phase because of the high temperature which is closer to the β transus temperature. The major advantage of the HIP treatment is that it effectively closes the internal pores present in the structure. In the process, improving the ductility and fatigue life of the structure. For porous structures, it was observed that the amount of pores closed by HIP decreased with the inclination of the struts. The horizontal struts have maximum porosity whereas the vertical struts have nearly zero porosity after HIP treatment [15]. Figure 2.10 shows the microstructure of Ti6Al4V alloy after HIP process.

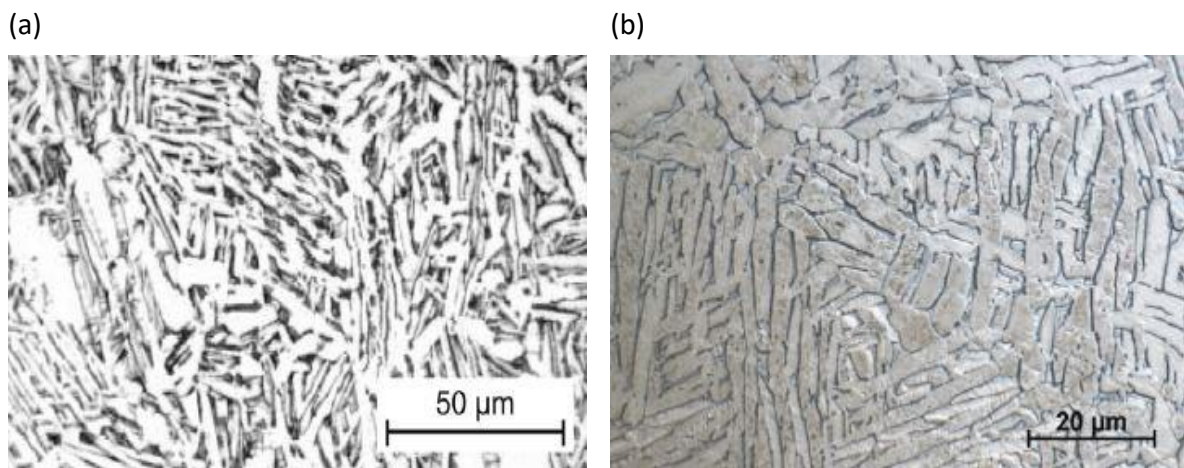


Figure 2.10 Microstructure of HIP processed samples. Reproduced from (a) R. Wauthle *et al.* (2015) [15] and (b) B. van Hooreweder *et al.* (2017) [4].

2.3.3 Surface modification treatments

The surface modification treatments play an important role in determining the mechanical properties of porous structures. They help in reducing roughness by smoothing the struts by removing loosely stuck and partially melted powder particles and in the process improving fatigue life. In addition to this, they provide a micron level roughness of up to 10 μm that helps in better

osseointegration and bone on growth in implants [32]. Some of the commonly used surface modification techniques on titanium implants include chemical etching, shot peening, sandblasting and Sandblast, Large-Grit and Acid etching (SLA) to name a few. Among the mentioned techniques, chemical etching using HF solution is the most widely used on porous structures [4, 18, 19, 33]. The reason for this being the expected homogeneous treatment throughout the porous structure. This is because the acid based solutions can penetrate through the interconnected pores in lattice structures. The influence of chemical etching on lattice structures with HF solutions of varying concentrations, compositions and time has been analysed by researchers [18, 19, 33]. The influence of chemical etching by 0.5 ml HF and 50 ml water solution for an immersion time of 10 minutes on fatigue properties has been shown by B. van Hooreweder *et al.* (2017) [4]. Figure 2.11 shows the image of a representative porous structure before and after chemical etching. It should be noted that in this study [4], the SEM images are taken from the top surface and no information is available regarding the effect and uniformity of etching process on the core of the samples.

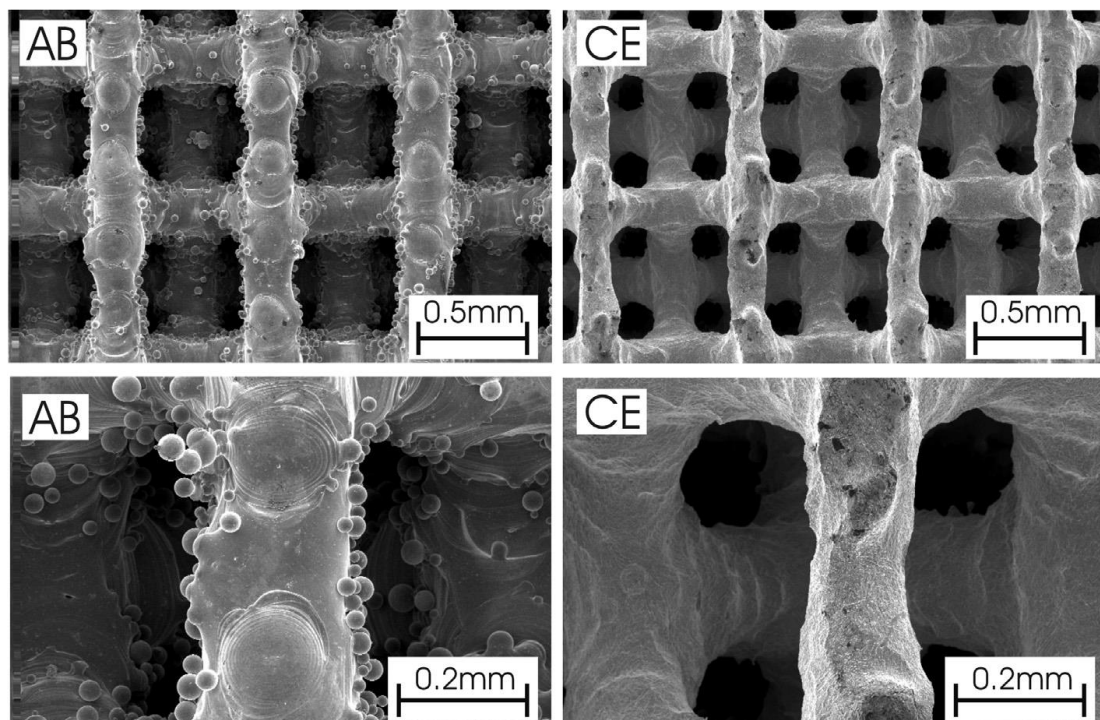


Figure 2.11 SEM images of as-processed (left) and chemically etched (right) samples. Reproduced from B. van Hooreweder *et al.* (2017) [4].

From Figure 2.11, the removal of loosely stuck and partially melted powder particles with the smoothing of the surface is observed. This results in a reduction in roughness which can improve the fatigue properties of the structure. S.A. Yavari *et al.* (2014) studied the effect of acid-alkali and alkali-acid-heat treatment on the mechanical properties of porous structures. These are commonly used surface treatments for bio-functionalising which also reduce the surface roughness [24].

Shot peening is another technique used on fully dense samples to impart compressive stresses on the surface in addition to removal of loosely stuck powder particles. The compressive stresses

help in preventing crack propagation at the surface. The shot peening process is a preferred choice for an implant to be designed with medium to high cycle fatigue and low production costs [34]. Sandblasting is another commonly used technique for imparting a micron level roughness on the structures. The usage of sandblasting for different grit size and abrasive particle type such as Al_2O_3 , TiO_2 has been studied on fully dense samples [32, 35]. A positive influence in terms of imparting a roughness favouring osseointegration and bone on growth is observed. But there are disadvantages to the sandblasting technique. Primarily, the effect of residual contamination of the abrasive particles on the surface of the structures. Hence, the sandblasting technique is generally followed by an acid etching step to dissolve or remove such contamination from the surface. Their application has been limited to fully dense samples and no literature on its influence on porous structures was found.

2.3.4 Mechanical Properties

The mechanical properties, namely compression and fatigue to understand the effect of the post-processing treatments as compared to as-processed SLM produced Ti6Al4V alloy has been shown in this section. The post-processing is done to bring the properties as close to or even improve them as compared to parts manufactured by conventional techniques such as casting or forging. The main reason for the post-processing treatments is to improve the mechanical properties of the material for industrial relevance with the focus in this research on biomedical applications. SLM processing results in anisotropic properties due to the growth of the prior β grains along the building direction as a result of the high thermal gradient. The mechanical properties discussed in this section are along the building direction.

2.3.4.1 Compression Properties

Compression testing is an important testing method to understand the mechanical behaviour of the SLM processed Ti6Al4V alloy for biomedical application. The implants are constantly subjected to compression loading. Compression test on porous samples with different unit cell design, relative density and post-processing treatments have been performed to establish their effect on the behaviour of the alloy. The compression tests were carried out in accordance to the ISO 13314 [4, 15, 23, 36]. Table 2.1 shows the results of compression test on diamond unit cell porous structure in the as-processed and post-processed conditions. Based on the standard the following data is determined from the σ - ϵ curves:

- Maximum compressive strength (σ_{\max}) which corresponds to the first maximum in the σ - ϵ curve.
- Plateau stress (σ_p) taken as the arithmetic mean of the stresses between 20% and 40% compressive strain.
- Energy absorption which is the energy required to deform a specimen to a certain strain by measuring the area under the σ - ϵ curve up to a strain of 50%.
- Compressive offset stress (σ_{OYS}) which corresponds to the compressive yield strength given by the compressive stress at a plastic compressive strain of 0.2%.
- Elastic gradient ($E_{\sigma_{20-70}}$) as the gradient of the elastic straight line between two stress values, namely σ_{20} and σ_{70} .

Table 2.1 Compression test results of SLM processed and post processed Ti6Al4V alloy. Reproduced from B. van Hooreweder *et al.* (2017) [4].

	Relative Density (ρ_{rel})	Internal Porosity (%)	$E_{\sigma 20-70}$ (GPa)	σ_{max} (MPa)	σ_y (MPa)	σ_{pl} (MPa)
As-processed	34.42	1.59	4.301	118.68	90.11	71.98
As-processed	37.42	1.19	4.921	128.00	101.50	74.24
650°C/4 h/Furnace cooling (SR)	34.31	0.92	4.941	117.73	103.59	80.01
HIP	39.93	0.60	6.658	146.85	118.97	133.78
HIP + CE	31.12	0.73	4.176	88.64	79.19	97.70

It can be observed from Table 2.1, an increase in the relative density results in an increase in the strength of the porous structure. Thus by varying the structural density, the properties of the SLM processed Ti6Al4V part can be tailored to the properties of the bone it is replacing. This can be observed in the HIP processed sample as well which shows high strength with a small increase in the relative density. This increase in strength can also be attributed to the decrease in process induced internal porosity of the samples due to the HIP treatment. The compressive failure in porous unit cell structures occurs by successive failure of the layers. In the case of the as-processed samples, the failure is brittle in nature for each layer with lower strain at fracture and higher strength when compared to the heat treated or HIP samples [4]. The stress state of the porous samples is cyclic in nature with the as-processed samples undergoing a sudden decrease in the stress with the failure of each layer when compared to a more dampened stress phenomenon showing plastic deformation in the case of heat treated and HIP samples [4, 23].

2.3.4.2 Fatigue

Fatigue life is a dynamic property of utmost importance for biomedical applications to ensure a prolonged life of the implant. The fatigue life of porous and fully dense test samples differ in nature. For porous samples, the failure of the structure is dependent on the unit cell and their relative density in addition to the microstructure. Other fatigue influencing factors that need to be considered that are inherent to SLM processing are the surface roughness, porosity, residual stresses and stress concentration sites. These factors play a decisive role in determining the fatigue life, especially, surface roughness and porosity that act as sites for crack initiation and ultimately the failure of the structure [4, 30]. Thus, post-processing techniques such as HIP for closing the pores and chemical etching with different concentration and time to reduce the surface roughness have been used to analyse its effect on the fatigue behaviour of the SLM fabricated Ti6Al4V alloy porous structures. It is important to consider even the mass loss that occurs in the struts due to the chemical etching process involved in reducing the surface roughness of the material [4, 19]. Figure 2.12 shows a S-N plot for the fatigue behaviour of as-

processed and post-processed SLM Ti6Al4V open porous biomaterial with a diamond unit cell design. The fatigue tests have been carried out by subjecting the samples to a constant amplitude loading in compression-compression with a load ratio, $R = 0.1$ and frequency of 15 Hz [4]. Note that the stress taken here is the local stresses generated in the struts to understand the fatigue behaviour with respect to the struts which are critical in the fatigue behaviour of the lattice structures.

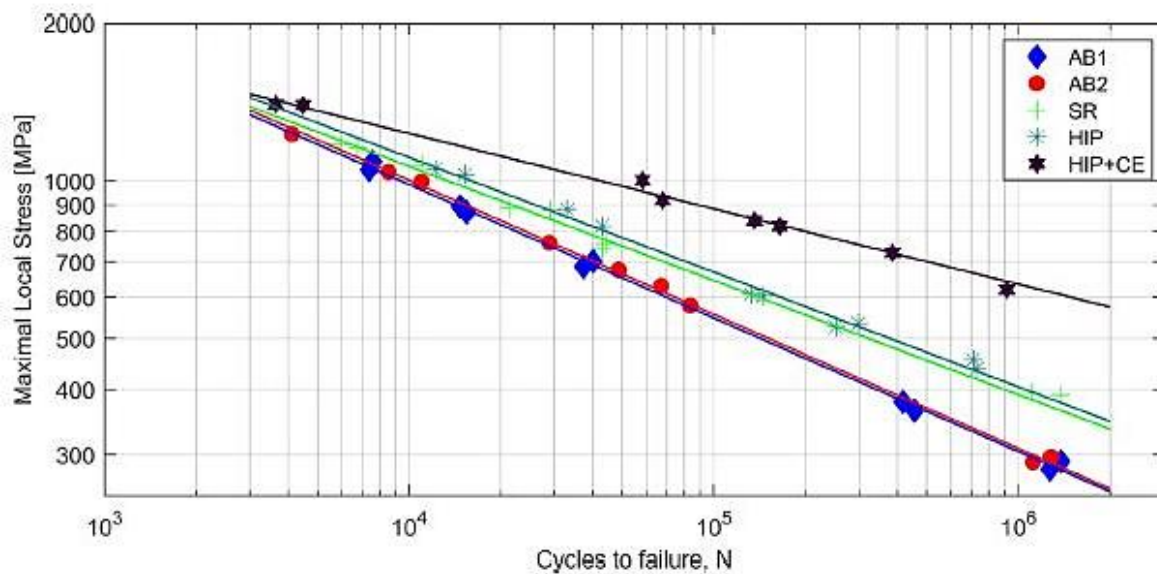


Figure 2.12 Fatigue behaviour (S-N curve) of SLM processed and post-processed Ti6Al4V porous structures. Reproduced from B. van Hooreweder *et al.* (2017) [4]

From Figure 2.12, it can be observed that the post-processing treatments have a positive effect on the fatigue behaviour of the structures. This can be attributed to the change in the microstructure due to the heat treatments involved and morphology due to the HIP and chemical etching (CE) process carried out. The chemical etching process is carried out by immersion in a HF based solution (2% HF solution for 10-12 minutes) for the HIP sample. The sample with HIP followed by chemical etching shows the highest resistance to fatigue failure based on the S-N curve. This is due to the reduction in surface roughness and porosity and a change in microstructure to a stable lamellar $\alpha+\beta$ microstructure from the non-equilibrium, brittle α' microstructure [4]. The better fatigue resistance is also due to the decrease in defects resulting from minimised porosity and higher volume fraction of β phase when compared to as-processed structures [30].

2.4 Conclusion

The literature review was carried out to understand the progress made in terms of SLM and its usage for Ti6Al4V alloy. The literature review can be summarised as:

- SLM processing is a novel technique for manufacturing of implants for biomedical applications using Ti6Al4V alloy. However, it has its associated process induced defects and imperfections.

- A lot of research has been carried out in terms of parameter optimisation and post-processing techniques to minimise the process induced defects such as roughness and porosity to attain superior mechanical properties.
- Heat treatment can be classified into two regimes based on the β transus temperature and the effect on properties has been accounted to a large extent in literature. On the other hand, it still shows no repeatability in the properties for a given heat treatment due to the high sensitivity of the SLM process to the machine, powder type and environment.
- HIP has become an important post-processing treatment to reduce the process induced porosity of the structure in order to improve fatigue life in addition to relieving internal stresses and obtaining a stable and controlled microstructure at room temperature.
- In porous structures, unit cell design, relative density and post-processing treatments are important factors that play a decisive role in the mechanical properties of the structure. Hence, a lot of research is targeted towards it to improve the quality of SLM processed lattice structures by post-processing and varying the design to change the unit cell type and relative density.
- The post-processing of porous structures is predominantly aimed at diamond unit cell due to their relatively less complexity and isotropic structure.
- Different design parameters, structure density, building orientation and their influence have been analysed to a small extent in terms of fatigue life and compression properties.
- Surface modification techniques are important in increasing the fatigue life and imparting a micron level roughness to the structure.

2.5 Research Objective

Based on the literature review, there is a lack of reproducibility of the results for the as-processed samples. This is due to the sensitivity of the SLM process to the processing parameters and the processing environment. Additionally, in this study, a new SLM vector based approach has been investigated on as-processed and post-processed conditions. It should also be noted, that the literature review provided in Chapter 2 is based on conventional STL based approach, which will serve as a reference point for comparative studies presented in this thesis. Hence, the main research objective for this thesis is to bridge the gap and find the most optimal solutions in terms of:

1. Investigating post-processing techniques, namely, hot isostatic pressing (HIP) and surface modification for Ti6Al4V lattice structures manufactured by vector based approach.
2. Investigating the relationship between the microstructure and mechanical properties, namely compression and fatigue life before and after post-processing.
3. Comparison between the vector based and STL based approaches for the as-processed samples.

The use of HIP samples for testing and surface optimization is based on the results of the literature review as well as preliminary analysis carried out on various heat treatment regimes. Based on literature, the HIP samples showed the most improved mechanical properties in the post-processed conditions. The preliminary analysis carried out led to a similar conclusions of using HIP for further surface modification analysis. More information regarding the preliminary analysis can be found in the conference article to be presented at ICSMR-2017, S.M. Ahmadi *et al.* (2017) [37].

Chapter 3 Experimental Section

The SLM processed Ti6Al4V samples manufactured by the vector based approach are tested in the as-processed and post-processed condition to investigate the influence of post-processing on the properties of the material. Also, a comparative study between the as process vector and STL approach based samples was carried out using the mentioned testing conditions and techniques.

3.1 Material and Methods

A plasma atomised, spherical Grade 23 Ti6Al4V ELI powder acquired from AP&C (Advanced Powder and Coatings Inc., Boisbriand, Canada) with a particle size range of 10 to 40 μm was used. The extra low interstitial (ELI) grade is used in this study. Cylindrical specimen with an open cell porous structure consisting of a diamond unit cell were manufactured using Selective Laser Melting (SLM). Figure 3.1 shows the cylindrical test sample and diamond unit cell analysed in this study.

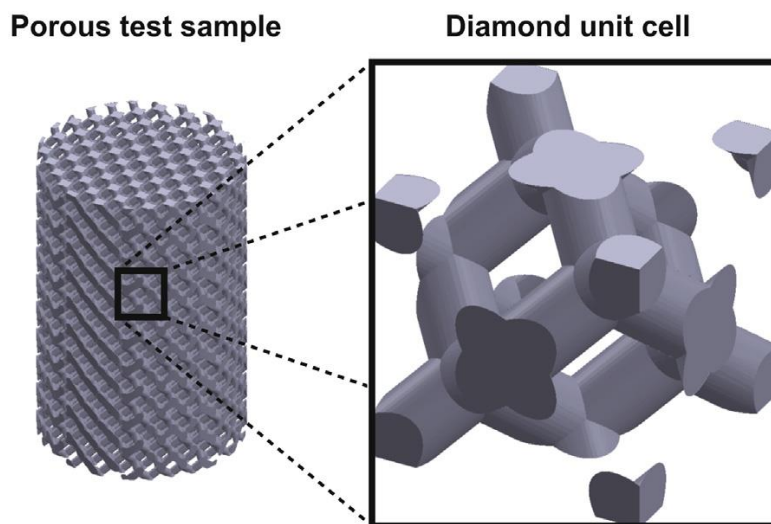


Figure 3.1 3D representation of the porous test sample and diamond unit cell. Reproduced from R. Wauthle *et al.* (2015) [15].

SLM specimens with dimensions of 15 mm diameter and 20 mm height were produced using the commercially available SLM125 machine (Realizer GmbH, Borcheln, Germany) on a Titanium substrate. The SLM machine was equipped with an YLR laser with a maximum power output of 400 W and wavelength range of 1070 ± 10 nm. The specimens were prepared in the SLM building chamber flushed with argon gas to reduce the oxygen level to below 0.2 %. The substrate is

preheated to 100 °C. The process parameters used for the fabrication of the specimens included a scanning time of 550 μ s and laser power of 128 W. The cylindrical lattice structure was sliced into layers of 50 μ m.

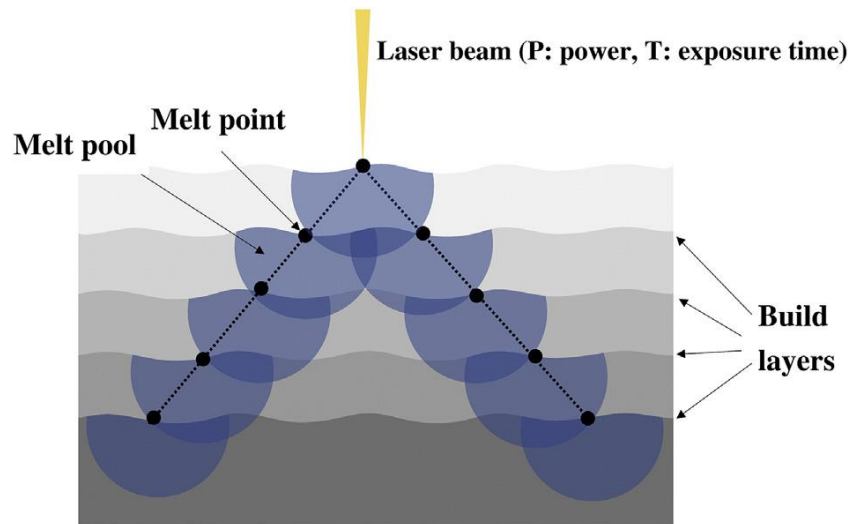


Figure 3.2 Schematic of the vector based approach for the manufacturing of porous structures using SLM. Reproduced from S.M. Ahmadi *et al.* (2017) [13].

The specimens were designed using the RDesigner software (Realizer GmbH, Borchten, Germany) based on vector based approach explained by S.M. Ahmadi *et al.* (2017) [13]. The size of the unit cell edge was 1 mm and consisted of 16 struts, each defined as a vector with the angle between the struts equal to 109.5°. In the vector based method, the strut thickness is a function of the energy density supplied at each point as opposed to the predefined strut thickness based on the STL file fed to the system observed in the STL driven method. In the vector based approach, no STL files are created for the manufacturing of the sample. Instead, the laser beam follows the vector path describing the porous structure and selectively melts the point of intersection of the strut vector and sliced layer along the central axis of the to-be manufactured strut as shown in Figure 3.2. Thus, the strut thickness depends on the laser power and scanning time as they determine the size of the melt pool at each intersection point. The laser is switched off between consecutive jumps.

3.2 Post-processing

The post-processing consists of HIP and surface modification treatment either individually or in combination. The as-processed samples are used as reference sample for comparison with the post-processed samples. For the HIP treatment, the samples were heat treated at a temperature of 920 °C for 2 hours with the simultaneous application of pressure at 100 MPa in an inert atmosphere. The samples were furnace cooled at a rate of 10 °C/minute.

The HIP samples were then subjected to surface modification treatments using chemical etching and sandblasting. Chemical etching is performed on the HIP samples using a solution of 50 ml water, 25 ml HNO₃ (\geq 65 % volume) and 5 ml HF (40 % volume) by immersion for 150 seconds (represented by HIP+CE). Constant stirring was performed during immersion. The immersion was

followed by cleaning in an ultrasonic bath with ethanol for 10 minutes. A number of immersion times and etchant compositions were experimented with, but the above mentioned solution and immersion time yielded the best results.

For sandblasting, Al₂O₃ abrasive particles with a size in the range of 180-250 µm were used on the HIP samples (represented by HIP+SB). The sandblasting was performed manually using a Micropeen equipment at a working pressure of 3 bars. Each specimen was sandblasted for a time of 2.5 minutes. The distance between the gun and sample maintained at around 15 cm. Table 3.1 gives an overview of all the post-processing conditions and samples used in the study.

Table 3.1 Overview of the samples used for testing in this study.

	Post-processing treatment	Surface modification treatment	Designated by
As-processed	-	-	as-processed / AB
Hot Isostatic Pressing	920 °C/100 MPa/2 hours/inert atmosphere	-	HIP
Chemical etching	HIP	Immersion in 50 ml H ₂ O, 25 ml HNO ₃ and 5 ml HF solution for 150 seconds.	HIP+CE
Sandblasting	HIP	Sandblasted using alumina abrasive particles of size 180 to 250 µm.	HIP+SB

3.3 Morphological Characterisation

Dry weighing technique was used to determine the relative density of the open cell porous samples. Prior to the dry weighing, the specimens were cleaned using ethanol in an ultrasonic bath for 5 minutes. To determine the relative density, the dry weight of the porous specimen was divided by the theoretical weight of a solid specimen taking 4.43 g/cm³ as the theoretical density for Ti6Al4V ELI [23].

For roughness optimization, a qualitative approach was used by taking images of the sample before and after chemical etching to establish the amount of reduction in strut thickness using the table top SEM, Joel JSM-IT100. An average of 20 struts from randomly picked samples are used in the quantification of thickness reduction. The samples were also weighed and relative density determined by the mentioned approach to comprehend the effect of chemical etching and sandblasting on the relative density. In addition to this, the process induced internal porosity in the struts of the samples were calculated using the Keyence VHX5000 and the inbuilt VHX measurement software.

3.4 Microstructural and Hardness Analysis

One representative specimen from the as-processed and post-processed conditions (HIP, HIP+CE and HIP+SB) was selected for microstructural and microhardness analysis. The specimens were first embedded and cut to view the top, middle and cross section. Following which the embedded samples were ground (SiC 320 and MD Largo 9 μm) and then polished (MD Chem with OPS solution 0.04 μm). The samples were etched by immersion for 12 seconds in a 50 ml distilled water, 25 ml HNO_3 and 5 ml HF solution. The samples were observed using an optical microscope, Olympus BX60M Trinocular Inspection Microscope and Keyence VHX5000. The images were taken for top, middle and cross section of the samples as shown in the Figure 3.3.

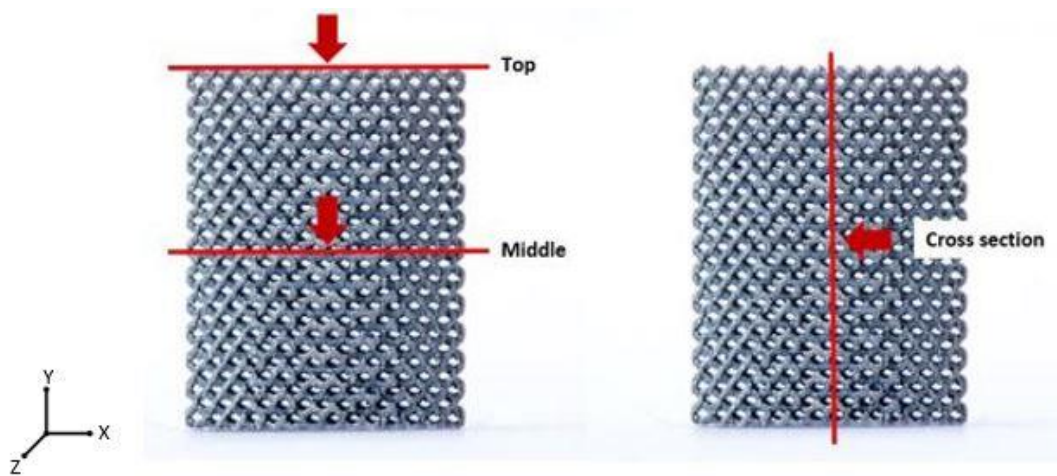


Figure 3.3 Schematic representation of the top, middle and cross section location of the samples.

The microhardness measurements were carried out using an automated Vickers hardness machine, Dura Scan (Steurs) with a load of 0.3 kgf. The hardness measurements were carried out along the cross section of the sample to analyse the influence of the subsequent layer deposition and the thermal gradient on the samples.

3.5 XRD Analysis

XRD analysis was carried out to determine the phases present in the as-processed and post-processed conditions of the samples. The analysis was performed with the Bruker D8 advance diffractometer using a $\text{Co K}\alpha$ radiation. The step size used was $0.034^\circ 2\theta$ with 45 kV and 35 mA current in a 2θ range of 20° - 120° .

In addition to this, the influence of sandblasting to create compressive stresses on the strut surface was analysed using the $\sin^2 \psi$ method as explained in [38]. The same setup was used for the measurements with a Eulerian cradle with parallel beam geometry but with a step size of $0.03^\circ 2\theta$ for the Ti {104} reflection at 115° in a 2θ range of 104° - 117° . The stress measurements were carried out using the elastic constants for pure titanium available in the database Xpert Stress. The Poisson's ratio and young's modulus used were 0.361 and 120.2 GPa respectively.

3.6 Static Mechanical Testing

Compression tests were carried out on the porous samples for the as-processed and the post-processed conditions on the Zwick Z100 (100 kN load cell) test machine. The load was applied at a uniform rate of 1.8 mm/minute with an initial preload of 10 N for a holding time of 10 seconds. The tests were continued for a maximum compression of 80 % or a maximum compressive load of 50 kN, reaching either stopped the test. 3 samples from each set, namely, as-processed, HIP, HIP+CE and HIP+SB were tested for compression and the stress-strain data analysed in accordance with the ISO 13314:2011 standard for porous materials [36]. The compressive tests results were plotted in σ - ϵ curves from which the maximum compressive strength (σ_{max}), plateau stress (σ_p), energy absorption, compressive offset stress ($\sigma_{0.05}$) and the elastic gradient ($E_{\sigma 20-70}$) were determined.

3.7 Fatigue Testing

Compression - compression fatigue tests were performed on the as-processed and post-processed samples. The high cycle fatigue tests were stress controlled with a load ratio of $R=0.1$ and frequency of 15 Hz. A sinusoidal wave form was used for the load. Two samples from each set were tested for different load criterion determined with respect to the compressive offset stress obtained from the σ - ϵ curve for each sample type. If a deviation of greater than 40 % for the number of cycle to failure was observed, additional samples were tested. The tests were carried out on an Instron Electropuls E10000 machine with a 10 kN load cell as shown in Figure 3.4. Based on the experiments, S-N curves were plotted and a power law curve fitted for the data.

The power law is denoted by the equation $y = ax^b$. In the equation, x is the number of cycles to failure, y is the normalised stress, a is a constant and b is the power law exponent. The power law shows that a change in the normalised stress value results in a proportional relative change in the number of cycle to failure. Since, the power law exponent is negative, the change in the number of cycles shows a proportional relative decrease with an increase in the applied load during fatigue. The coefficient of determination, R^2 value is used to show the goodness of the fit of the S-N curve. The value being equal to 1 shows that the dependent variables used in the power law can be predicted without any errors or deviation from the independent variables. The closer the R^2 value is to 1, the better is the fit of the plot to predict the behaviour of the samples.



Figure 3.4 Instron Electropuls E10000 used for fatigue testing.

The precise moment for failure is difficult to estimate in a compression-compression fatigue test and hence, failure was defined by a loss in stiffness of 90 % as seen in previous fatigue studies by S.A. Yavari *et al.* [39, 40]. The test was stopped at 10^6 cycles irrespective of failure and the result was regarded as the maximum limit for this study.

Chapter 4 Results

4.1 Morphological Characterisation

The morphological characterisation includes the measurement of relative density of the sample based on the dry weighing method and the process induced internal porosity (defects) of the samples from the optical images.

4.1.1 Relative Density (ρ_{rel})

The results for relative density are shown in Table 4.1. A minimum of 10 samples for each type were used in the measurement of the relative density using the dry weighing technique.

Table 4.1 Relative density and internal porosity of the samples.

Specimen Type	Relative Density (%)
As-Processed	31.89 ± 0.58
HIP	32.01 ± 0.43
HIP + CE	27.42 ± 0.33
HIP+SB	31.24 ± 0.36

As seen in the above table, the relative density of the samples after HIP did not vary much and are within the standard deviation of the as-processed samples. Thus, the relative densities did not change after HIP. Only significant reduction in relative density is because of the chemical etching process for the HIP+CE samples. This is because of the removal of material from the etching process.

4.1.2 Process induced internal porosity

Table 4.2 Statistical data for internal porosity of the samples.

Sample Type	Internal Porosity (Area %)	Mean Pore size (μm^2)	Median (μm^2)	Maximum Area (μm^2)	Minimum Area (μm^2)	Maximum Diameter (μm)	Minimum Diameter (μm)
As-processed	1.16 \pm 0.57	74.56 \pm 270.96	4.1	3200.9	0.8	63.84	1.01
HIP	0.13 \pm 0.12	15.40 \pm 35.03	2.85	211.3	0.8	16.40	1.01
HIP + CE	0.13 \pm 0.13	7.04 \pm 21.33	0.5	184.1	0.2	15.31	0.50
HIP + SB	0.15 \pm 0.11	8.25 \pm 25.33	0.6	238.7	0.2	17.43	0.50

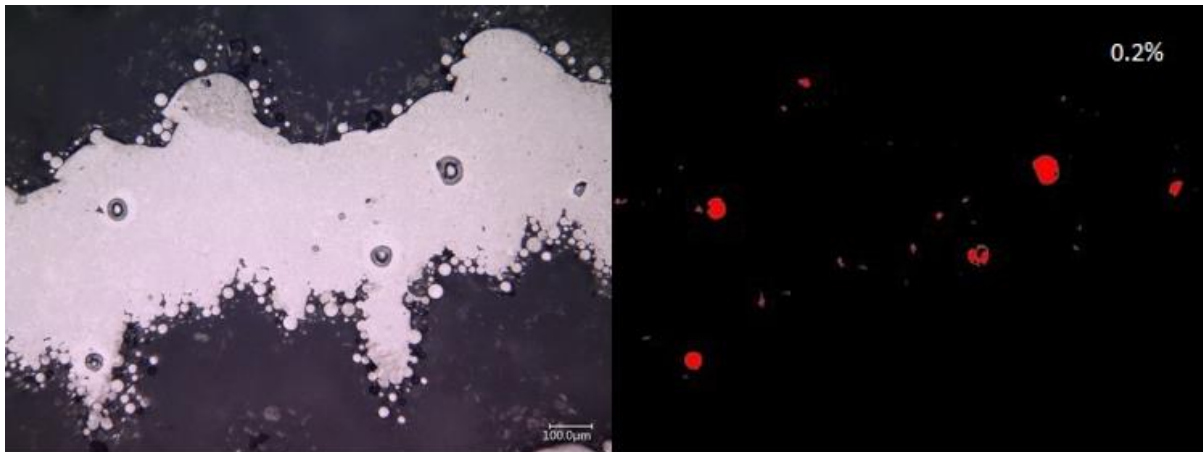


Figure 4.1 Porosity measurements for as-processed sample using the Keyence VHX Microscope.

Table 4.2 shows the results and statistical data based on the pore size and areas obtained from the images of the polished samples. From the above table, it is clear that the HIP treatment results in a decrease in the internal porosity of the samples. This is due to the closing of pores by the application of pressure during HIP. The as-processed sample show a high percentage of internal porosity. It is expected that a reduction in internal porosity can help improve the fatigue life and strength of the studied samples by decreasing the number of stress concentration sites. The process induced porosity reduced by 88.80 % after HIP of as-processed samples. Figure 4.1 shows an example of the usage of the contrast between the pores and material to determine the porosity of the sample with the help of the VHX software.

4.1.3 Effect of chemical etching

The effect of chemical etching with respect to a reduction in relative density, caused by removal of material by the etching process has been shown in Table 4.1. In addition to this, thickness reduction and qualitative observations were made on the top surface (as shown in Figure 3.3) of representative samples.

Table 4.3 Influence of chemical etching on the strut thickness.

Sample Type	Etching Time (seconds)	Strut Thickness before CE (μm)	Strut Thickness after CE (μm)	Reduction in Thickness (%)
HIP	150	229.89 ± 9.41	187.68 ± 10.10	18.36

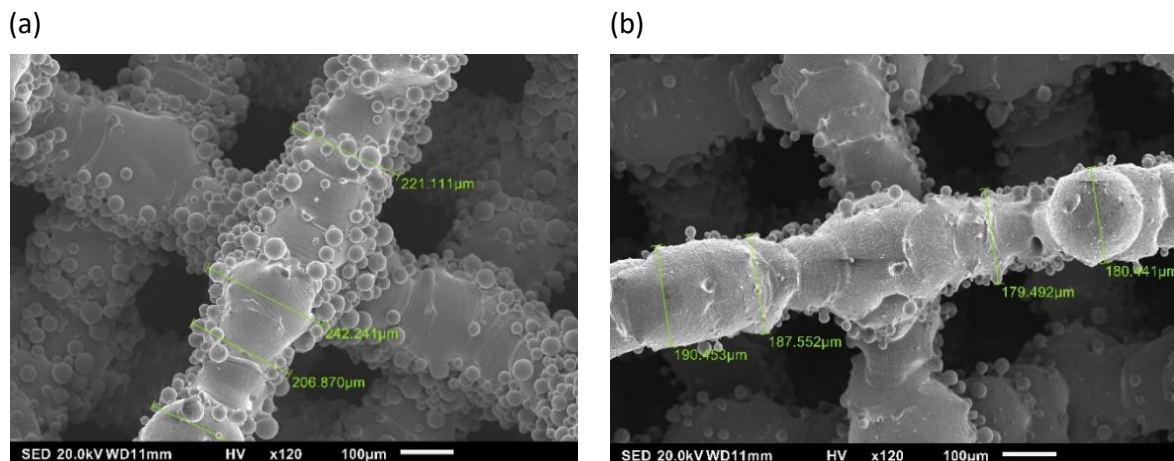


Figure 4.2 Effect of chemical etching on HIP Sample (a) Before CE and (b) After CE.

The chemical etching process results in a decrease in strut thickness of HIP sample by 18.36 % and removal of loosely stuck and partially melted powder particles from the strut surface as seen in Figure 4.2 and Table 4.3. The removal of loosely stuck and partially melted powder particles is important to ensure that there is no contamination during application as an implant. They can detach themselves during loading and contaminate the surrounding. Also, the removal helps reduce the surface roughness. The images are taken from the top surface of a representative HIP and HIP+CE sample along the XZ plane before and after the chemical etching process and not from the core of the samples.

Figure 4.3 shows the images taken from the HIP+CE samples along the middle (as represented in Figure 3.3) to see the influence of chemical etching along the interiors of the sample. It was observed that the chemical etching treatment had no effect at the core of the sample and the material removal was limited to a distance of around 1.5 to 1.7 mm as shown in Figure 4.3 (a) by the shaded region from the edges for the representative sample used in the qualitative analysis. This indicates that the chemical etching technique for our samples has to be optimised. The possible reasons for the lack of optimisation of the chemical etching and recommendations to improve the efficiency of the process will be discussed in Chapter 5.

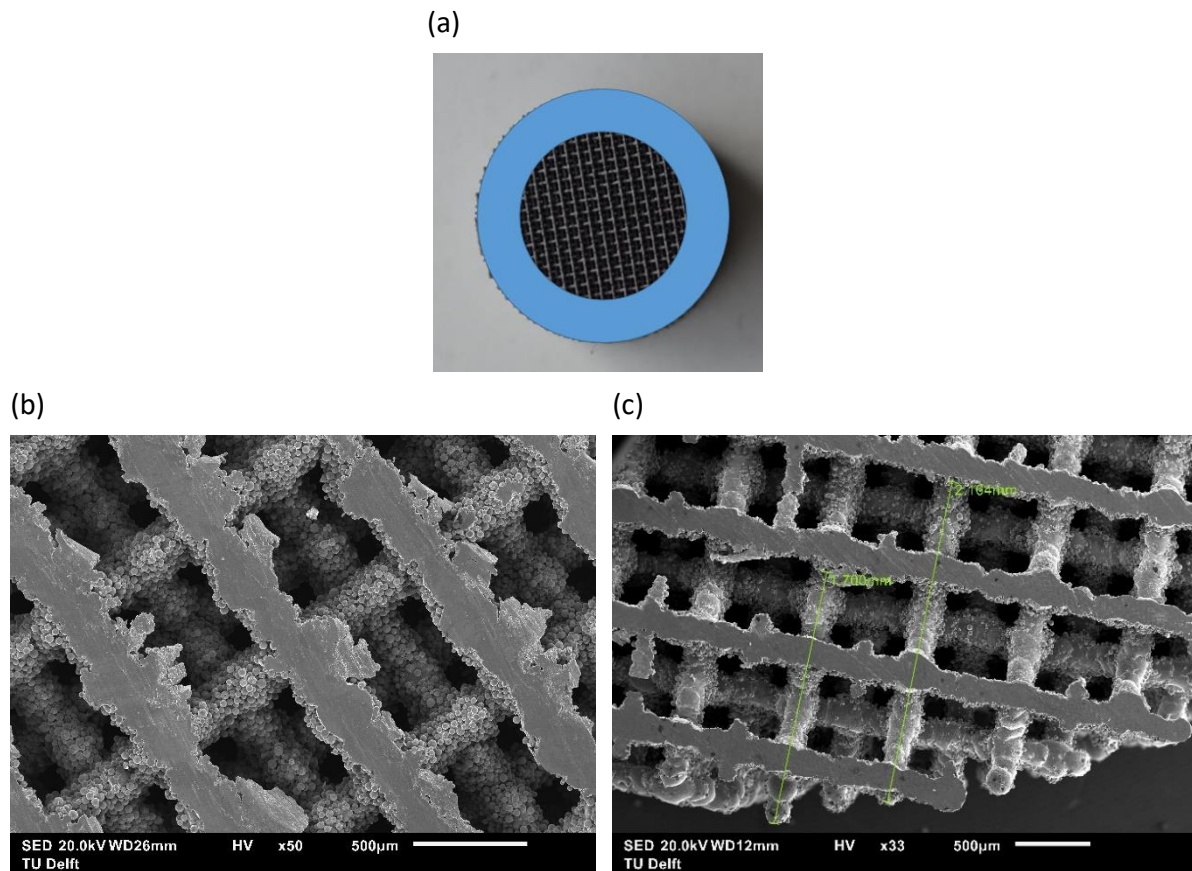


Figure 4.3 (a) Shaded area represent the region affected by chemical etching. SEM images from the middle of the sample (b) core and (c) edges of the sample after chemical etching.

4.1.4 Effect of sandblasting

The effect of sandblasting on the thickness of the struts and the percentage reduction compared to HIP samples is shown in Table 4.4. As can be seen, sandblasting results in strut thickness reduction similarly to chemical etching. Furthermore, it was found that there is no drastic reduction in relative density after sandblasting, as the amount of material removal is around 0.2 grams from its initial weight.

Table 4.4 Influence of sandblasting on the strut thickness.

Sample Type	Strut Thickness before SB (μm)	Strut Thickness after SB (μm)	Percentage Reduction (%)
HIP	225.27 ± 9.56	179.10 ± 11.66	20.50

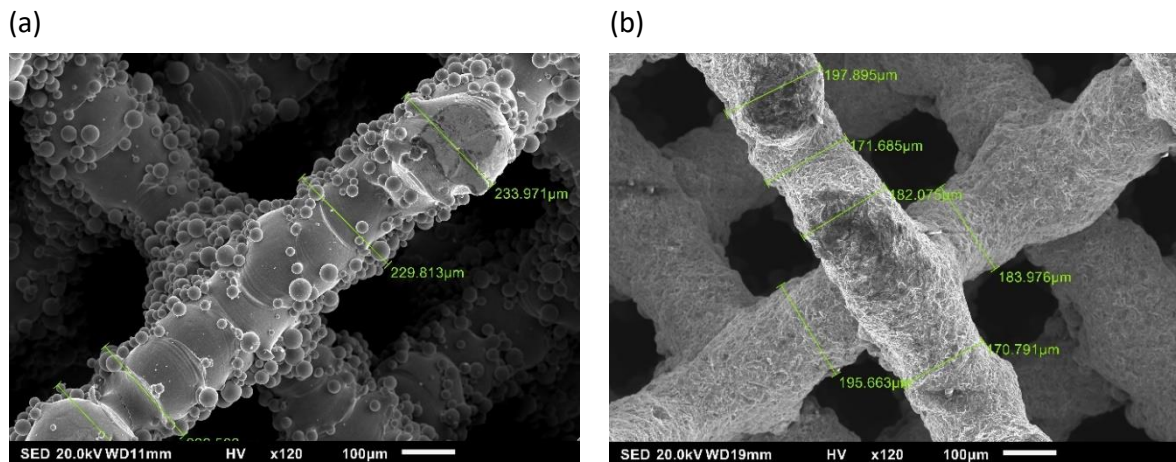


Figure 4.4 Effect of sandblasting on HIP samples (a) Before SB and (b) After SB.

Similar to chemical etching, sandblasting results in the removal of loosely stuck and partially melted powder particles from the strut surface and in the process reducing the strut thickness of the HIP+SB sample by 20.50 % as shown in Table 4.4 and Figure 4.4. The images were taken from the top of the HIP and HIP+SB samples along the XZ plane and not from the core of the samples.

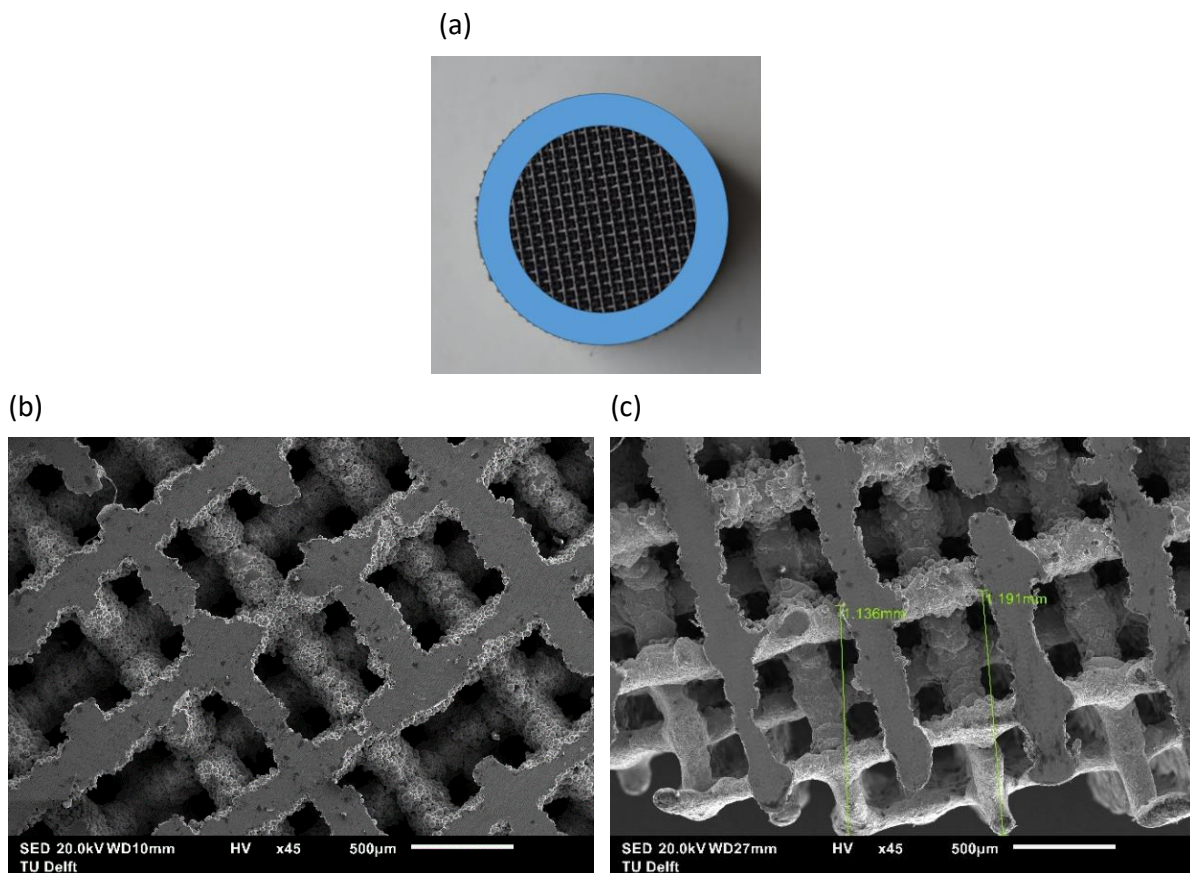


Figure 4.5 (a) Shaded area represents the area affected by sandblasting. SEM images from the middle of the sample (a) core and (b) edges of the sample after sandblasting.

Figure 4.5 shows the images taken after sandblasting for the HIP+SB representative sample from the middle (as represented in Figure 3.3) to show the influence of sandblasting on the core of the sample. It can be observed that the sandblasting had no effect on the interior as shown in Figure 4.5 (a). The effect of material removal is limited to a distance of 1.1 to 1.2 mm as shown by the shaded region from the edges for the representative samples taken for qualitative analysis. The possible reasons for non-uniform material removal as well as proposed solution will be discussed in Chapter 5.

4.2 Microstructure and Hardness

4.2.1 Microstructure

The microstructure for the as-processed and the post-processed condition are shown in Figure 4.6. From Figure 4.6 (a), it can be seen that the as-processed microstructure consists of the non-equilibrium martensitic phase, α' having fine acicular or needle like shape. For the as-processed microstructure, the shape and size of the prior β grains can be seen to an extent with respect to orientation of α' phases. The HIP treatment as expected results in the formation of a lamellar ($\alpha+\beta$) microstructure. The lighter region is α phase and darker region present at the grain boundaries of α is the β phase. The microstructure does not change after the chemical etching and sandblasting process. As the β transus temperature is not reached during the HIP process, the columnar grain morphology is retained. The β phase fraction after post-processing is calculated similar to the internal porosity and the results are shown in Table 4.5.

Table 4.5 β phase fraction in weight percent, calculated by optimal method.

Sample type	β phase (wt. %)
As-processed	0
HIP	10.2 ± 2.4
HIP+CE	11.5 ± 4.6
HIP+SB	10.0 ± 1.2

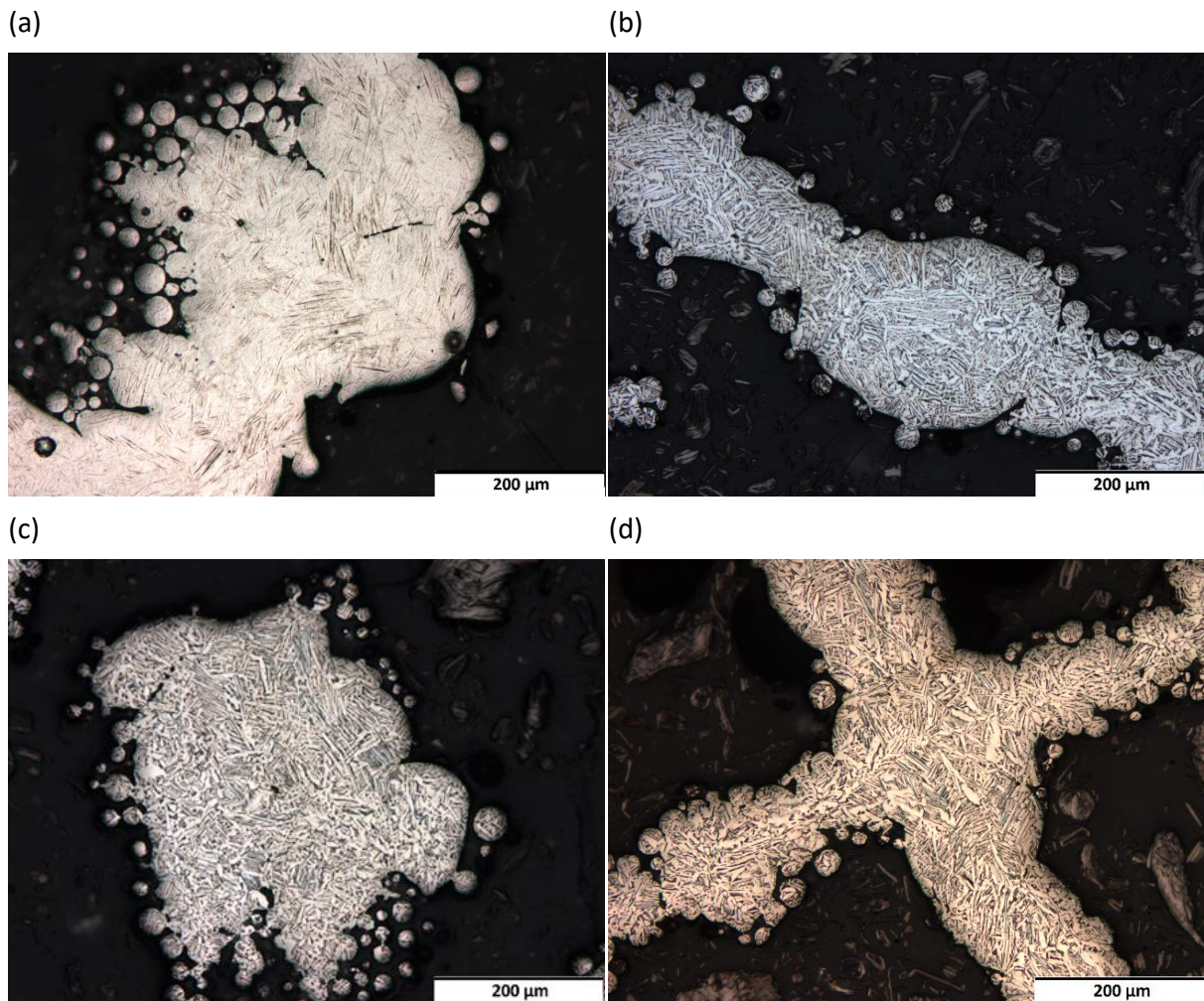


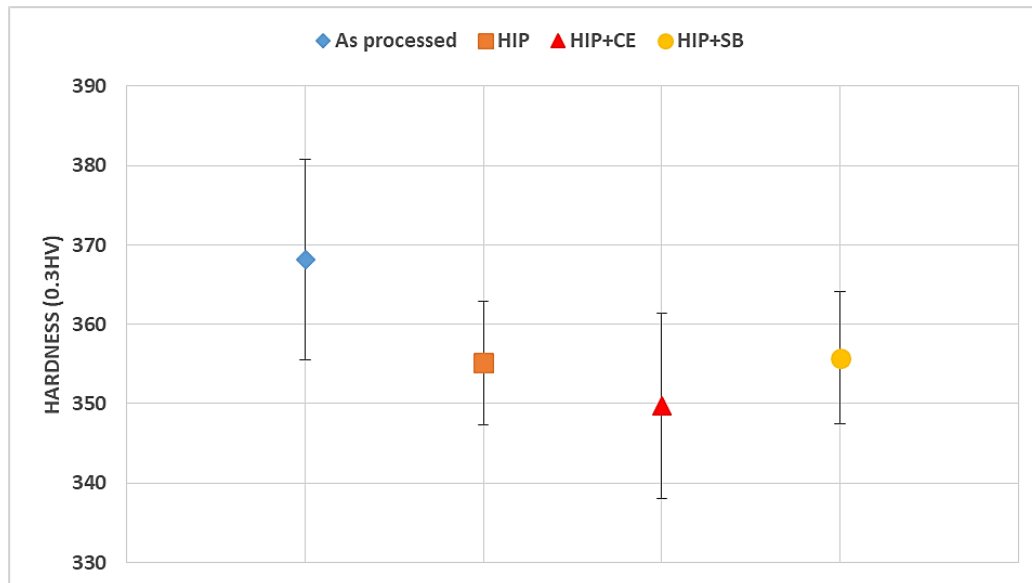
Figure 4.6 Optical Microscopy images for (a) as-processed (b) HIP (c) HIP+CE and (d) HIP+SB samples.

From the microstructure image for the as-processed condition, the various defects can be seen. The spherical pores seen in Figure 4.6 (a) represent the gas entrapped porosity and the irregularly shaped pores represent the lack of fusion porosity present between two subsequent layers or beads. As for the HIP condition, the simultaneous application of pressure and temperature reduces the internal process induced porosity, thus densifying the struts and forming a lamellar ($\alpha+\beta$) microstructure.

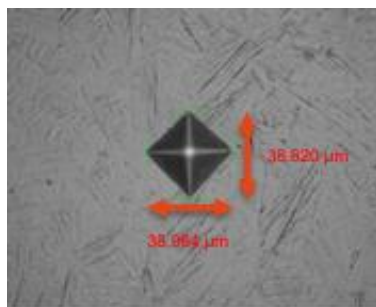
4.2.2 Hardness

A plot of the hardness profile with the indent size and shape for each of the sample is shown in Figure 4.7. From Figure 4.7 (a), it can be observed that the HIP process results in a small decrease in the hardness value by 3.5 % as compared to the as-processed samples due to the formation of an equilibrium ($\alpha+\beta$) microstructure. As for the surface modification techniques used, there is no effect on the hardness of the samples when compared to the HIP sample as the microstructure is not influenced.

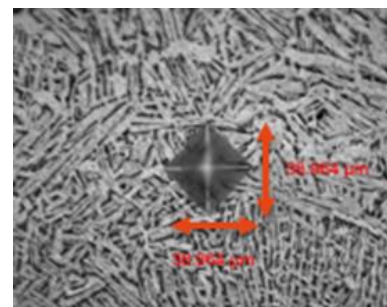
(a)



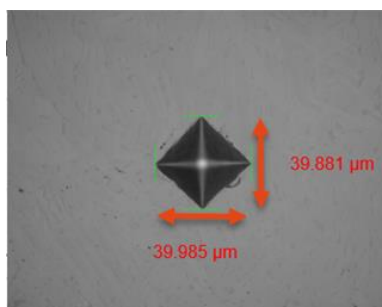
(b)



(c)



(d)



(e)

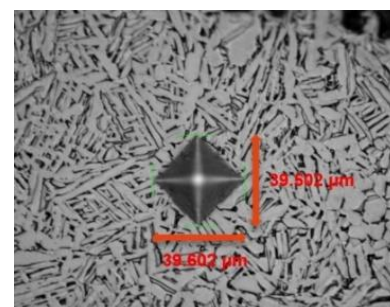


Figure 4.7 (a) Plot for the average hardness and indent shape and size for (b) As-processed (c) HIP (d) HIP+CE and (e) HIP+SB.

4.3 XRD

The diffraction pattern for the as-processed and post-processed samples are shown in Figure 4.8. A clear observation can be made in terms of an increase in the intensity of the peaks and a decrease in the peak width after HIP. Also, the presence of β can be observed due to the presence

of new peaks in the diffraction pattern. This can be attributed to the formation of equilibrium microstructure consisting of α and β phases from the as-processed α' microstructure. As for the HIP+SB sample, peak broadening is observed.

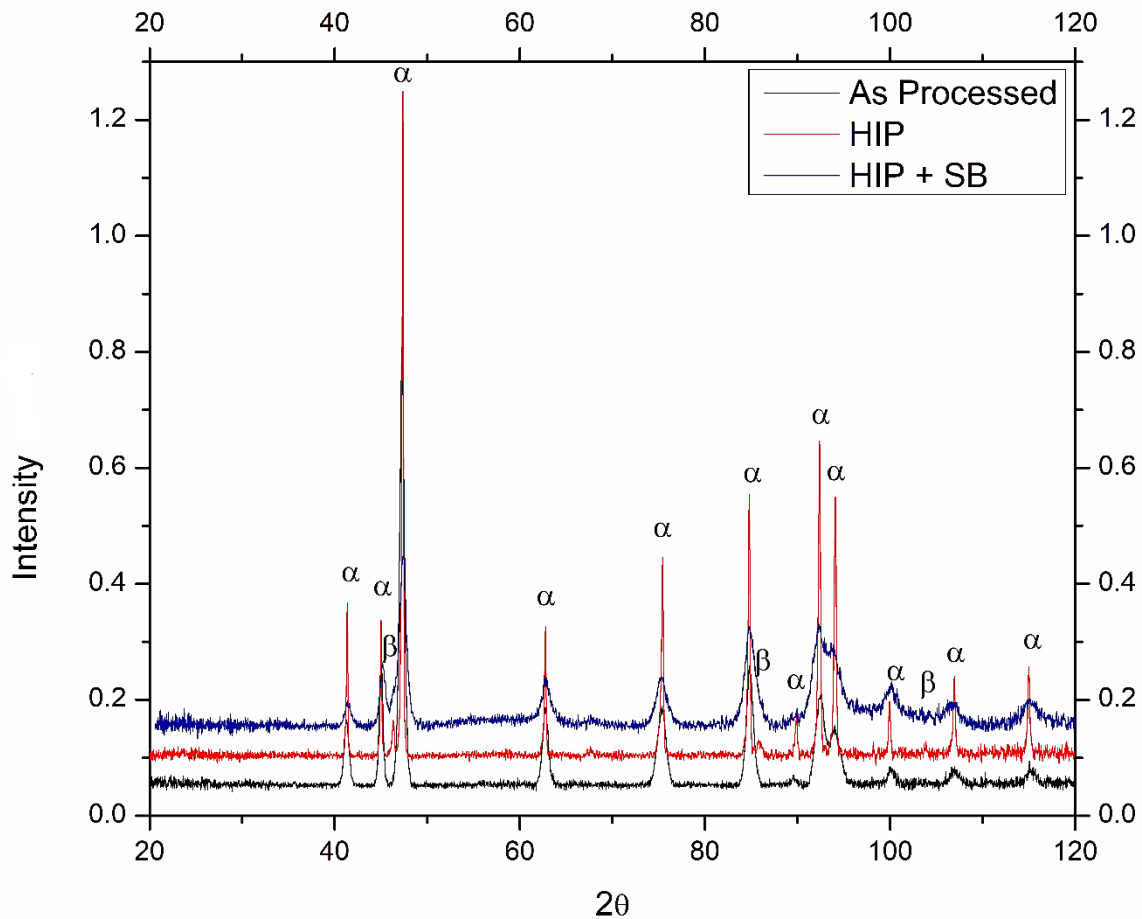


Figure 4.8 XRD pattern for the as-processed and HIP samples.

XRD was additionally used to confirm the presence of stresses caused by the sandblasting treatment on the strut surface. A clear increase in residual stresses was observed after sandblasting of the samples relative to that of HIP samples. This was in accordance with the increase in peak width accompanied by a peak shift and decrease in crystallite size by almost 10 times as shown in Table 4.6. The residual stress measurements were carried out along the building direction and perpendicular to the building direction before and after sandblasting of the same representative HIP sample. The results for residual stresses are shown in Table 4.6 with the standard deviation values.

Table 4.6 Stresses induced after sandblasting on HIP samples based on $\sin^2 \psi$ method.

Sample Type	Peak width (FWHM, $^{\circ}2\theta$)	Crystallite size (nm)	Residual stress along the building direction (MPa)	Residual stress perpendicular to the building direction (MPa)
HIP (Before SB)	0.1359	108 \pm 32	20 \pm 13	7.3 \pm 0.4
HIP (After SB)	1.3892	14 \pm 2	-245.3 \pm 82.9	-132.2 \pm 73.6

From Table 4.6, it can be seen that though there exists a large standard deviation in the values, sandblasting results in the formation of compressive stresses on the strut surface. This observation can be made for both the building direction and perpendicular to the building direction based on the $\sin^2 \psi$ method used in the calculation of residual stresses using the residual strain in the struts formed by the impact of the abrasives. An area of approximately 5*5 mm was measured and based on the optical images should have included more than a thousand grains for the stress estimation.

4.4 Static Mechanical Testing

The results of compression tests are shown in Table 4.7. From the table, it is observed that the HIP treatment results in an increase in ductility of the material as seen from the increase in both plateau and offset compressive strength. On the other hand, chemical etching followed by HIP results in a decrease in strength as compared to both HIP and as-processed sample. This is a result of removal of material by the etching process leading to a decrease in both relative density and strut thickness. This weakens the structure of the HIP+CE samples and hence, a reduction in the strength of the samples.

Table 4.7 Compressive mechanical properties for as-processed and post-processed samples.

Sample Type	σ_{\max} (MPa)	σ_p (MPa)	$\sigma_{0.05}$ (MPa)	Elastic Gradient ($E_{\sigma 20-70}$, GPa)	Energy Absorption (MJm^{-3})
As-processed	59.04 \pm 0.96	46.02 \pm 0.62	46.00 \pm 0.73	1.83 \pm 0.11	21.54 \pm 0.42
HIP	60.95 \pm 5.85	65.51 \pm 3.22	55.17 \pm 4.48	2.12 \pm 0.34	32.89 \pm 1.85
HIP + CE	51.19 \pm 5.50	54.36 \pm 2.15	44.17 \pm 4.37	1.78 \pm 0.23	26.44 \pm 1.11
HIP+SB	54.14 \pm 3.88	61.10 \pm 3.92	49.50 \pm 3.28	1.90 \pm 0.33	30.45 \pm 1.97

Figure 4.9 shows the images of the compression tested samples. From the images, it can be seen that the compression results in a gradual densification of the samples with the increase in strain and finally behaves like a completely solid sample. The images for the as-processed condition showed either complete or partial disintegration of the sample as shown in Figure 4.9 (b). The failure of the samples in all the cases takes place as successive collapsing of layers due to weakening of the struts with the application of load. In the case of as-processed samples the

failure appears to be brittle in nature with a sudden and comparatively larger decrease in stress for the first layer failure as compared to a more dampened phenomenon observed in the case of HIP and HIP+SB and to an extent for HIP + CE. The failure of the struts takes place close to the compression plates, generally at the bottom along the building direction of the specimen. The σ - ϵ plots for all the samples have been plotted individually on Figure 4.10 with their mean and standard deviation up to a strain of 60 % or 0.6.

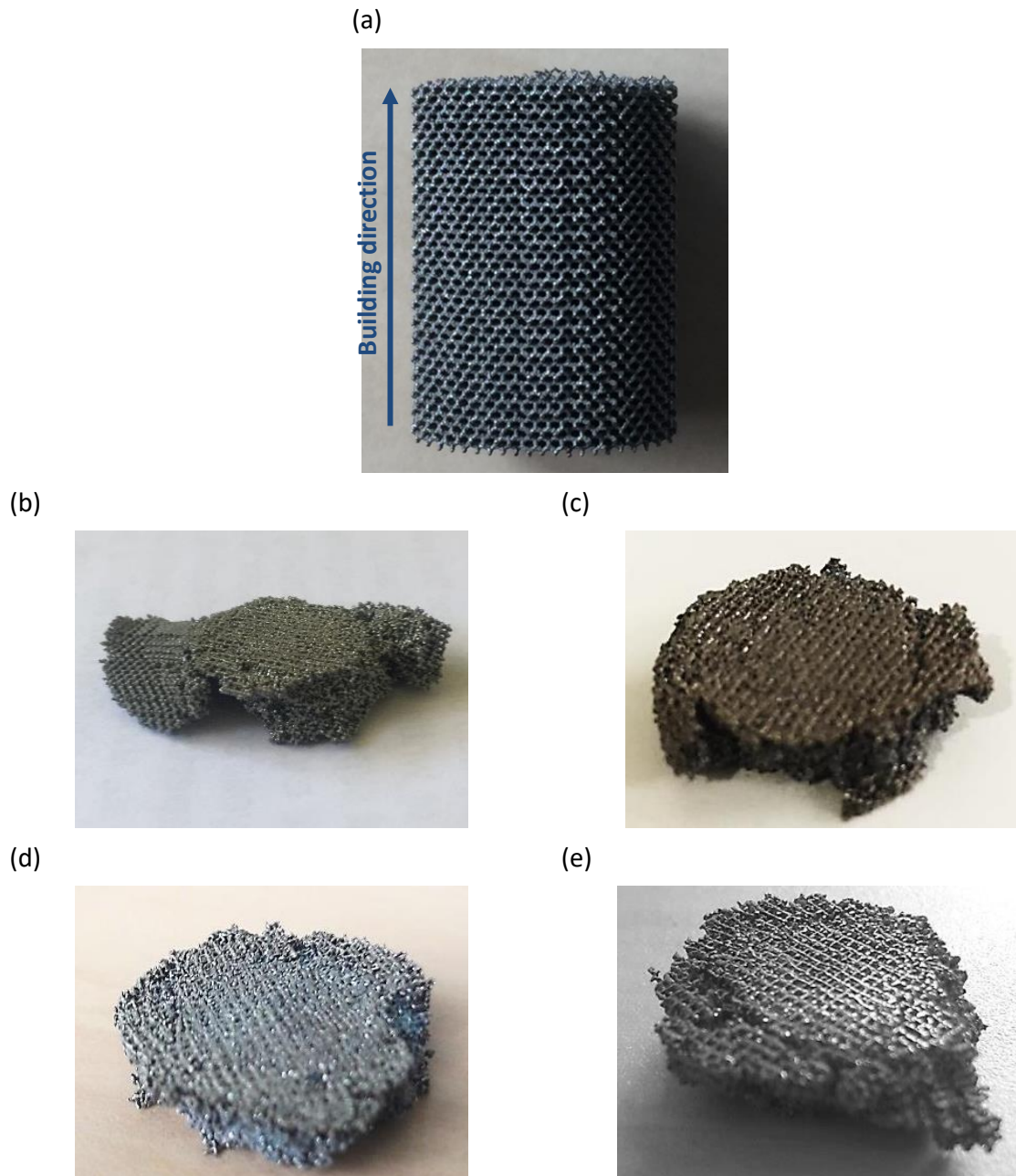


Figure 4.9 Compression specimen (a) before testing and after testing for (b) as-processed (b) HIP (c) HIP+CE and (d) HIP+SB sample.

From Figure 4.10, it can be observed that the HIP, HIP+CE and HIP+SB samples show a gradual densification process with an increase in stress as strain reaches 0.6 when compared to the

declining trend seen in the as-processed samples. For the HIP+SB, a reduction in σ_{\max} value but approximately the same σ_{pl} value and a 10 % reduction in the compressive offset strength as compared to the HIP samples is seen. This indicates that sandblasting technique results in the minimum loss of strength after the surface modification of HIP samples. As for the HIP+CE sample, it is the weakest in terms of strength among the samples tested.

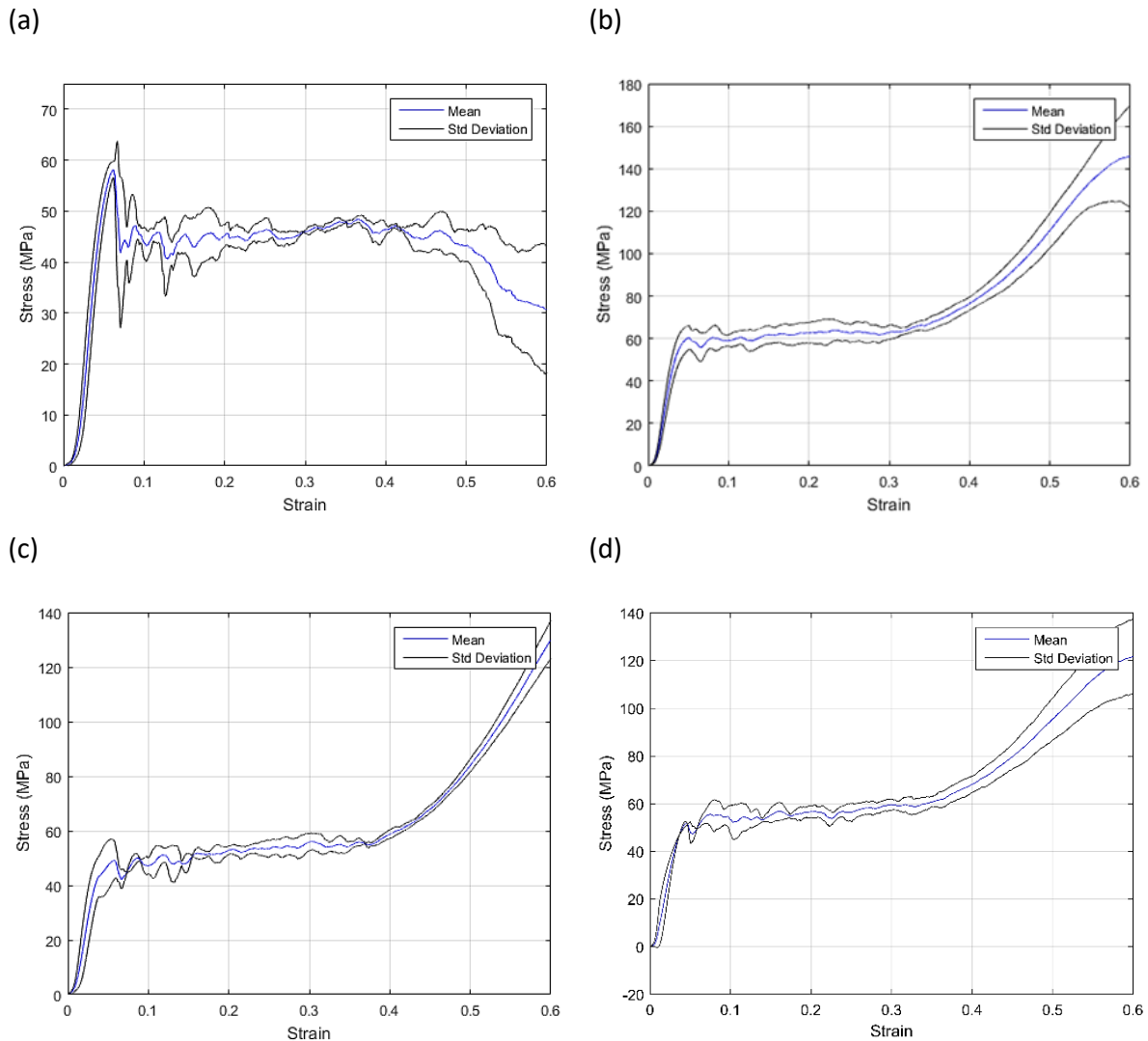


Figure 4.10 σ - ϵ plots after compression for (a) as-processed (b) HIP (c) HIP+CE and (d) HIP+SB.

4.5 Fatigue

The fatigue life for the as-processed, HIP, HIP+CE and HIP+SB conditions are plotted against the normalised stress values in Figure 4.12. The maximum stress applied during each test is normalised with their respective compressive offset stress for the as-processed, HIP, HIP+CE and HIP+SB to plot the S-N curve. A minimum of two samples were tested at each normalised stress value for the as-processed and post-processed condition. Additional samples were tested when the scatter was greater than 40 % for a given test criteria. Failure of specimen generally occurred

along an angled plane of 45° or -45°, either at one or two planes as shown in Figure 4.11. Table 4.8 shows the power law fitting terms used for plotting the curves.

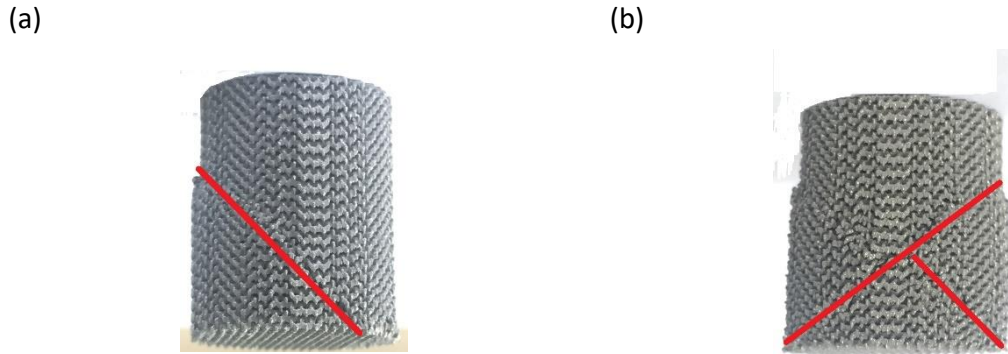


Figure 4.11 Typical sample failure after fatigue at (a) one or (b) two planes.

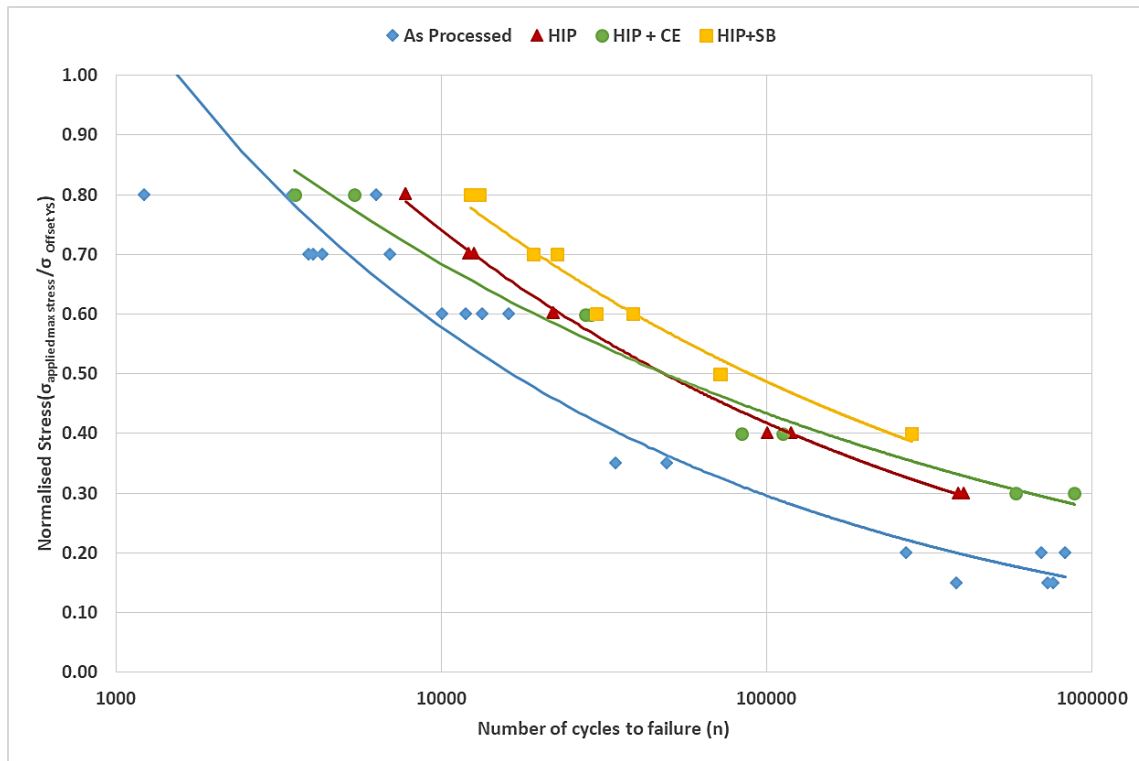


Figure 4.12 S-N plot for the as-processed and post-processed conditions after normalisation.

Table 4.8 Power law fit parameters ($y=ax^b$).

Sample type	a	b	R ²
As-processed	8.4601	-0.291	0.9467
HIP	7.3620	-0.249	0.9978
HIP+CE	4.2533	-0.198	0.9683
HIP+SB	6.4086	-0.224	0.9767

From Figure 4.12, it can be observed that the post-processing results in an improvement in the fatigue life based on the S-N curve. For the as-processed condition, a large scatter can be observed for all the fatigue testing conditions. The coefficient of determination, R^2 value also gives a clear indication of the scatter observed in the plot. A reduction in scatter for the post-processed samples is seen which is confirmed by the R^2 value being closer to 1. The post-processed samples also show an improvement in fatigue life over the as-processed samples as shown in Figure 4.12.

A comparison between the post-processed samples show that the HIP+SB samples have the best resistance to fatigue when compared to HIP and HIP+CE. As for the HIP and HIP+CE samples, observations can be made in terms of better fatigue resistance for HIP samples at higher normalised stress values (> 0.5). But as the normalised stress values goes below 0.5, a change in trend is seen. The HIP+CE samples show an improved fatigue life behaviour when compared to the HIP samples (Normalised stress < 0.5). A million cycles were achieved in all the post-processed conditions following which the test stopped based on the applied constraints. The points are not shown in the above plots as the samples did not fail at a million cycles. For the HIP and HIP+CE samples a fatigue life of a million cycle without failure was achieved at 0.2 and for the HIP+SB samples at 0.3 normalised stress value. Based on the fitted power law equation, a fatigue life of a million cycles can be reached at a normalised stress of 0.24 for HIP, 0.28 for HIP+CE and 0.3 for HIP+SB samples.

4.6 As-processed (Vector vs STL based approach)

In this section, the two different SLM approaches are compared for the as-processed samples. An important consideration to be taken into account is the difference in weight, hence, the relative density and the unit cell size of the samples. Also, a limited number of samples of STL approach were available for testing. Table 4.9 shows the morphological characterisation of the samples in terms of relative density for the two techniques.

Table 4.9 Relative density and unit cell size of the samples.

Sample Type	Relative Density (ρ_{rel})	Unit cell size (mm)
Vector based	31.89 ± 0.58	1
STL approach	37.30 ± 0.41	1.5

The STL approach based samples were acquired from Amber Implants B.V. and hence, the processing parameter information cannot be disclosed. The as-processed samples as expected have the same microstructure consisting of martensite, α' as shown in Figure 4.13. From the micrographs, an observation can be made in terms of the fine needle of α' clearly showing the prior β grain boundaries for the STL samples.

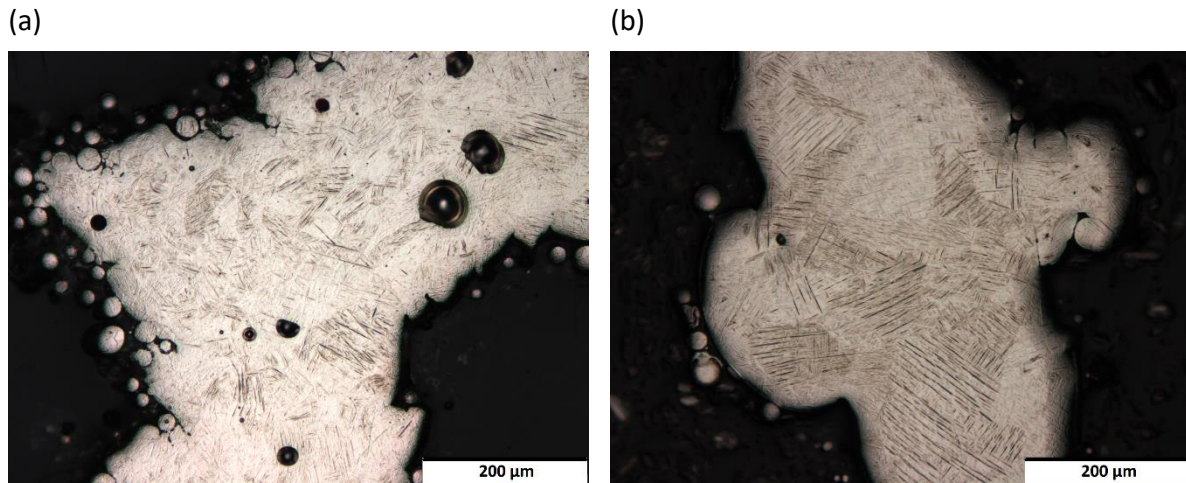


Figure 4.13 Optical micrographs for (a) Vector based and (b) STL based as-processed samples.

The results for the Vickers hardness test using 0.3 kgf have been shown in Table 4.10. STL based samples showed an increase of 7 % in the hardness value as compared to the vector based samples. This is seen even though there is no change in the microstructure between the two samples.

Table 4.10 Vickers hardness test results.

Sample type	Hardness (HV _{0.3})
Vector based	368.13 ± 12.66
STL based	395.55 ± 10.81

Figure 4.14 shows the SEM images from the top surface for a representative sample. The STL sample shows a reduction in the amount of loosely stuck and partially melted powder particles on the strut surface as compared to the vector approach samples.

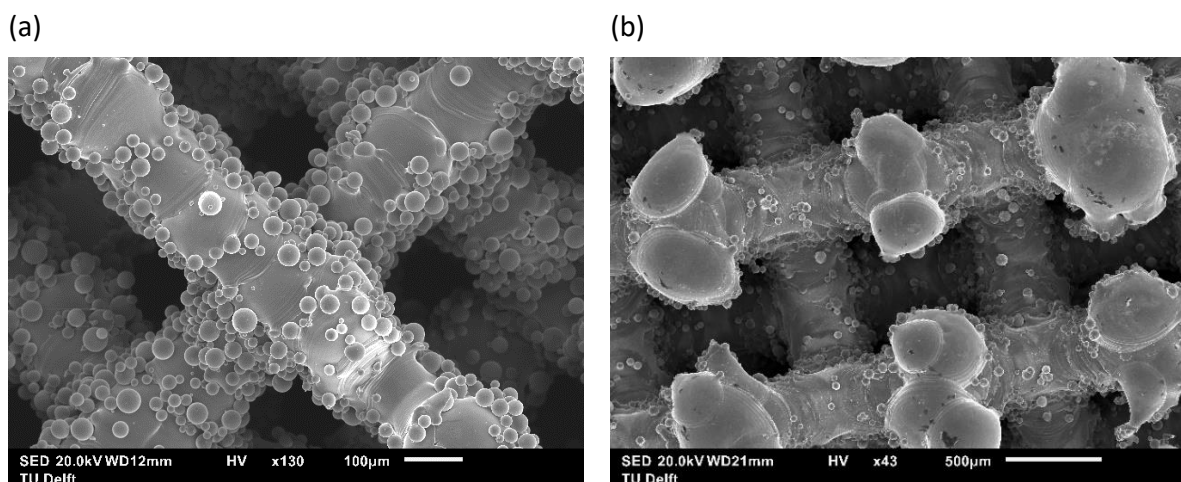


Figure 4.14 SEM images for (a) Vector based and (b) STL based sample.

Following the morphological characterisation, static mechanical testing was carried out using the same parameters as discussed in Section 3.6. The results for the compression test are shown in Table 4.11. An increase in compression strength can be seen for the STL samples. This can be attributed to the higher relative density and decreased defects. The increase was expected but was almost double.

Table 4.11 Compressive mechanical properties.

Sample Type	σ_{\max} (MPa)	σ_p (MPa)	σ_{Oys} (MPa)	Elastic Gradient ($E_{\sigma_{20-70}}$, GPa)	Energy Absorption (MJm^{-3})
Vector based	59.04 ± 0.96	46.02 ± 0.62	46.00 ± 0.73	1.83 ± 0.11	21.54 ± 0.42
STL based	121.74 ± 2.23	78.83 ± 4.34	79.75 ± 2.47	3.51 ± 0.08	41.00 ± 1.85

Figure 4.15 shows the σ - ϵ plot for the two samples. Due to the limited number of STL samples, only two were tested for and used in the static compression test analysis. From the plot, it can be observed that the STL based samples conform to the behaviour mentioned in literature [4, 23]. There is a sudden drop in stress level with the failure of each subsequent layer. This observation is not exactly clear in the vector based samples. Vector based samples after the first failure show a continuous decline in the stress levels. The densification behaviour of the porous sample is seen with an increase in stress after 0.5 strain for the STL samples whereas a drop in stress level is observed in vector based samples.

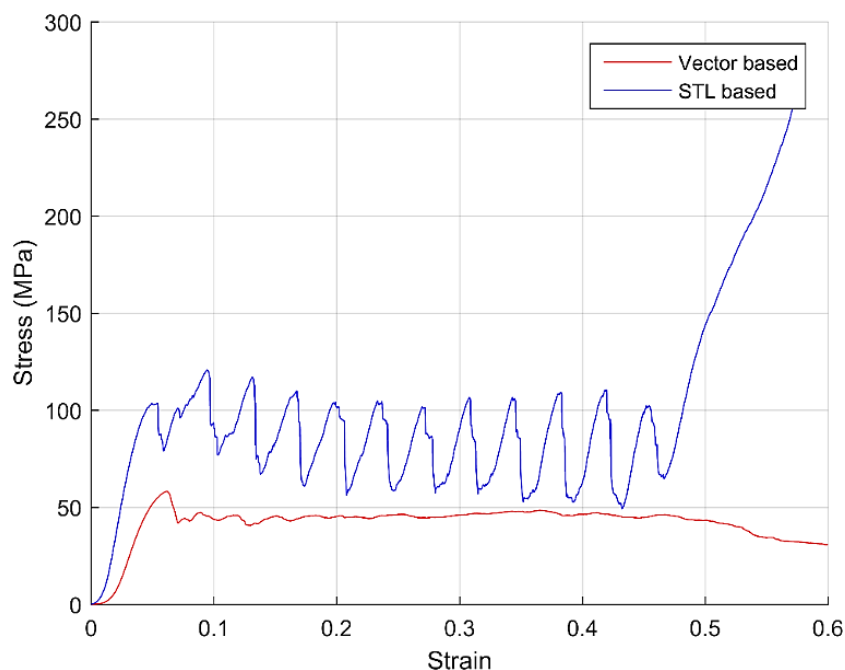


Figure 4.15 Mean σ - ϵ plot for vector based and STL based samples.

Based on the compression test results, fatigue tests were carried out. The S-N curves are plotted by testing the samples using the same parameters as mentioned in Section 3.7. As mentioned

earlier, the limited number of samples meant that fewer stress values were tested for the STL samples. The results are plotted in Figure 4.16 and the power law fitting parameters used are shown in Table 4.12.

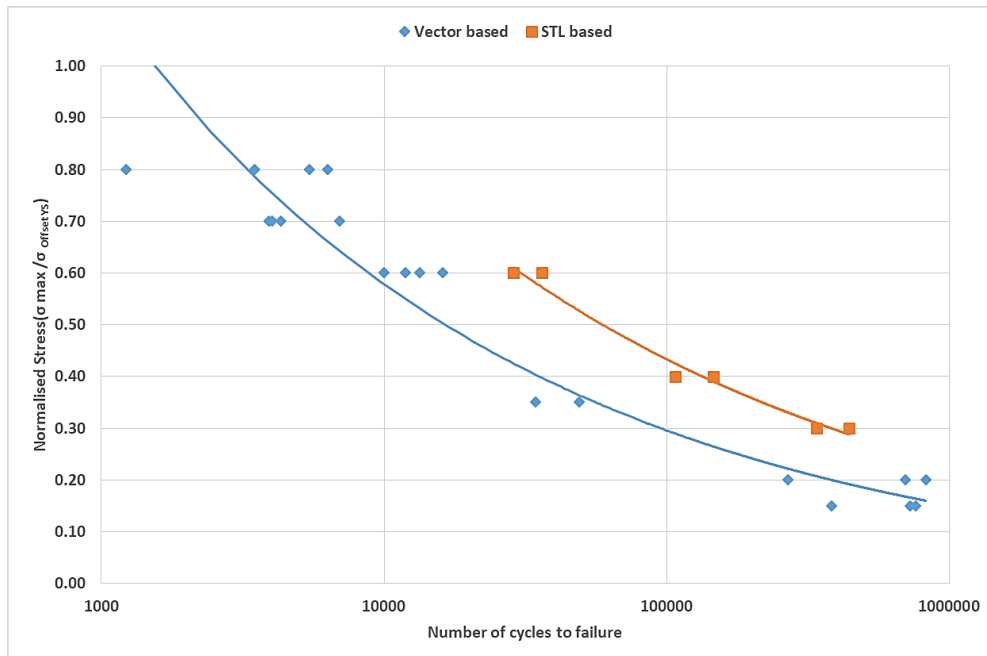


Figure 4.16 S-N plot for the as-processed vector based and STL based samples after stress normalisation.

Table 4.12 Power law fitting parameters ($y=ax^b$).

Sample type	a	b	R ²
Vector based	8.4601	-0.291	0.9467
STL based	10.23	-0.275	0.9805

Based on the plot in Figure 4.16, an improvement in fatigue life with respect to the normalised stress can be observed by the shifting of the power law curve to higher values for the STL samples. Also, a reduction in scatter in the data to less than 10% indicates the repeatability of the property for a given load which is absent in the case of vector based samples due to the high scatter. This reduction in the scatter is confirmed by the high R² value (closer to 1) for the STL based sample. Another important observation which is not shown in the plot is with respect to 0.2 normalised stress for STL samples not failing even after a million cycles. This indicates a substantial improvement in fatigue behaviour for the STL based sample as compared to the vector based. The vector based sample failed to reach a million cycle even for a normalised stress value of 0.15. Based on the power law equation a fatigue life of a million cycle can be reached at a normalised stress of 0.15 for vector based and 0.23 for STL based samples. But due to the large scatter in the vector based samples, this value cannot be held accountable.

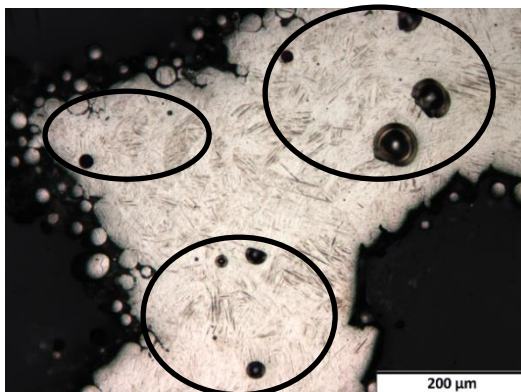
Chapter 5 Discussion

5.1 Vector approach based samples

5.1.1 Morphological characterisation

The results of the relative density of the as-processed and post-processed samples are as expected. With the post-processing treatment, in particular, HIP there was no influence on the relative density of the samples. As for the surface modification treatment, as mentioned earlier and shown in the Section 4.1.2 and 4.1.3, removal of loosely stuck and partially melted powder particle from the strut surface causes a decrease in weight and hence a reduction in the relative density of the sample. The material removal in the case of sandblasted samples was less compared to chemical etching and hence the large difference in the relative density between the two. The as-processed samples based on Figure 4.1 and Table 4.2, show a high percentage of process induced porosity and defects. This will be detrimental in the mechanical properties of the structure. These defects can act as sites for crack nucleation and propagation. Thus reducing the strength of the structure. Figure 5.1 (a) shows the process induced gas pores and lack of fusion pores encircled in black and (b) a SEM image from a representative sample of a strut which shows lack of fusion between two beads for the as-processed samples. During loading, these sites can inherently weaken and result in a premature failure of the entire structure [4, 12, 15, 30]. These defects are a result of non-optimised process parameters. The positive influence of HIP can be seen with the reduction in internal porosity to 0.1-0.2 % from 1.2-1.6 % by the closing of internal voids and pores. This was visible even in the optical images taken during the course of the analysis.

(a)



(b)

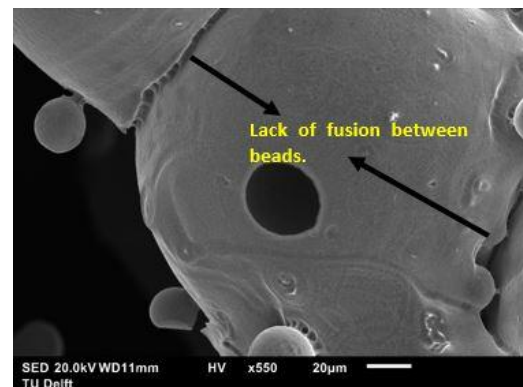


Figure 5.1 (a) Process induced internal defects and porosity and (b) Lack of fusion between beads.

5.1.2 Microstructure and hardness

The microstructure and hardness correspond with the influence of post-processing on the samples. The as-processed sample microstructure as shown in Figure 4.6 (a), consists of acicular or fine needle like martensite, α' which is brittle and has a high hardness value. The high hardness value is due to the presence of the martensite (HCP structure), which is a closely packed and non-equilibrium brittle phase characteristic of SLM. The HIP treatment in addition to closing of the internal process induced pores and stress relieving, results in the formation of a lamellar ($\alpha+\beta$) microstructure as observed in Figure 4.6 (b). Also, due to the temperature being close to the β transus temperature, a small amount of equiaxed α grains are observed. According to I. Yadroitsev *et al.* (2014) [41], when heat treated below β transus temperature at 800 °C, decomposition of α' followed by the nucleation of fine α precipitates at martensite grain boundaries and simultaneously enrichment of the surroundings by β stabilisers resulting in the formation of equilibrium ($\alpha+\beta$) phase mixture takes place. A similar phenomenon can be seen in HIP microstructure, with the development of a columnar equilibrium microstructure and small amounts of equiaxed α phase. The elongated grain structure emerges due to epitaxial growth and the direction is related to the process parameters and building direction [42, 43]. The prior β grains cannot be clearly distinguished after HIP but EBSD analysis can be used to determine the orientation of the α phases and hence the prior β grains formed during the processing of the sample. The prior β can be distinguished to an extent in the as-processed microstructure. The percentage of β is in agreement with literature [12] at around 10 % for the post-processed samples. This explains the decrease in the hardness value to a mean value of around 355 HV_{0.3} from 368 HV_{0.3} for all the post-processed conditions. The surface modification technique does not influence the microstructure and hence does not correspond to any change in hardness as seen in the results.

5.1.3 Surface modification treatments

Surface modification treatments used in this research are the chemical etching and sandblasting technique. A lot of literature with respect to the use of chemical etching and its influence in improving fatigue behaviour is documented. But no literature was found on the use of sandblasting technique for surface modification of porous structure. This could be due to the difficulties involved in removing the abrasives from the porous structure or due to the size of the abrasive particles in comparison with the strut size. The influence of the effect of the two techniques have been shown in the results section in terms of morphology and ability to remove material. B. van Hooreweder *et al.* (2017) [4] showed the top surface of the sample as a representative for the influence of chemical etching on the entire sample. However, top surface images do not represent the entire sample and cannot be used to discuss uniformity of the etching process. Hence, it is important that images from the core of the sample in combination with top surface be used to confirm the homogeneity of the process. Attempts were made to homogenise the chemical etching process but as observed based on Figure 4.3, the chemical etching treatments does not fully reach the core of the samples. Surface modification treatments require further optimisation in order to ensure a more homogenised treatment throughout the sample. This is needed to ensure that not only the removal of material from the surface but also the core of the structure takes place. The results from C. de Formanoir *et al.* (2016) [33] show a completely optimised chemical etching treatment of titanium lattice structures by using relative densities as

low as 7.3 % and a much more open structure with a strut diameter of 1 mm. The etching time used is also significantly higher at 30 minutes with four repetitions using fresh etchant with a similar etchant solution consisting of 3 % HF and 13 % HNO₃ [33]. The lack of homogenisation by chemical etching in this research can be a result of the unit cell size of the samples used being low. In addition to this, the etching process results in the formation of air bubbles which can prevent any reaction from occurring within these bubbles. Another potential reason could be that the samples did not have an open cell network preventing the acid from reaching the interiors of the sample. The viscosity of the acid also can be another reason to explain the inhomogeneity. All these recommendations should be taken into account when selecting best suited etchant.

Based on the results, it can be concluded that the influence of chemical etching in the material removal process is greater than that of sandblasting and also has higher efficiency in terms of reaching greater depths in the sample. This can be attributed to the size of the abrasive particles during sandblasting being large, some almost equal to the strut diameter. Thereby decreasing the ability of the abrasive to remove material from the interior of the samples. Also, the residual contamination of the alumina particles must be taken into consideration as they tend to remain in the form of fragments on the strut surface during sandblasting as shown in Figure 5.2. Alumina contaminants reduce the corrosion resistance of titanium in physiological environment and hence it is important that the residual particles be minimised if not removed completely [35]. Figure 5.2 shows a schematic of the influence of the impact of irregularly shaped abrasive on the strut surface.

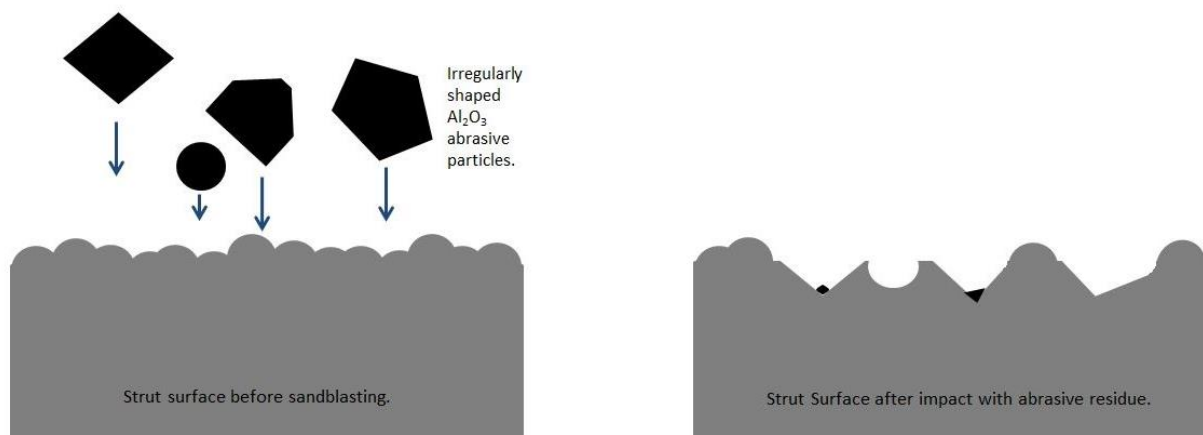


Figure 5.2 Schematic of sandblasting using Al₂O₃ abrasives.

Sandblasting was carried out using sharp edged abrasive particle as shown in Figure 5.3 (a) and (b). From the SEM images, it can be observed that the abrasive particles are irregularly shaped and have a varying size. The influence of the varying size of the abrasive particles is shown in Figure 5.3 (c). It can be seen that the abrasives in addition to removing loose and partially melted powder particles, impart a permanent plastic deformation on the strut surface. The shape and size of these deformation are varied and depend on the impacting particles. The irregular shape and size of the particles induce a roughness on the strut surface which can be an advantage for biomedical application. Based on the literature review, the imparted roughness can help in better osseointegration and bone on growth but can affect the mechanical properties by forming micro cracks on the surface.

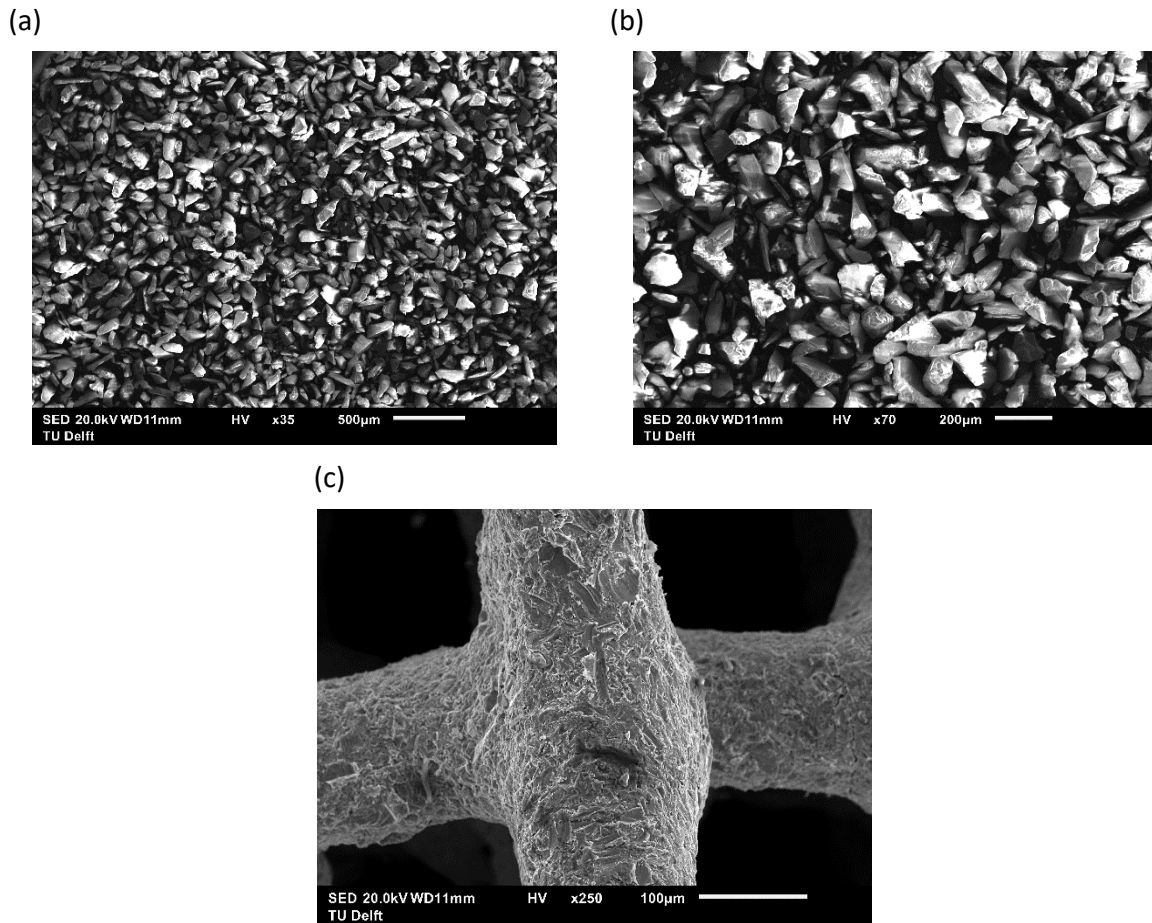


Figure 5.3 (a) and (b) Aluminium oxide abrasive particles and (c) HIP+SB sample strut surface.

The influence of sandblasting on the strut surface can be considered similar to that induced by shot peening on metal surface and welds. Shot peening is a cold working process used to induce compressive residual stresses on metal and composite surface to improve fatigue life. It is done by impacting the surface with round metallic, glass or ceramic particles [44]. Shot peening is advantageous in improving the fatigue life for Ti6AL4V alloy [34, 45, 46], but also can be counter-productive. Shot peening if applied on porous structures can result in the damage of the strut surface and induce early crack initiation reducing the fatigue life. A similar behaviour of the sandblasting particles is possible on the porous structure. Sandblasting, similar to shot peening, results in the formation of compressive stresses on the strut surface which prevents crack propagation. Thus improving the fatigue life in addition to reducing surface roughness. This correlation with shot peening is based on the fact that the abrasive particles used during sandblasting are of the same size as used for shot peening and impart compressive stresses on the strut surface. The only difference being the use of sharp edged abrasives during sandblasting as shown in Figure 5.3. Thus, sandblasting gives the dual advantage of surface roughness optimisation and compressive stress creation on the strut surface.

The formation of compressive stresses on the strut surface was observed in the XRD plots in Figure 4.8 by the broadening of the peaks, possibly accompanied by shifting for HIP+SB. This shift in the peak is not visible because of the large width and the shifting is generally correlated to residual stresses. The presence of compressive stresses was confirmed by the stress analysis carried out

on the samples before and after sandblasting using the $\sin^2 \psi$ method. It results in the formation of stresses due to impact by abrasive particles in both the building and the direction perpendicular to the building direction. Note that the value for the residual stresses shown in Table 4.6 are not absolute. They are relative to the HIP samples and are calculated using the elastic constants of pure titanium. There is a large scatter in the stress data as shown by the standard deviation. This can be attributed to the manual sandblasting of the samples. This can affect the angles at which the abrasive particles impact the surface. The residual stresses being different in the two measured directions can be due to the anisotropy in the property of the material because of the preferential texture in the microstructure. This needs to be confirmed by EBSD analysis of the samples. Another reason for the dissimilarity could be the manual sandblasting of the HIP+SB sample resulting in a non-homogenised treatment. Additionally, similar to chemical etching, sandblasting process failed to reach the core of the sample as shown by the Figure 4.5 and requires further optimisation

A solution for ensuring a homogenised surface modification treatment throughout the samples with the mentioned techniques would be to increase the unit cell size. An increase in unit cell size would help the flow of abrasive particle for sandblasting and easier flow of the acid for chemical etching into deeper channels of the open network of the samples. A reduction in the size of the abrasive for sandblasting can result in homogenisation. A combination of sandblasting followed by acid etching referred to as SLA technique should be experimented with. The acid etching step after sandblasting can assist in removing the contamination residue from the sandblasted abrasives.

5.1.4 XRD

XRD patterns in Figure 4.8 correspond to that of the non-equilibrium α' phase (HCP) for as-processed and α (HCP) and β phase (BCC) for the post-processed samples. The peaks for the HCP and BCC phase are seen in the case of all the post-processed samples with the maximum intensity peaks overlapping. The decrease in peak width after HIP and HIP+CE is due to an increase in crystallites sizes. This is attributed to the formation of α phase after HIP from α' phase which relates to a change in the lattice parameters. As for the HIP+SB samples, peak broadening is seen. This again is a result of change in crystallite size at the measured surface as shown in Table 4.6. This is caused by the compression of the crystallites by the impact of abrasive particles. In addition to the peak broadening, there is a possible shifting of the peaks confirmed by the formation of compressive residual stresses on the strut surface by the impact of Al_2O_3 abrasive particles. The peak shifting may not be visible due to large peak width after sandblasting. For the HIP+CE sample, the diffraction pattern was the same as the HIP sample and no shifting or broadening of the peaks was observed. The phase fraction based on the area under the peaks could not be determined accurately due to the curvature and porosity of the sample in addition to the curvature of struts. The results attained were lower than expected at 5 % for β phase fraction (wt. %). The curvature of the sample results in an unexpected increase in the peak intensity for higher 2θ angles. In addition to this, a lot of background noise is seen in the data making it difficult to identify peaks with low intensity.

5.1.5 Static mechanical testing

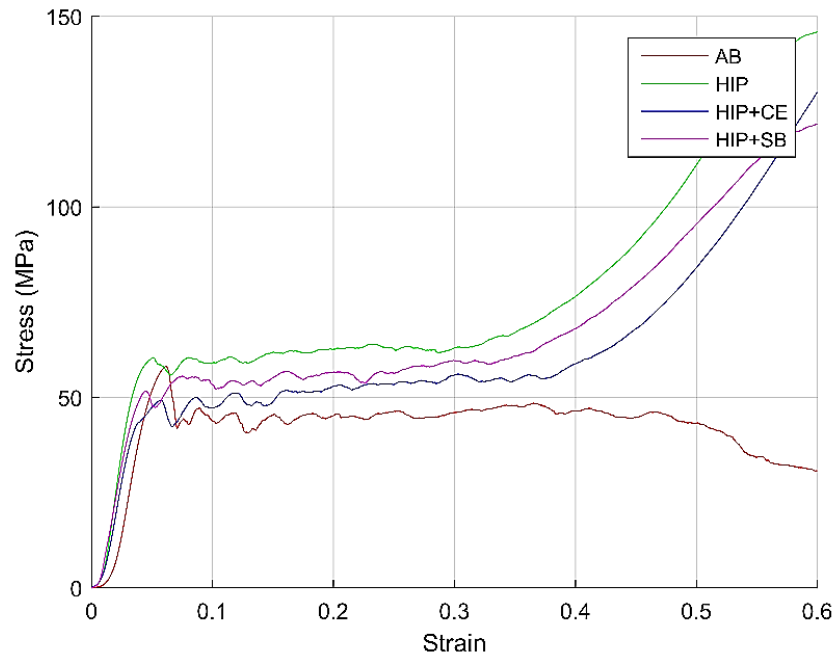


Figure 5.4 Mean σ - ϵ plots for the as-processed and post-processed samples.

The results of static mechanical testing are discussed in the following sub-section. Figure 5.4 shows σ - ϵ curve for the as-processed and post-processed samples using the mean data from compression of the three samples. The as-processed (AB) plot shows a sudden drop in stress with respect to the failure of the first layer and a continuous decline in the stress for increasing strain. The decline in stress is contrary to the expected rise by the densification of the samples during compression [4, 23, 25]. It is a result of defects in the as-processed samples. The lack of fusion between the beads forming the struts and process induced internal porosity as shown in Figure 5.1, results in the continuous weakening of the structure. During the testing, the samples had parts chipping off and the structure disintegrating, indicating the incomplete fusion between successive layers of the as-processed samples. For the post-processed samples, a more dampened stress phenomenon is seen clearly in the plots for the HIP, HIP+CE and HIP+SB compared to the as-processed sample. Thus, indicating a more ductile behaviour which can be correlated to the presence of the β phase and an equilibrium (α + β) microstructure [30]. In the case of HIP samples, a decrease in strength was expected with higher ductility. But to the contrary, due to the densification of the struts in the samples by the reduction of the process induced porosity to around 0.15 % by the application of pressure, an increase in the strength is observed. This shows the importance of the influence of defects in the SLM process and the need to minimise them by process parameter optimisation in the initial stages. If optimised, the HIP process can show a larger improvement in mechanical properties of the samples. The HIP+CE plot as shown in Figure 5.4, shows the first failure at a lower stress level when compared to the HIP and HIP+SB sample indicating a reduction in strength. This is due to the decrease in the relative density and strut thickness by chemical etching. By the compression test results, a proportionality relation between the strength and relative density can be established where an increase in relative density corresponds to an increase in the strength of the structure. The HIP+SB sample has a behaviour

similar to HIP but with decreased strength and the same ductility as shown by the plateau stress (σ_{pl}) value.

5.1.6 Fatigue

Based on the data obtained from the compression tests, the loading conditions for compression-compression fatigue were decided and the tests were carried out. From Figure 4.12, a clear improvement in fatigue life with the shifting of the curves to top right for the post-processed samples is observed. The large scatter in the as-processed condition is due to the presence of defects in the samples. The position and size of the defects have a significant role in determining the fatigue life of the structure as explained by S. Beretta *et al.* (2016) [47]. The sub-surface defects lower the fatigue life more than the defects present in deeper positions [47]. Thus, HIP leads to improved fatigue life and reduced scatter. This is due to the reduction in process induced porosity by pressure and the change in microstructure to an equilibrium, lamellar ($\alpha+\beta$) by HIP. As mentioned in the results, the surface modification treatment improves the fatigue life of the HIP samples. HIP+SB showing the most prominent improvement among them. This is a result of the compressive stresses on the strut surface resisting fatigue crack growth. The influence of surface roughness is noticeable in the case high cycle fatigue life of a material [48]. This could be a possible explanation for better fatigue life of HIP+CE samples at lower normalised stress values as it smoothens the strut surface and reduces the surface irregularities. As for the failure during fatigue at angles of 45° or -45° and in one or two planes, there is no clear relation between the applied loads or the sample type as previously mentioned in J. De Krijger (2016) [49].

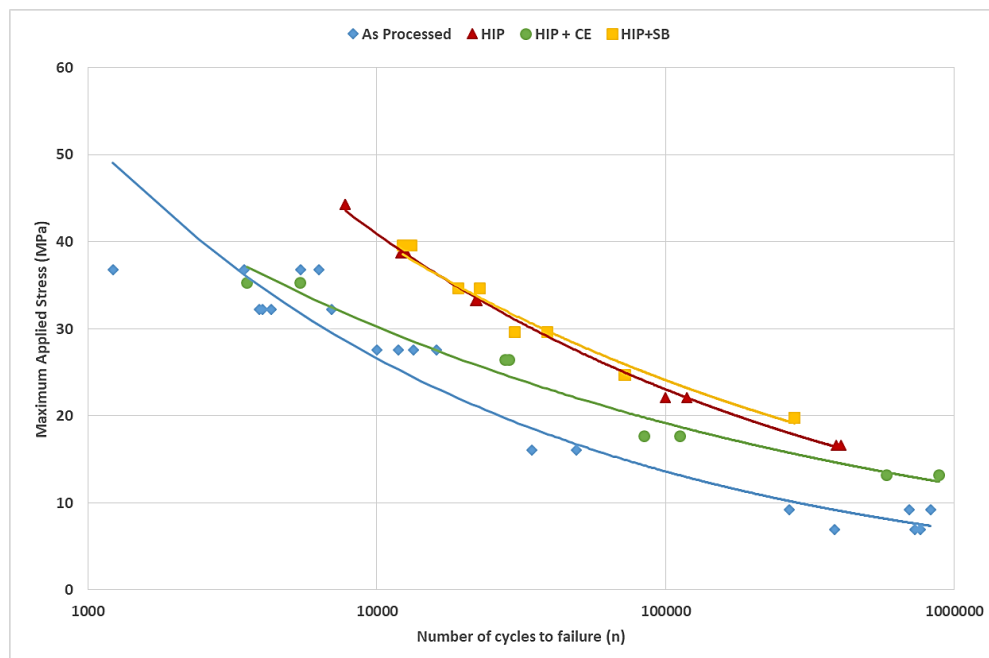


Figure 5.5 S-N curve using maximum applied stress during fatigue for as-processed and post-processed samples.

Data representation plays a key role in determining the properties of a material for a given application. This is shown by comparing the S-N curves plotted in Figure 4.12 and Figure 5.5. The plot in Figure 4.12 based on normalisation of the maximum applied stresses shows the behaviour

of the HIP+CE samples being improved compared to the HIP samples at normalised stress of lesser than 0.5. The normalising of the data was done to represent each sample type with respect to their compressive offset yield properties. Following which a comparison was done. But based on the Figure 5.5, it can be observed that the HIP samples show a better fatigue life when compared to the HIP+CE samples for all load conditions. Thus, for application related to high load requirements, it is important to plot the S-N curve using the applied stress and not by normalisation. But in the case of biomedical application for implants, where the applied loads during usage are not high, normalisation is used to plot the S-N curve.

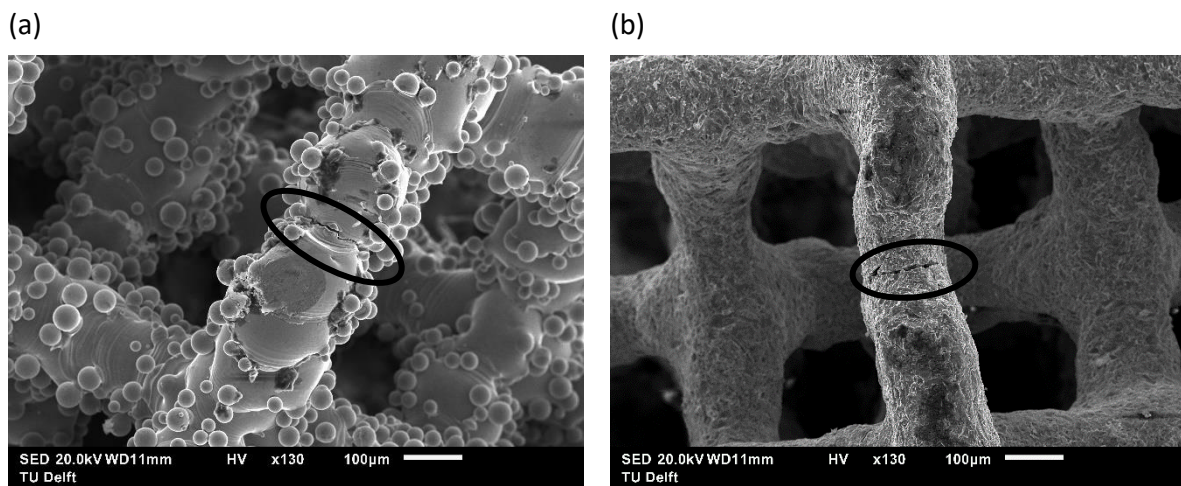


Figure 5.6 Fatigue cracks for (a) as-processed and (b) HIP+SB sample.

Figure 5.6 show SEM images of fatigue cracks for the as-processed and HIP+SB from representative samples. From the as-processed sample, it can be observed that the cracks initiate and grow at the region linking the beads. These regions are the weakest links that exist between beads forming the struts and are highly susceptible to fatigue cracks as shown in the Figure 5.6(a). The fatigue crack formation for the HIP and HIP+CE samples were identical to the as-processed samples. As for the HIP+SB sample, a clear differentiation on the site for failure cannot be made. But based on careful inspection, the cracks tend to initiate and grow at the thinnest region of the strut similar to the as-processed samples. This shows the region for failure being the links between the beads for the vector based approach samples.

With respect to the application of the SLM vector based approach for the biomedical implants, the as-processed samples have high strength but low ductility. Also, the presence of the process induced porosity affects the fatigue life. It reduces the fatigue life and increases the scatter in the data. Thus, post-processing is a necessary step for the utilisation of the process in manufacturing implants. HIP is an important post-processing technique to maintain the strength and at the same time provide ductility to the structure. The surface modification techniques as seen, show a positive influence on fatigue life. Chemical etching after HIP increases the fatigue life at lower normalised stress values. The lower loads are what a human body would be subjected to. Hence, the high fatigue life at lower normalised stress values indicate that the implants do not require regular replacements and have prolonged life. The sandblasting technique shows the highest improvement in fatigue life indicating that the sandblasting technique is the best suited surface modification treatment after HIP. In addition, the roughness imparted by sandblasting can be an advantage. It aids better osseointegration and bone on growth. The elastic gradient for all the

cases though are lesser than those for bones, an increase in the relative density can result in an increase in the elastic gradient. Thus, they can be made to match the properties of the bone they are intended to replace and in the process avoiding the stress shielding effect. The samples after post-processing were able to withstand a million cycles at lower normalised stress values. Therefore, showing their potential to be used for production of bone implants. Also, the post-processing treatments generally do not affect the biocompatibility of the Ti6Al4V ELI and are important for ensuring an improved fatigue for the implants [34].

5.2 Comparison of vector and STL based approach

Based on the results for the comparison between the vector based and STL based approach samples, a visible improvement in both compression and fatigue properties is seen for the STL approach. It is important to take into account the fact that the STL approach samples had a higher relative density at 38 %. An increase in relative density results in an increase in the strength of the porous structure as it would start resembling a fully dense sample.

The STL approach samples show a reduction in the amount of loosely stuck and partially melted powder particles as seen in Figure 4.14. The reduction is due to the use optimised process parameters for the production of the STL samples. The use of optimised parameters can subsequently minimise the need for surface modification techniques to smoothen as well as remove such particles from the strut surface. This shows the importance of process parameter optimisation, as mentioned multiple times.

Based on the hardness results shown in Table 4.10, an increase in hardness of 7% is seen for the STL samples. Though the parameters used in the processing of STL samples are not known, this can be attributed to the process parameters used for the samples which can affect the grain size of the α' phase. From Figure 4.13, acicular or fine needle like α' phases are observed in both cases. Also, the prior β grains in which the martensite nucleate and grow can be distinguished evidently in the microstructure for the STL samples. During microstructure analysis, the amount of process induced porosity observed were lesser for the STL based samples.

The results for the compression test are plotted in Figure 4.15. The declining stress behaviour observed in the case of vector based samples are due to the presence of high percentage of process induced internal porosity. STL samples confirm the compression behaviour observed in literature, where each layer failure is accompanied with a sudden drop in the stress and subsequent densification. The effect of densification is observed with an increase in the stress for increasing strain after 0.5 strain. Figure 5.7 shows the images of the samples after the compression test. An evident improvement in the quality of the samples for the STL approach is seen. Hence, it can be concluded that the vector based approach does not have optimized processing parameters resulting in the failure of the structure without any visible densification effect as seen in the σ - ϵ plots.

(a)



(b)

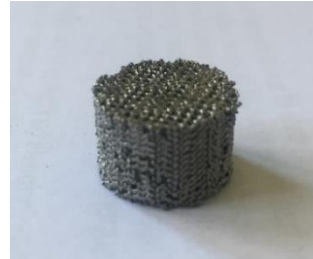
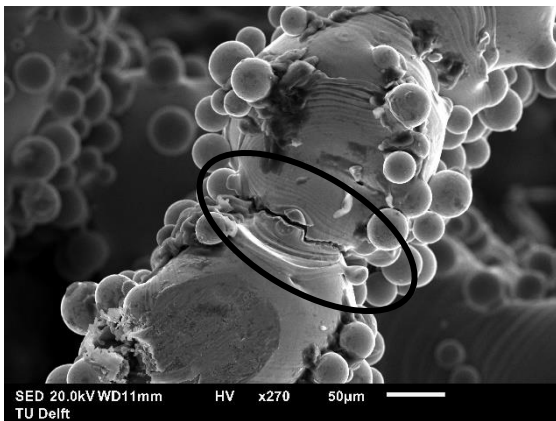


Figure 5.7 Compression specimens after testing (a) Vector based and (b) STL based.

(a)



(b)

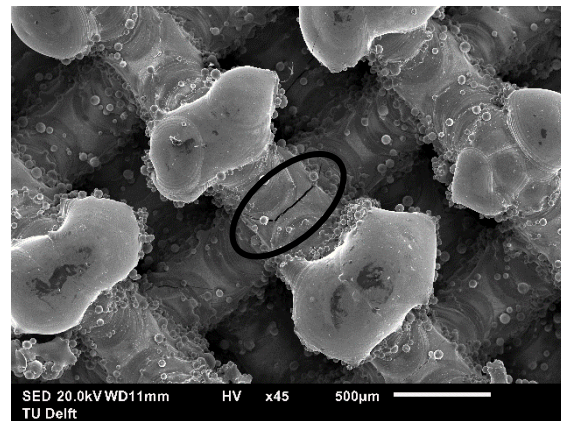


Figure 5.8 Fatigue cracks in (a) Vector based and (b) STL based samples.

The fatigue results as shown in Figure 4.16 and Table 4.12 show an improvement in fatigue life for the STL approach based samples with scatter reduction. Also, a fatigue life of one million cycle with no apparent failure of the structure was seen at 0.2 normalised stress for STL samples. The regions of failure and crack growth are shown in Figure 5.8. The failure of the samples for the vector approach samples is most likely caused at the interconnection of two spot welds or two weld beads. But in the case of STL based samples the failure was at the nodes of the unit cell joining two struts and not in the strut itself. This indicates that the sites of stress concentration and failure for vector based approach are at the intersection of the beads in addition to the nodes between the struts. This makes them more prone to failure as the number of sites prone to crack initiations are higher in the case of vector based samples. Thus, making them susceptible to fatigue failure at lower number of cycles however low the load is compared to STL samples. This could be an inherent defect with the vector based approach. Also, the decrease in scatter of data for STL samples upholds the importance of process parameter optimisation for SLM processed samples. The scatter was reduced to less than 10 % for the STL approach samples as compared to vector based samples which show a scatter of as high as 40 % for a few testing conditions. Though, the reduction in scatter can be a result of smaller sample space for STL samples. In order to ensure repeatability in the fatigue properties for both the post-processed and as-processed conditions, the process parameter optimisation during sample fabrication is of utmost importance. This can help improve the properties drastically in the as-processed samples which would then be evident in improved mechanical properties after post-processing. Also, to have a more conclusive and

detailed understanding of the difference between the two approaches, a larger sample space is needed for the STL samples.

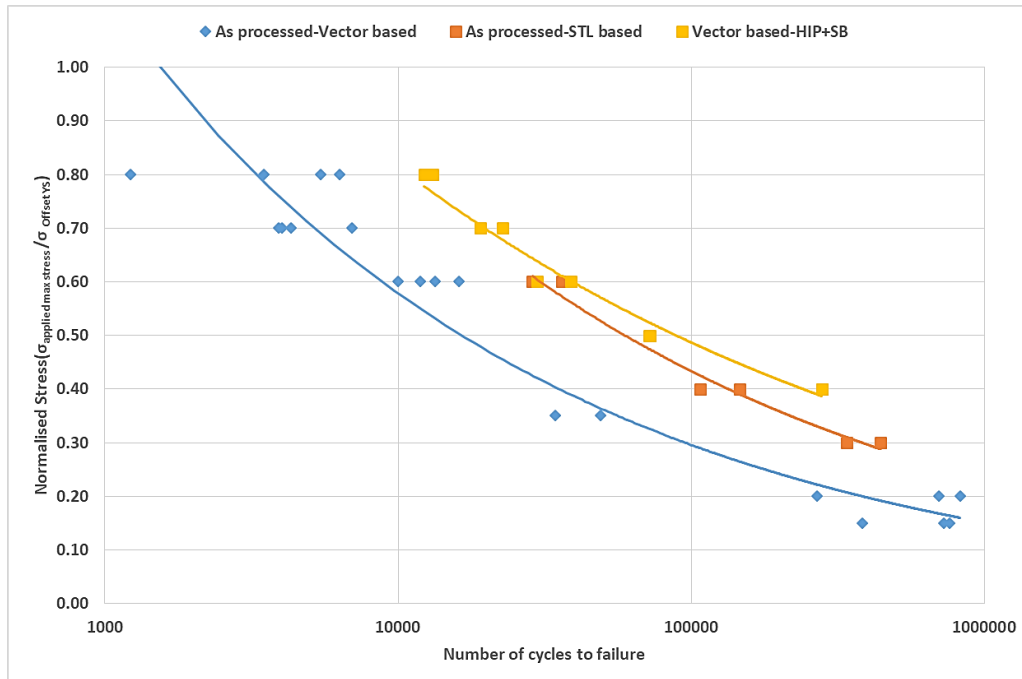


Figure 5.9 S-N curve comparison of as-processed vector based and STL based with HIP+SB samples.

Figure 5.9 shows the S-N curves for as-processed vector based and STL based compared to HIP+SB samples for normalised stress. From the S-N curve, it can be said that a combination of HIP and sandblasting resulted in a fatigue behaviour better than the as-processed STL sample even with poor quality as-processed vector approach samples. This shows that sandblasting along with HIP is the most influential among the post-processing techniques tested for porous structures in improving fatigue life.

Chapter 6 Conclusion and recommendations

6.1 Conclusions

The influence of post-processing, namely HIP and surface modification treatment, namely chemical etching and sandblasting for diamond unit cell porous biomaterials processed by SLM using the vector based approach was studied. Furthermore, a comparison between the as-processed properties of the vector based and STL based approach were investigated. The research objectives have been analysed and based on this study, the following conclusions per objective can be drawn:

1. Investigating post-processing techniques, namely, hot isostatic pressing (HIP) and surface modification for Ti6Al4V lattice structures manufactured by vector based approach:
 - The post-processing of SLM processed lattice structure is necessary to realise their usage for manufacturing of implants as they improve the ductility and fatigue life.
 - Application of HIP treatment reduces the process induced defects in the struts and improves the mechanical properties of the material.
 - Chemical etching is a promising surface modification technique to improve the fatigue life of the porous structure but requires further optimisation to homogenise the treatment.
 - Sandblasting is a surface modification approach, which has been for the first time applied in this study to porous structures.
 - Sandblasting in combination with HIP is the most influential post-processing technique to improve the fatigue life without considerable reduction in strength.
 - Sandblasting improved fatigue life by surface roughness optimization and introduction of compressive stress, similar to shot peening, retarding crack initiation and growth at the strut surface. Even with the aforementioned advantages, sandblasting requires further optimisation to realise its full potential.
 - Both the surface modification techniques impart micron level roughness which can be beneficial in osseointegration and bone on growth in implants.
2. Investigating the relationship between the microstructure and mechanical properties, namely compression and fatigue life before and after post-processing:
 - A change in microstructure after post-processing from non-equilibrium, α' to lamellar ($\alpha+\beta$) microstructure can be seen. No influence of surface modification on the HIP microstructure based on optical images and XRD results.
 - The presence of β phase up to 10% after post-processing corresponds to the ductile behaviour of the post-processed samples during compression and improved fatigue behaviour.

- HIP in addition to a change in microstructure aids closure of internal voids and defects induced during processing.
 - The post-processed samples show improved compression behaviour with ductility and better fatigue life with reduced scatter.
3. Comparison between the vector based and STL based approaches using as-processed samples:
- The importance of process parameter optimisation is reemphasised based on the comparison between STL and vector based approach samples.
 - The vector based approach has inherent stress concentration and crack initiation sites at the region linking the beads forming the strut which could be detrimental for fatigue life.
 - A combination of HIP and sandblasting is required in order to improve the fatigue behaviour of vector based as compared to the STL based samples.

6.2 Recommendation for future work

This thesis presents a preliminary analysis and a further in-depth fundamental investigation is required. The following recommendations and follow-up project directions are proposed:

- Based on the study for vector based approach, it was observed that the process parameter should be further optimised to improve the properties. This was reemphasised based on the comparison between the STL and vector based approach samples.
- Compare the properties with samples heat treated below and above the β transus temperature. This would help ensure a complete understanding of the relation between the microstructure and the mechanical properties. In addition, the influence of temperature and time on the grain morphology can be studied.
- Homogenisation of the chemical etching treatment, where preliminary attempts were made to homogenise the process with the use of various etchant compositions and times. Also, the use of ultrasonic bath to homogenise the process was explored. But due to the lack of time work could not be carried out further. The results were promising in a few cases as shown in 0.
- The approach of sandblasting as a surface optimisation technique on porous structures has not been found in literature. As the results have shown, sandblasting is a promising technique for improving the fatigue life. Therefore, it is important to understand its influence on porous structures. For example, the influence of grain morphology and texture on the compressive stresses created on the surface. Also, it is important to characterise the compressive stresses in terms of their magnitude and depth.
- Studying the influence of abrasive shape and size on the strut surface. The influence of sandblasting in this thesis is limited to irregularly shaped abrasives. Thus, it is important to see the behaviour of porous structure under, for example, smaller size abrasive particle which could help reach deeper channels of the interconnected network.
- Explore the influence of the etchant and immersion time used in this study for larger unit cell size porous structures. This could ensure a homogenisation in the surface modification treatment as suggested in the discussion. Literature [33] shows that a larger unit cell size have a homogenised chemical etching treatment.

-
- Using the same testing methods and parameters, a similar study should be carried out on different unit cell designs and sizes. This would enable us to understand the influence of design on the post-processing.
 - Quantitative analysis for roughness measurements was done using the Keyence VHX5000 microscope but because of the manufacturing of the samples based on the vector based approach could not be verified with literature. Attempts were made to find the bead roughness as the technique involved melting the powder at intersection of the strut vector and the sliced layer giving a bead like structure similar to a spot weld. Details regarding the same can be found in the Appendix B.

References

- [1] D. C. Hofmann *et al.*, "Compositionally graded metals: A new frontier of additive manufacturing," *Journal of Materials Research*, vol. 29, no. 17, pp. 1899-1910, 2014.
- [2] D. L. Bourell, "Perspectives on Additive Manufacturing," *Annual Review of Materials Research*, vol. 46, no. 1, pp. 1-18, 2016.
- [3] J. J. Beaman, J. W. Barlow, D. L. Bourell, R. H. Crawford, H. L. Marcus, and K. P. McAlea, "Solid freeform fabrication: a new direction in manufacturing," *Kluwer Academic Publishers, Norwell, MA*, vol. 2061, pp. 25-49, 1997.
- [4] B. Van Hooreweder, Y. Apers, K. Lietaert, and J. P. Kruth, "Improving the fatigue performance of porous metallic biomaterials produced by Selective Laser Melting," *Acta Biomaterialia*, vol. 47, pp. 193-202, Jan 01 2017.
- [5] B. Vrancken, L. Thijs, J.-P. Kruth, and J. Van Humbeeck, "Heat treatment of Ti6Al4V produced by Selective Laser Melting: Microstructure and mechanical properties," *Journal of Alloys and Compounds*, vol. 541, pp. 177-185, 2012.
- [6] A. Sidambe, "Biocompatibility of Advanced Manufactured Titanium Implants—A Review," *Materials*, vol. 7, no. 12, pp. 8168-8188, 2014.
- [7] L. E. Criales, Y. M. Arsoy, and T. Özel, "Sensitivity analysis of material and process parameters in finite element modeling of selective laser melting of Inconel 625," *The International Journal of Advanced Manufacturing Technology*, vol. 86, no. 9-12, pp. 2653-2666, 2016.
- [8] T. Vilaro, C. Colin, and J. D. Bartout, "As-Fabricated and Heat-Treated Microstructures of the Ti-6Al-4V Alloy Processed by Selective Laser Melting," *Metallurgical and Materials Transactions A*, vol. 42, no. 10, pp. 3190-3199, 2011.
- [9] W. Xu *et al.*, "Additive manufacturing of strong and ductile Ti-6Al-4V by selective laser melting via in situ martensite decomposition," *Acta Materialia*, vol. 85, pp. 74-84, 2015.
- [10] P. C. Collins, D. A. Brice, P. Samimi, I. Ghamarian, and H. L. Fraser, "Microstructural Control of Additively Manufactured Metallic Materials," *Annual Review of Materials Research*, vol. 46, no. 1, pp. 63-91, 2016.
- [11] I. Yadroitsev, P. Krakhmalev, and I. Yadroitsava, "Hierarchical design principles of selective laser melting for high quality metallic objects," *Additive Manufacturing*, vol. 7, pp. 45-56, 2015.
- [12] G. Kasperovich and J. Hausmann, "Improvement of fatigue resistance and ductility of TiAl6V4 processed by selective laser melting," *Journal of Materials Processing Technology*, vol. 220, pp. 202-214, 2015.
- [13] S. M. Ahmadi, R. Hedayati, R. K. Ashok Kumar Jain, Y. Li, S. LeeFlang, and A. A. Zadpoor, "Effects of laser processing parameters on the mechanical properties, topology, and microstructure of additively manufactured porous metallic biomaterials: A vector-based approach," *Materials & Design*, vol. 134, pp. 234-243, 2017.
- [14] J. P. Kruth, "Consolidation phenomena in laser and powder-bed based layered manufacturing," (in eng), *CIRP Annals - Manufacturing Technology*, vol. 56, no. 2, pp. 730-759, 2007.

- [15] R. Wauthle *et al.*, "Effects of build orientation and heat treatment on the microstructure and mechanical properties of selective laser melted Ti6Al4V lattice structures," *Additive Manufacturing*, vol. 5, pp. 77-84, 2015.
- [16] B. Song *et al.*, "Differences in microstructure and properties between selective laser melting and traditional manufacturing for fabrication of metal parts: A review," *Frontiers of Mechanical Engineering*, vol. 10, no. 2, pp. 111-125, 2015.
- [17] M. Qian, W. Xu, M. Brandt, and H. P. Tang, "Additive manufacturing and postprocessing of Ti-6Al-4V for superior mechanical properties," *MRS Bulletin*, vol. 41, no. 10, pp. 775-784, 2016.
- [18] G. Pyka, G. Kerckhofs, I. Papantoniou, M. Speirs, J. Schrooten, and M. Wevers, "Surface Roughness and Morphology Customization of Additive Manufactured Open Porous Ti6Al4V Structures," *Materials*, vol. 6, no. 10, pp. 4737-4757, 2013.
- [19] G. Pyka *et al.*, "Surface Modification of Ti6Al4V Open Porous Structures Produced by Additive Manufacturing," *Advanced Engineering Materials*, vol. 14, no. 6, pp. 363-370, 2012.
- [20] M. Geetha, A. K. Singh, R. Asokamani, and A. K. Gogia, "Ti based biomaterials, the ultimate choice for orthopaedic implants – A review," *Progress in Materials Science*, vol. 54, no. 3, pp. 397-425, 2009.
- [21] A. A. Antonyamy, "Microstructure, texture and mechanical property evolution during additive manufacturing of Ti6Al4V alloy for aerospace applications," Doctor of Philosophy, Faculty of Engineering and Physical Sciences, University of Manchester, 2012.
- [22] B. Dutta and F. H. Froes, "The Additive Manufacturing of Titanium Alloys," pp. 1-10, 2016.
- [23] S. Ahmadi *et al.*, "Additively Manufactured Open-Cell Porous Biomaterials Made from Six Different Space-Filling Unit Cells: The Mechanical and Morphological Properties," *Materials*, vol. 8, no. 4, pp. 1871-1896, 2015.
- [24] S. Amin Yavari *et al.*, "Effects of bio-functionalizing surface treatments on the mechanical behavior of open porous titanium biomaterials," *J Mech Behav Biomed Mater*, vol. 36, pp. 109-19, Aug 2014.
- [25] S. Ahmadi *et al.*, "Mechanical behavior of regular open-cell porous biomaterials made of diamond lattice unit cells," *Journal of the mechanical behavior of biomedical materials*, vol. 34, pp. 106-115, 2014.
- [26] T. Kawai *et al.*, "Osteoconduction of porous Ti metal enhanced by acid and heat treatments," *J Mater Sci Mater Med*, vol. 24, no. 7, pp. 1707-15, Jul 2013.
- [27] A. Butscher, M. Bohner, S. Hofmann, L. Gauckler, and R. Müller, "Structural and material approaches to bone tissue engineering in powder-based three-dimensional printing," *Acta biomaterialia*, vol. 7, no. 3, pp. 907-920, 2011.
- [28] M. Thöne, S. Leuders, A. Riemer, T. Tröster, and H. Richard, "Influence of heat-treatment on Selective Laser Melting products—eg Ti6Al4V," in *Solid freeform fabrication symposium SFF, Austin Texas*, 2012.
- [29] M. Brandt, S. J. Sun, M. Leary, S. Feih, J. Elambasseril, and Q. C. Liu, "High-value SLM aerospace components: from design to manufacture," in *Advanced Materials Research*, 2013, vol. 633, pp. 135-147: Trans Tech Publ.
- [30] S. Leuders *et al.*, "On the mechanical behaviour of titanium alloy TiAl6V4 manufactured by selective laser melting: Fatigue resistance and crack growth performance," *International Journal of Fatigue*, vol. 48, pp. 300-307, 2013.

- [31] V. Cain, L. Thijs, J. Van Humbeeck, B. Van Hooreweder, and R. Knutsen, "Crack propagation and fracture toughness of Ti6Al4V alloy produced by selective laser melting," *Additive Manufacturing*, vol. 5, pp. 68-76, 2015.
- [32] A. Jemat, M. J. Ghazali, M. Razali, and Y. Otsuka, "Surface modifications and their effects on titanium dental implants," *BioMed research international*, vol. 2015, 2015.
- [33] C. de Formanoir, M. Suard, R. Dendievel, G. Martin, and S. Godet, "Improving the mechanical efficiency of electron beam melted titanium lattice structures by chemical etching," *Additive Manufacturing*, vol. 11, pp. 71-76, 2016.
- [34] M. Benedetti *et al.*, "The effect of post-sintering treatments on the fatigue and biological behavior of Ti-6Al-4V ELI parts made by selective laser melting," *Journal of the Mechanical Behavior of Biomedical Materials*, vol. 71, pp. 295-306, 2017.
- [35] C. Y. Guo, J. P. Matinlinna, J. K.-H. Tsoi, and A. T. H. Tang, "Residual Contaminations of Silicon-Based Glass, Alumina and Aluminum Grits on a Titanium Surface After Sandblasting," *Silicon*, pp. 1-8, 2015.
- [36] *Mechanical testing of metals—ductility testing—compression test for porous and cellular metals, 2011, 2011.*
- [37] S. M. Ahmadi, R. K. Ashok Kumar Jain, A. A. Zadpoor, C. Ayas, and V. Popovich, "Effects of heat treatment on microstructure and mechanical properties of additive manufactured porous Ti6Al4V," presented at the International Conference on Smart Material Research, Melbourne, Australia, 2017.
- [38] B. D. Cullity and J. W. Weymouth, *Elements of X-ray Diffraction* (American Journal of Physics, no. 6). 1957.
- [39] S. A. Yavari *et al.*, "Fatigue behavior of porous biomaterials manufactured using selective laser melting," *Materials Science and Engineering: C*, vol. 33, no. 8, pp. 4849-4858, 2013.
- [40] S. A. Yavari *et al.*, "Relationship between unit cell type and porosity and the fatigue behavior of selective laser melted meta-biomaterials," *Journal of the mechanical behavior of biomedical materials*, vol. 43, pp. 91-100, 2015.
- [41] I. Yadroitsev, P. Krakhmalev, and I. Yadroitsava, "Selective laser melting of Ti6Al4V alloy for biomedical applications: Temperature monitoring and microstructural evolution," *Journal of Alloys and Compounds*, vol. 583, pp. 404-409, 2014.
- [42] P. A. Kobryn and S. Semiatin, "Microstructure and texture evolution during solidification processing of Ti-6Al-4V," *Journal of Materials Processing Technology*, vol. 135, no. 2, pp. 330-339, 2003.
- [43] A. Basak and S. Das, "Epitaxy and Microstructure Evolution in Metal Additive Manufacturing," *Annual Review of Materials Research*, vol. 46, no. 1, pp. 125-149, 2016.
- [44] Y. Harada, K. Fukaura, and S. Haga, "Influence of microshot peening on surface layer characteristics of structural steel," *Journal of Materials Processing Technology*, vol. 191, no. 1, pp. 297-301, 2007.
- [45] M. Long and H. Rack, "Titanium alloys in total joint replacement—a materials science perspective," *Biomaterials*, vol. 19, no. 18, pp. 1621-1639, 1998.
- [46] B. AlMangour and J.-M. Yang, "Improving the surface quality and mechanical properties by shot-peening of 17-4 stainless steel fabricated by additive manufacturing," *Materials & Design*, vol. 110, pp. 914-924, 2016.

- [47] S. Beretta and S. Romano, "A comparison of fatigue strength sensitivity to defects for materials manufactured by AM or traditional processes," *International Journal of Fatigue*, vol. 94, pp. 178-191, 2017.
- [48] J. Schijve, *Fatigue of structures and materials*. Springer, 2001.
- [49] J. De Krijger, "The effect of stress ratio on the fatigue behavior of additively manufactured porous biomaterials," Master of Science, Delft University of Technology, 2016.

Appendix A Fatigue data overview

Table A-1 shows the overview of the fatigue data. The number of cycles to failure for all the samples tested with respect to the normalised stress are shown.

Table A-1 Overview of the fatigue data for all the samples.

Sample Type	Number of cycles to failure (With respect to normalised stress)								
	0.15	0.2	0.3	0.35	0.4	0.5	0.6	0.7	0.8
As-processed	383401	268051	-	34362	-	-	10021	4026	5436
	761875	698274	-	49207	-	-	16137	3918	3483
	729635	827446	-	-	-	-	13386	4317	1220
	-	-	-	-	-	-	11878	6964	6309
HIP	-	1000000+	403794	-	100073	-	22171	12134	7771
	-	-	388954	-	118394	-	21926	12622	7772
HIP+CE	-	1000000+	582000	-	83843	-	27662	-	3543
	-	-	882204	-	111870	-	28727	-	5416
HIP+SB	-	1000000+	1000000+	-	279182	72107	38761	19119	12288
	-	-	-	-	278907	71700	29863	22678	13125
As-processed (STL)	-	1000000+	442954	-	146285	-	36239	-	-
	-	-	339530	-	107196	-	28752	-	-

The samples shown with 1000000+ cycles did not fail and based on the constraint applied to the test, the machine stopped and the fatigue test were not carried out any further.

Appendix B Surface roughness quantification

As mentioned in the recommendation, surface roughness trials were carried out using the Keyence VHX5000. The results of the surface roughness could not be verified due to the usage of the vector based approach. Also, the measurements included two factors: bead roughness and strut roughness.

B.1 Bead roughness

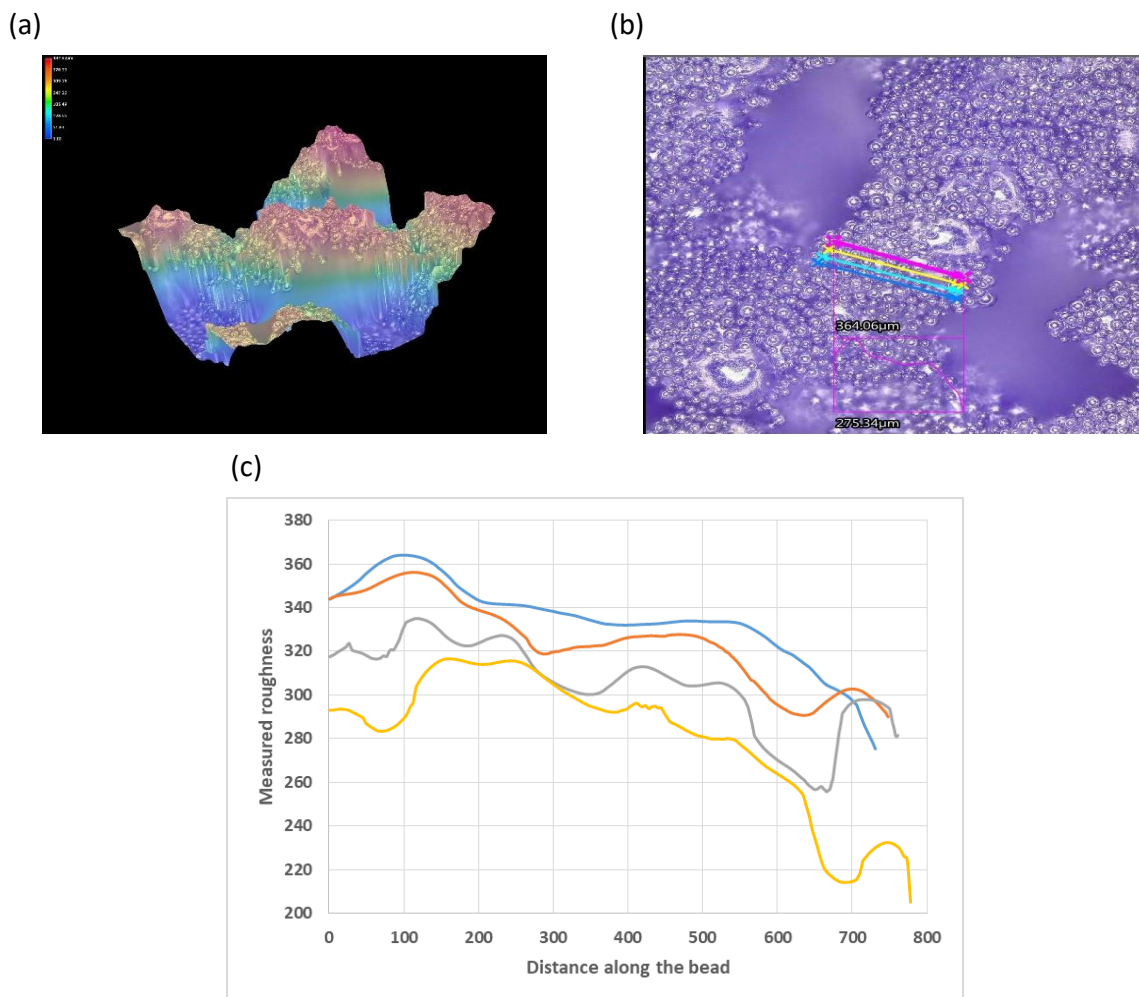


Figure B-1 Bead roughness measurement (a) Stitched image (b) Line along which roughness measurements were carried out and (c) Roughness profile.

The roughness of each bead was calculated as shown in the Figure B-1. The VHX software took images along the z axis and stitched the image together based on which the roughness was measured. Figure B-1 shows the stitched image and the roughness profile of a sample bead measurement.

Table B-1 shows the bead roughness along the lines shown in Figure B-1 (b) and roughness profile shown in (c). The calculation were done using the least square method with respect to the mean.

Table B-1 Bead roughness.

	Pink	Yellow	Light blue	Blue	Mean Roughness (μm)
Average Roughness (μm)	18.22	19.06	22.20	28.32	21.45 \pm 4.65

Based on the Table B-1, an average roughness of 21.45 μm for bead was determined. The values of the roughness could not be verified with literature. But they are well within the size of the powder particles used for processing during SLM. This gives an indication that the values are realistic but require verification.

B.2 Profile Roughness

The roughness along the strut was calculated to determine the profile roughness of the struts. Figure B-2 shows the stitched image from the top surface and the roughness profile of a sample measurement.

Table B-2 shows the bead roughness along the lines shown in Figure B-1 (b) and roughness profile in (c). The calculation were done using the least square method with respect to the mean. As for the profile roughness a large deviation on comparing individual lines is observed. This can be a result of the measurements being carried out on the same bead or due to the inclination of the strut.

Table B-2 Profile roughness.

	Pink	Light blue	Blue	Orange	Mean Roughness (μm)
Average Roughness (μm)	27.73	22.99	8.59	11.88	17.80 \pm 9.05

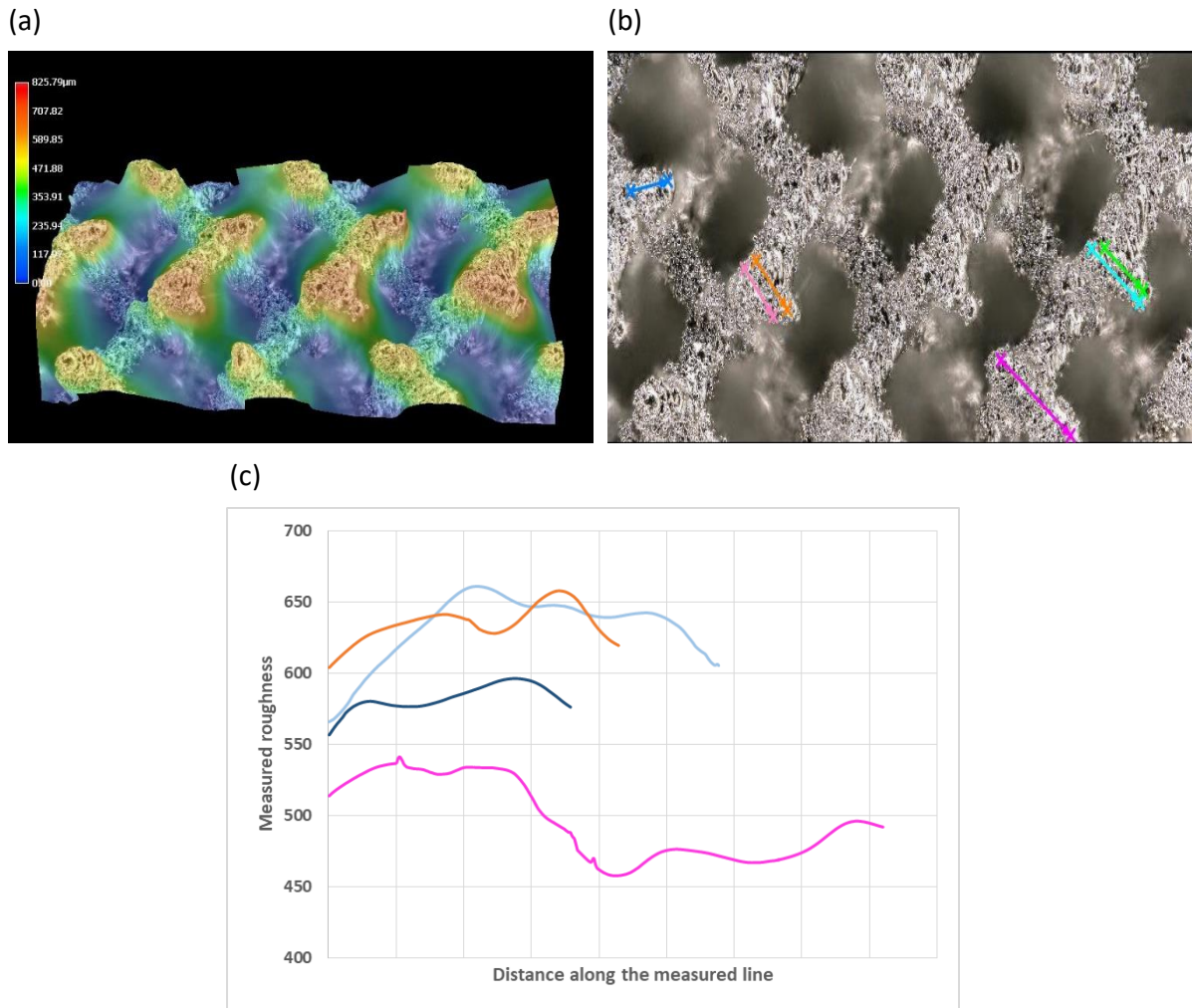


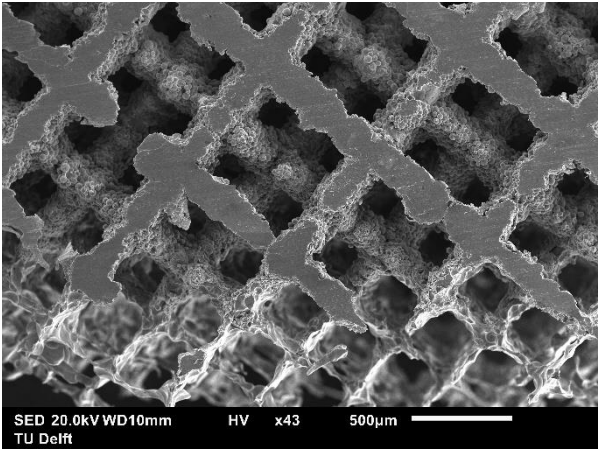
Figure B-2 Profile roughness measurement (a) Stitched image (b) Line along which roughness measurements were carried out and (c) Roughness profile.

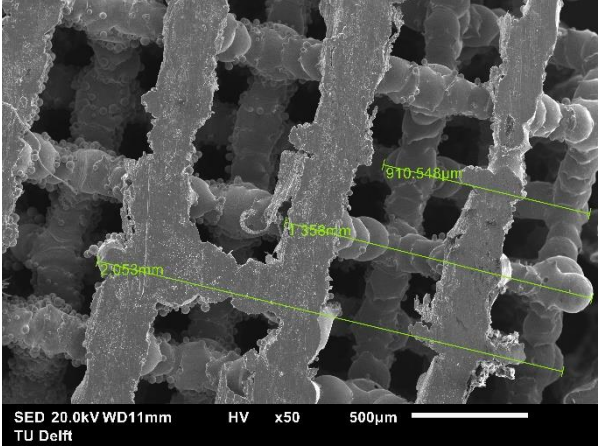
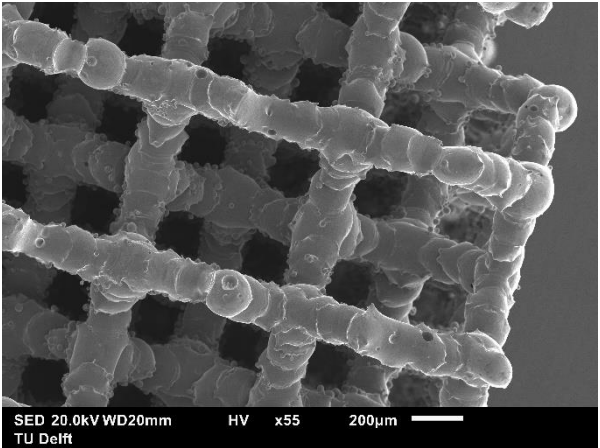
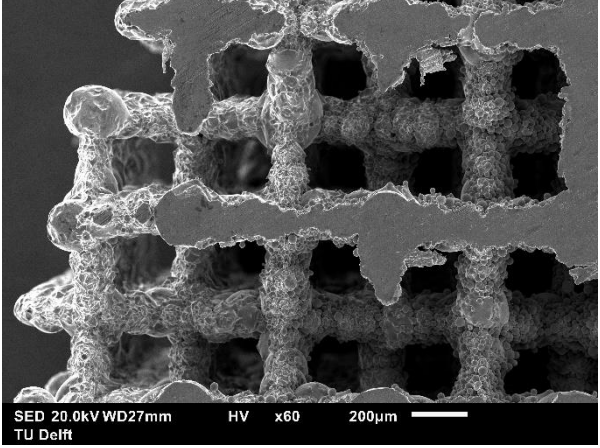
Appendix C Chemical etching trials

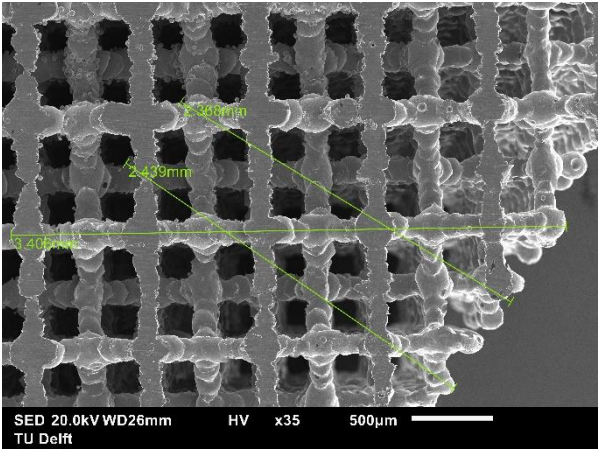
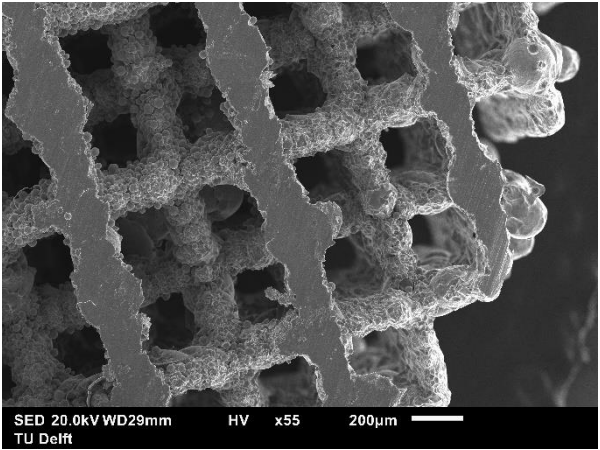
As mentioned in the thesis, a number of chemical etching solutions and immersion times were attempted to homogenise the process. In addition, ultrasonic bath was used during immersion to reduce the amount of air bubbles from affecting the removal of material and ensure flow of the etchant into the sample core. The etching results were either bad or promising but did not show repeatability. Images for a few samples were taken at the core but the etching process did not seem effective. The core images were similar to the core of HIP+CE samples shown in Section 4.1.3.

Table C-2 consists of the etchant with the immersion time and SEM images from either the top or middle. Note that all the samples during immersion were placed in an ultrasonic bath. From the table it can be seen that the results for etching using 90.625 ml H₂O, 7.8125 ml HNO₃ and 1.5625 ml HF for 360 seconds, 93.3125 ml H₂O, 3.90625 ml HNO₃ and 0.78125 ml HF for 900 seconds and 98.835 ml H₂O, 1.5 ml HNO₃, 3 ml H₂SO₄ and 1.665 ml HF showed promising results. The etching was seen to reach deeper channels of the interconnected network. But the process was not repeatable.

Table C-2 Chemical etching trials with etchant, time and SEM images.

Etching solution	Etching time (in seconds)	SEM Images
81.25 ml H ₂ O, 15.625 ml HNO ₃ and 3.125 ml HF.	360	 <p style="text-align: center;">(Image from middle)</p>

<p>90.625 ml H₂O, 7.8125 ml HNO₃ and 1.5625 ml HF.</p>	<p>360</p>	 <p>(Image from middle)</p>
<p>93.3125 ml H₂O, 3.90625 ml HNO₃ and 0.78125 ml HF.</p>	<p>900</p>	 <p>(Image from top)</p>
	<p>+ 1800</p>	 <p>(Image from middle)</p>

<p>98.835 ml H₂O, 1.5 ml HNO₃, 3 ml H₂SO₄ and 1.665 ml HF</p>	<p>900</p>	 <p>(Image from middle)</p>
	<p>+ 900</p>	 <p>(Image from middle)</p>